Technische Universiteit Delft

Electrolytic Plasma Cleaning of Advanced High Strength Steels

Muhammad Arsel Hasan

TU Delft

TATA STEEL

Electrolytic Plasma Cleaning of Advanced High Strength Steels

By

Muhammad Arsel Hasan
Student Number, 4688538

submitted in partial fulfilment of the requirements for the degree of Master of Science Technical University Delft, Delft, Netherlands, Department of Cognitive Robotics, Master track Vehicle Engineering, to be publicly defended on Monday 29th January, 2020 at 10:00.

Panel

Dr. ir. Wim G. Sloof,
Associate Professor - Principal Investigator,
Department of Materials Science and Engineering,
Mechanical, Maritime and Materials Engineering (3mE),
TU Delft, The Netherlands.

Dr. ir. Jilt Sietsma,
Principal Researcher,
Department of Materials Science and Engineering,
Mechanical, Maritime and Materials Engineering (3mE),
TU Delft, The Netherlands.

Dr. ir. Marcel J.M. Hermans,
Associate Professor - Principal Investigator,
Department of Materials Science and Engineering,
Mechanical, Maritime and Materials Engineering (3mE),
TU Delft, The Netherlands.

TU Delft

TATA STEEL

Acknowledgement

This master thesis would not have materialized without the help and support of many individuals whom I wish to acknowledge. First and foremost, I would like to express my sincere gratitude to Dr. ir. Wim G. Sloof, who offered me this opportunity to perform my master's thesis project at Tata Steel, Ijmuiden, The Netherlands. I would like to thank him for providing guidance and support wherever possible. I would like to thank Dr. ir. Jilt Sietsma for always being there at an email's length away to help me with the difficulties I faced while trying to become a better materials engineer. My heartfelt thanks to Dr. ir. Marcel J.M. Hermans for his inputs during the final stages of the report. Finally, I thank the entire 3mE faculty for catapulting me into the field of research, it has truly been an enriching experience.

I would like to thank Dr. Ruud Westwerwaal from Tata Steel for introducing me to the research idea explored in this thesis, as well as for his guidance during the entire phase of this research. I am also indebted to a lot of people from Tata Steel for all of the technical advice and help that I received from them.

My experience in Delft, for the most part, has been shaped by my friends and fellow students. I would like to thank each of them for making Delft all the more bearable. I would also like to thank Ms. Lourdes Gallastegui Pujana, who helped in building my confidence to face the challenges during my time at TU Delft.

Finally, but most importantly, I would like to thank my family, especially my parents and my sister for their unconditional love and support through all the tough times. They have stood by me through thick and thin and have always inspired me to better myself, personally and professionally. They will always be my greatest strength, and I dedicate this work to them.

Delft University of Technology Muhammad Arsel Hasan

29th of January, 2020.

Abstract

The automotive industry is continuously improving in performance and fuel efficiency year after year. With the increasing feature comforts, safety measures and the rise in the number of driver assistive technologies in a modern car, the weight of an average car would have increased drastically over the years had it not been a constant strive within the automotive industry to reduce the same by means of using better materials and better production techniques.

The most commonly used material in the automotive industry is steel. Steel used in making Body-In-White (BIW) for cars are broadly classified as Advanced High Strength Steels (AHSS). These AHSS are produced by a well-defined alloying and specific annealing procedure. They undergo cold rolling to give them maximum thickness reduction and better work hardening properties. After cold rolling, the steel is annealed to remove residual stresses and burn off the excess oil from the operation. The annealed steel can either be coated with Zinc using Hot Dip Galvanisation (HDG) or can be taken for further pre-cleaning treatment to subsequently coat them using novel techniques such as Physical Vapour Deposition (PVD) to prevent corrosion. HDG is the most common method of applying a protective coating to steel. However, the annealing step prior to hot dipping can cause external oxidation of the constituent alloying elements from the steel. This selective oxidation of alloying elements on the steel surface affects the adhesion of the Zinc to the steel. The Zinc bath consists of some Aluminium in it to help reduce these surface oxides and to form an inhibition layer that helps improving the coating adhesion. Electrolytic Plasma Cleaning can be introduced after the annealing to free the surface from oxides before HDG or newer coating techniques, such as, PVD, where a clean surface is expected for proper deposition and adhesion of Zinc vapour on the steel sheet substrate.

The main goals of this research work were to define the optimal parametric windows for the Electrolytic Plasma Cleaning technique to form a plasma capable of cleaning a steel surface by removing external oxides formed during the annealing process. Electrolytic Plasma Cleaning uses the traditional electrochemical cell that consists of an anode, a cathode, an external potential and an electrolyte but at higher input potentials. Literature survey showed that the process promises a steel surface suitable for coating to meet the standards of the automotive industry.

An experimental setup had to be developed with the aim of finding the ideal working parameters, establishing the groundwork for future large-scale experimentation. Before trying to define the working band of the plasma parameters, the anode material and geometry needed to be confirmed so that further experiments could be carried out using the same anode and dimensions. When the appropriate material and geometry for the anode was used i.e., a solid Graphite anode with no perforations, the process successfully reduced the amount of oxides present on the surface, increase wettability and reduce the surface roughness. Additionally, for a good steel surface a near boiling electrolyte (60 to 80 °C) is required, low flow rates of 60 to 80 L/hr of electrolyte, short inter-electrode distances of 1 to 2 mm and quick treatment times of ≅ 20 seconds to generate a stable plasma and clean the surface. Concentration of electrolyte did not play an important role in the plasma formation.

Contents

ABBREVIATIONS USED 2

LIST OF FIGURES 4

LIST OF TABLES 7

1 INTRODUCTION 9

Why lightweight design? 9

Why Steel? 10

What are Advanced High Strength Steels? 11
What is DP800? 12

Annealing 12

Selective Oxidation 15

Coating Techniques 16
Hot Dip Galvanisation 17
Physical Vapour Deposition 18

Scope of thesis 19
Problem Description 19
Research Questions and Objectives 19

Outline 19

2 ELECTROLYTIC PLASMA CLEANING 21

What is Electrolytic Plasma Cleaning? 21
Types of Electrolytic Plasma Processes 23

Process Description 24

Kinetics of Plasma Discharge 25
Gas formation through electrochemical reactions 25
Gas formation through Joule heating 26

Parameters 27
Concentration of Salt 27
Temperature of Electrolyte 27
Anode 28
Material 28
Geometry 29
Inter-electrode distance 30

Flow rate/Speed 31
Frequency & Treatment time 32

3 EXPERIMENTATION 34

Experimental Setup 34
Setup Limitations 35

Procedure 36

Methodology 36

Analysis Techniques 36
Scanning Electron Microscopy 37
Secondary Electrons 37
Backscattered electrons 37
Glow Discharge Optical Emission Spectroscopy 38
Sessile Drop Experiment 38
Profilometry 39
Stylus Profilometry 39
Confocal microscopy 40

4 RESULTS 43

Annealing 43

Hot Dip Galvanisation 45

Surface Morphology 47
Steel Anode 47
Titanium Anode 48
Stainless-Steel Anode 48
Copper Anode 49
Graphite Anode 50

Surface Wettability 50

Surface Topography 51

Chemical Analysis 53

Plasma Analysis 56
Concentration of Electrolyte 56
Inter-electrode Distance 57
Flow Rate 58

5 DISCUSSIONS 60

6 CONCLUSIONS 66

7 RECOMMENDATIONS 70

8 INDUSTRIAL FEASIBILITY **72**

Energy Requirements **72**

Bottlenecks **73**

9 APPENDIX **75**

Appendix 1: Bare Spot Analysis **75**

Appendix 2: Steel droplet on treated sample **77**

Appendix 3: Titanium droplet on treated sample **78**

Appendix 4: Chromium Carbides on treated sample **79**

Appendix 5: Copper Oxide and Sodium particles on treated sample **80**

Appendix 6: DP800 Sample treated with a Graphite anode **82**

Appendix 7: Confocal Microscopy **83**

Appendix 8: Copper Deposits in treated Samples **84**

Appendix 9: Calculations **84**
Appendix 9.1: Molarity of Na_2CO_3 needed 84
Appendix 9.2: Industrial feasibility 85

10 REFERENCES **87**

Abbreviations used

Body-In-White (BIW)

Advanced High Strength Steels (AHSS)

Dual Phase (DP) steel

Transformation-Induced Plasticity (TRIP) steel

Complex Phase (CP) steel

Martensitic (MS) steel

Ferritic-Bainitic (FB) steel

Twinning-Induced Plasticity (TWIP) steel

Continuous Annealing Line (CAL)

Direct Fired Furnace (DFF)

Radiant Tube Furnace (RTF)

Hot Dip Galvanisation (HDG)

Physical Vapour Deposition (PVD)

Electrolytic Plasma Cleaning (EPC)

Electrolytic Plasma Processing (EPP)

Contact Glow Discharge Electrolysis (CGDE)

Sodium Bicarbonate (Na_2CO_3)

Scanning Electron Microscopy (SEM)

Energy Dispersive X-ray Spectroscopy (EDS)

Glow Discharge Optical Emission Spectroscopy (GDOES)

Heat Affected Zone (HAZ)

Average Surface Roughness (R_a)

List of Figures

Figure	Description
1	Historical fleet CO_2 emissions performance and current standards (gCO_2/km normalized to the New European Driving Cycle) for passenger cars.
2	Estimated Real-World Fuel Economy, Horsepower, and Weight Since Model Year 1975.
3	Schematic representation of the annealing section of an industrial continuous galvanizing.
4	Typical temperature profile of a steel strip in an industrial continuous galvanizing line (i) DFF section, and, (ii) RTF section.
5	Schematic representation of the oxide concentration in the steel surface region in a normal operation after (i) oxidation in the DFF and after (ii) reduction in the RTF.
6	Defects encountered while coating steel surface with Zinc using Hot Dip Galvanisation: (i) larger bare spots (more than 0.5 cm^2), (ii) smaller bare spots (less than 0.5cm^2), and, (iii) delamination after bending.
7	On the left a schematic representation is shown of the layers formed in the galvanized coating. On the right a backscattered electron image of the HDG-coating is displayed. The coating on steel strip displayed is the coating when Aluminium is added to the Zn-bath.
8	EPC treated sample (i) Spheroidal nodules, and, (ii) Craters.
9	A standard electrochemical cell.
10	Types of Vapour-air discharge.
11	Current-voltage dependence in cathodic electrolytic plasma discharge.
12	Used (melted and oxidised) titanium 3D printed anode.
13	(i) Unused graphite anode, and, (ii) Used graphite anode.
14	Samples of DP800 treated with a (i) partially submerged, and, (ii) fully submerged Stainless-Steel anode.
15	Plasma when the gap is: (i) 1mm, and, (ii) 5mm.
16	DP800 Steel surface after (i. a) 1 mm, and, (i. b) 5 mm inter-electrode distance, (ii. a) $\dot{f}$= 60 L/hr (ii. b) $\dot{f}$= 160 L/hr, (iii. a) 50 seconds, and, (iii. b) 20 seconds.
17	Schematic representation of the EPC setup: 1) Plexiglass container containing the Na2CO3 electrolyte (295 × 487 × 536 mm^3), 2) Pump inlet, 3) Pump, 4) Pump power supply, 5) Flow meter, 6) Hollow PVC tube, 7) Electrical contact to the anode housed inside the PVC tube, 8) Anode housed inside the PVC tube, 9) Workpiece, 10) Stainless Steel workpiece holder, 11) Plasma power supply, and, 12) Height controller for the PVC tube to change the anode-cathode gap.
18	Setup with de-coupled flow. Schematic of the interaction volume of Scanning Electron Microscopy.
19	Half-treated sample due to the height difference introduced by the curvature of the steel sample.
20	Schematic of the interaction volume of Scanning Electron Microscopy.
21	Sessile drop with fitted contour (shown in green).
22	Contact angle on different materials.
23	Changing contact angle with respect to time.
24	Schematic of a stylus profilometer.
25	Working principle of confocal microscopic technique.

26	GDOES depth profilometry of (i) Manganese, (ii) Silicon, (iii) Aluminium, (iv) Boron, (v) Iron, and, (vi) Oxygen in samples annealed at different dew point temperatures.
27	Samples previously annealed at (i) -30 °C, (ii) 0 °C, and, (iii)10 °C coated using HDG process.
28	(i) Bare Spot, (ii) $FeZn_{13}$ crystals, and, (iii) No Fe_2Al_5 diffusion layer present inside the bare spot, abundance of $FeZn_{13}$ crystals on the boundaries and proper Zinc adhesion outside of the bare spot.
29	Droplet from a steel anode on the DP800 substrate.
30	Ti droplet on a DP800 steel substrate.
31	Sample after treatment with Stainless-Steel anode.
32	(i) Possible Copper Oxide particles, and, (ii) Thorn-like structures with Na on a DP800 sample treated with a Copper anode.
33	A DP800 sample treated with a Graphite Anode.
34	Contact angle measurements for EPC treated and untreated samples using anodes made out of different materials.
35	Surface Roughness as a function of (i) Treatment Time (in seconds), and, (ii) Inter-electrode Distance.
36	Cross-Sectional SEM of (i) untreated DP800 sample, and, (ii) treated DP800 sample.
37	Sideview of nodules and craters on an EPC treated DP800 sample.
38	GDOES depth profilometry to detect Copper in samples treated with a (i) Copper anode, and, (ii) Graphite anode.
39	GDOES depth profilometry to detect Oxygen in samples treated with a (i) Copper anode, and, (ii) Graphite anode.
40	GDOES depth profilometry to detect Sodium in samples treated with a (i) Copper anode, and, (ii) Graphite anode.
41	Greenish patina on the sample treated with a Copper anode.
42	Current v/s Voltage as a function of concentration.
43	Electric Field v/s Voltage as a function of inter-electrode distance.
44	Current v/s Voltage as a function of inter-electrode gap.
45	Current v/s Voltage as a function of flow rate.
46	Current and Resistance v/s Voltage as a function of changing anode material.
47	Graphite anode with cylindrical duct through it for electrolyte transport (i) used, and, (ii) unused.
48	Sample treated with (i) a solid graphite anode comprising of a cylindrical duct through it, and, (ii) a graphite anode with 37 holes.
49	Variation in the arc length and cone with respect to arc voltage in Arc Welding process.
50	Current and resistance v/s voltage when flow is through the anode and when it is de-coupled.
51	(i) The hysteresis in current and resistance with respect to voltage, and, (ii) The change in voltage, resistance and power with respect to time.
52	Block Diagram showing the dependencies between different parameters. The boxes in red denote the variable parameters.
53	Block Diagram showing the operational window for the parameters investigated. The values are inside the green diamond boxes.
54	SEM image of (1) Inside Bare Spot, (2) Boundary between bare spot and Zn coating, and, (3) Zn coating.
55	SEM image of $FeZn_{13}$ crystals inside the bare spot.

56	SEM image of steel deposit on DP800 substrate.
57	SEM image of Titanium Deposit on DP800 steel surface.
58	SEM image of plausible Chromium Carbide Deposits on the DP800 surface.
59	SEM image of Copper particles after EPC treatment of DP800 with a Copper anode.
60	SEM image of Thorn-like structures made out of Na, Cu and O.
61	SEM image of steel surface after treatment with Graphite anode.
62	GDOES depth profilometry of Copper in samples annealed at different dew point temperatures.

List of Tables

Table	Description
1	Alternative materials, potential weight savings versus cost.
2	Alloying elements and their respective weight percentages in DP800.
3	Numerical values of important intrinsic parameters.
4	Parameters taken into consideration and their classification.
5	Types of anode used; the material and the geometry used.
6	Extremities of the parameters used.
7	Important properties of Graphite used.
8	Surface Roughness of treated sample as a function of anode material and geometry.
9	Cross-section area and time taken to clean a 394.521 m^2 of cold rolled strip steel.
10	Estimated power density and energy consumption for the two possible setups based on flow.
11	Heat map obtained from confocal microscopy on R_a as a function of inter-electrode distance and treatment time.

1 Introduction

Why lightweight design?

Carmakers are under constant pressure by the authorities and consumers alike to increase fuel efficiency, performance and safety standards and reduce emissions. Regulations across the EU and 9 other governments of the world demand for reduction in fuel consumption and Green House Gas emissions, more specifically, CO_2 emission values have steered automotive manufacturers to develop vehicles which are lightweight; see Figure 1.

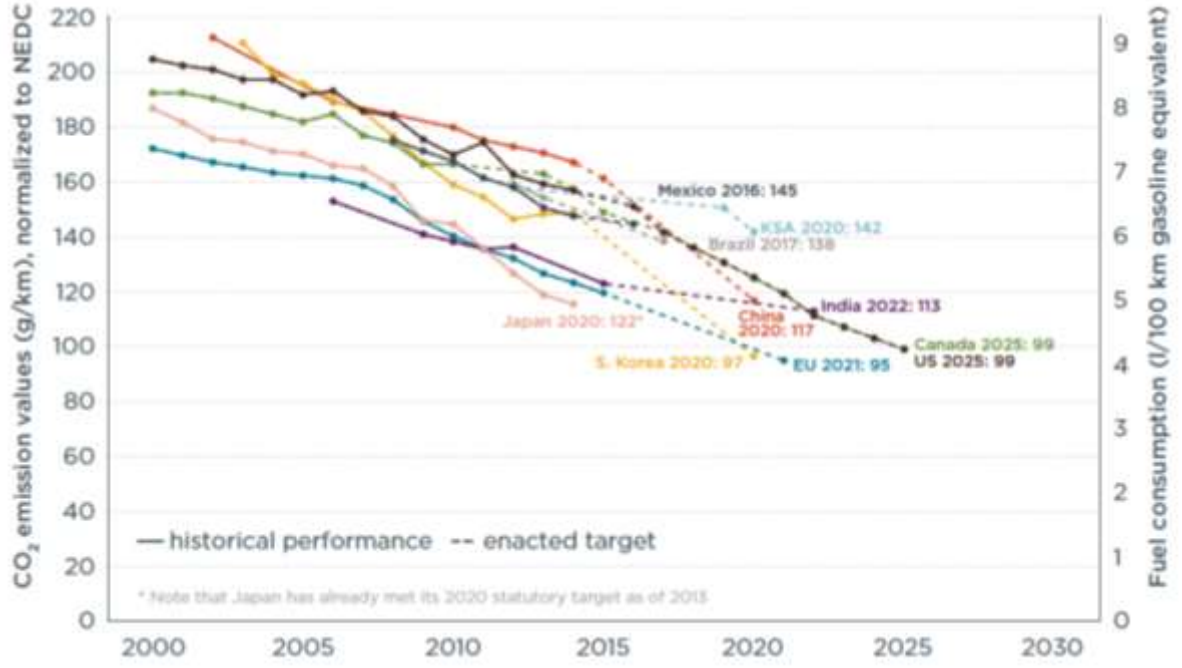

Figure 1 Historical fleet CO_2 emissions performance and current standards (gCO_2/km normalized to the New European Driving Cycle) for passenger cars [49].

Feature comforts such as heated seats, heated steering wheels, better interiors, seat massager etc., safety features starting from power steering to Anti-lock Braking System to the newest in the trend i.e., hardware for autonomous systems such as camera, sensors etc., increase the weight of car.

Vehicle weight and horsepower are two fundamental vehicle attributes that influence a vehicle's CO_2 emissions and fuel efficiency. Vehicles with higher weight, or more power, will generally have higher CO_2 emissions and lower fuel economy. Over time, innovation has been applied to vehicle design with differing emphasis between vehicle weight, power, CO_2 emissions and fuel economy.

Figure 2 shows the change in the average fuel economy, horsepower and weight relative to the year 1975. One of the reasons why the modern car manages to weigh almost the same as a car from 1975 even after so many advancements is because of the improvement in the selection of material to fabricate the different components of the car. In the two decades before the start of this century, technological innovation was generally used to increase vehicle

power, and weight increased due to changing vehicle design, increased vehicle size, and increased content. During this period, average new vehicle fuel economy steadily decreased and CO_2 emissions correspondingly increased. However, since the beginning of this century technology has been used to increase fuel economy (up 29%) and power (up 11%), while maintaining vehicle weight and reducing CO_2 emissions (down 23%). This is partly because of the persistent effort by automotive manufacturers to constantly improve the materials used in their vehicles [1].

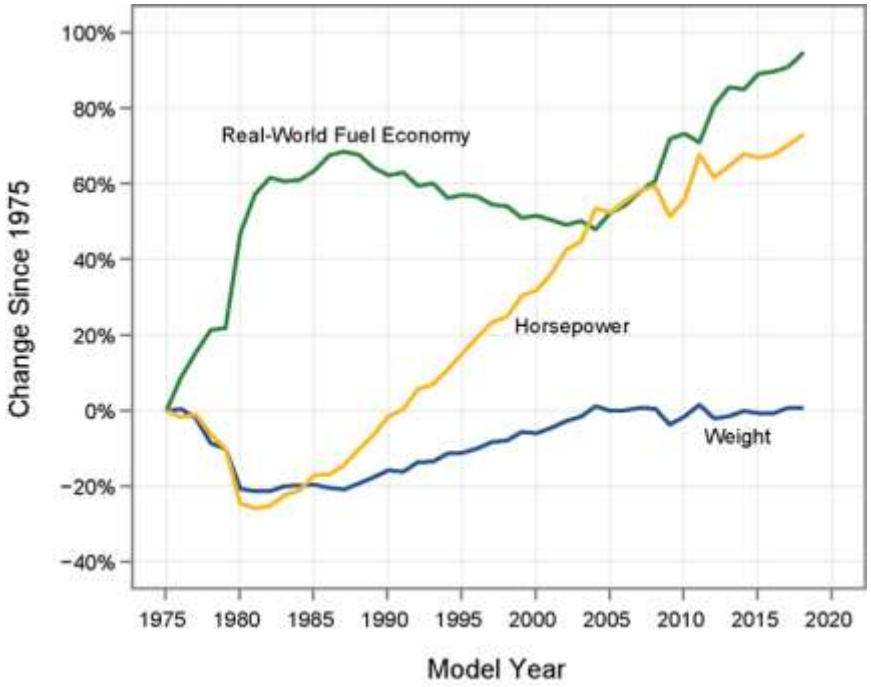

Figure 2 Estimated Real-World Fuel Economy, Horsepower, and Weight Since Model Year 1975 [1].

Why Steel?

Mass reduction through advances in the use of Iron and steel is significant (ferrous materials), because they are the dominant material in most of the passenger vehicles (64% of a typical vehicle). Iron and steel form the critical elements of structure for the vast majority of vehicles, and are low-cost materials with an extensive experience base and familiarity to the industry.

The main structure known as the Body-In-White (BIW) is usually made of steel pressings welded together to form a strong and stiff frame. This method of construction accounts for 99.9 per cent of all the cars produced in the world. The remaining 0.1 per cent is mostly constructed with Aluminium BIW, while a very small number (< 0.01 per cent) are constructed from carbon-fibre composite. The prime reason for using steel in the body structure of an automotive is its inherent capability to absorb impact energy in a crash situation. This, in combination with the good formability and joining capability, makes these materials often a first choice for the designer of the BIW structure [2]. The weight reduction versus the price increase by replacing steel by Aluminium for some of the parts is reported in Table 1.

	Steel	Aluminium	% weight reduction		% cost increase
	kg	kg	Part	vehicle	part
BIW	285	218	23.5	3.90	250
Bonnet (Assembly)	14.8	8.3	44	0.48	300
Door (Assembly)	15.7	9.5	39	0.40	275

Table 1 Alternative materials, potential weight savings versus cost [2].

The cost penalty for a marginal reduction in the overall weight of the car has limited the use of Aluminium and other metals in making the various structures of a vehicle.

Being ferrous, steel can be easily sorted from the scrapyard. Moreover, from a sustainability point of view, steel is better because modern steel production is dominated by two process routes that rely on steel scrap in different ways. Steel production via blast furnaces is based on iron ore and uses scrap as an additional element when the iron from the blast furnace is refined to steel in a basic oxygen converter. Steel production in electric arc furnaces is almost completely based on scrap. This is not only highly resource-efficient, it also reduces the overall environmental footprint of steel making considerably. A holistic perspective integrating primary steel production in blast furnaces as well as steel recycling in the electric arc furnace route shows CO_2 emissions from steel production decreasing with every recycling cycle.

In contrast, Aluminium has separate ecosystems of recyclers — Aluminium can recyclers are adept at making new Aluminium cans, and auto part recyclers at making new parts. The primary/secondary ratios, and to some extent the processes (e.g. cans have to be "demagged" or have magnesium removed) are different for these different applications. Thus, Aluminium is costlier to recycle, requiring the different grades to be separated before melting to preserve the grades.

What are Advanced High Strength Steels?

The term AHSS is primarily used to denote multi-phase steels or the high yield strength micro-alloyed steels. Conventional high strength steels are single phase ferritic steels. Automotive steels are classified in three designations: metallurgical designation includes low-strength steels, conventional high strength steel, and the newer types of AHSS. The second classification method, important to part designers, is the strength of the steel. The third classification method presents various mechanical properties or forming parameters of different steels, such as total elongation, work hardening exponent n, or hole expansion ratio.

Some types of AHSS have a higher strain hardening capacity resulting in a strength-ductility balance superior to conventional steels. Other types have ultra-high yield and tensile strengths and show a bake hardening behaviour.

The metallurgy and processing of AHSS grades are somewhat novel compared to conventional steels. Their remarkable mechanical properties are the result of their unique

processing and structure. All AHSS are produced by controlling the cooling rate from the austenite or austenite plus ferrite phase, either on the run-out table of the hot mill (for hot-rolled products) or in the cooling section of the continuous annealing furnace (continuously annealed or hot-dip coated products). They are classified into six categories: Dual Phase (DP) steel, Transformation-Induced Plasticity (TRIP) steel, Complex Phase (CP) steel, Martensitic (MS) steel, Ferritic-Bainitic (FB) steel and Twinning-Induced Plasticity (TWIP) steel [3].

What is DP800?

Dual Phase grades consist of a soft matrix called ferrite containing islands of low temperature transformation products, predominately a very hard matrix called martensite. The cold rolled strip is rapidly heated into the inter-critical region forming an austenite–ferrite mixture. The strip is then quenched to room temperature where austenite–martensite transformation proceeds. The strip composition, annealing temperature and quench rate will determine the amount of martensite in the final structure. The strength of DP steels is principally related to the volume fraction of martensite in the structure. There is an austenite to martensite volume change upon quenching from the inter-critical region during annealing. This transformation causes deformation of the soft ferrite matrix, introducing mobile dislocations into the ferrite and at the ferrite/martensite interfaces due to the volume expansion associated with this transformation. Firstly, the movement of these dislocations results in a low yield stress during deformation. Secondly, the dislocation density rapidly increases requiring additional stress to continue deformation, which results in excellent work hardening properties [4]. The number 800 denotes the yield strength of the steel.

In order to achieve the desired mechanical properties of good formability and good work hardening, alloying elements are added in the steel. Table 2 lists the approximate weight percentages of all the alloying elements present in DP800. These alloying elements may oxidise during the annealing process depending on the oxygen partial pressure over the surface. The oxidation phenomenon will be discussed in the following section.

Grade	Fe	C	Mn	Al	Si	B	V
DP800	~ 96.00	~ 0.15	~ 2.05	~ 0.6	~ 0.4	~ 0.002	~ 0.06

Table 2 Alloying elements and their respective weight percentages in DP800.

Annealing

The cold rolling of steel is done at temperatures below the recrystallization temperature. During cold rolling process, the reduction in thickness is due to plastic deformation which occurs by means of dislocation movement. Steel gets hardened because of the build-up of these dislocations. These dislocations reduce the ductility of cold rolled steel making it useless for forming operation. To recover the ductility, cold rolled steels need to undergo an annealing process for the relieving of the stresses that have built up within the microstructure during the process of cold rolling. In this process, the cold rolled steel is heated above its recrystallisation temperature by soaking the steel at that temperature and then cooling it. The annealing is usually carried out under a well specified gas atmosphere to meet the high

demand on the surface of the cold rolled steel. Generally, annealing is performed prior to coating the cold rolled strip steel with Zinc.

Without delving into specifics, the three stages of annealing are [5]:

- ***Stress relief***: This stage takes place at a temperature around ***480-500*** ℃. During this stage, the atoms in the steel move around causing a reduction of internal stresses.
- ***Recrystallisation***: This stage takes place at a temperature around ***500-550*** ℃. Though the internal stresses are removed in the stress relief, new crystals are not formed. To change this, the steel undergoes recrystallization where new crystals start to form. This realigns the atoms and the newly formed grains unite with the cold rolled grains.
- ***Grain growth***: This stage happens during soaking. The grains increase in number and size as they consume the newly formed crystals.

There are two types of annealing processes, Batch Annealing, and Continuous Annealing. A ***Continuous Annealing Line (CAL)*** is used for the production of cold rolled strip for further processing. It is used because of its advantages over batch annealing: (i) better uniformity of the properties along the coil, (ii) better shape and surface properties and cleaner surface, (iii) short processing time leading to higher productivity, and (iv) possibility to produce lower cost high strength grades.

In this process, a decoiler and two loopers are involved. The steel coil is placed at the decoiler. The movement is maintained during heat treatment. Two sets of rolls are present in the looper. The entry looper moves to and from in the heat-treating section to feed the steel coil into it continuously. The exit looper receives the steel coil and thus the continuous movement is maintained during heat treatment. After soaking, the steel roll is allowed to cool down at room temperature [6]. CAL can also be referred to as a ***Continuous Galvanising Line*** if there is galvanisation taking place right after the annealing. Figure 3 provides a schematic of a CAL.

A typical CAL is explained briefly [7]:

- Firstly, the steel strip passes through a ***Pre-Heating Furnace***, where it is heated up to 300 ℃ approximately by the resident heat in the flue gases from the following furnace.
- Then the steel strip first passes through the ***Direct Fired Furnace (DFF)*** where it is heated up rapidly. Removal of the thin rolling oil layer deposited on the steel surface by the cold rolling process occurs within the DFF. During the DFF operation there is a pre-oxidation of the alloying elements and Iron to obtain a relatively thin layer of Iron oxides (<100 nm) which then can be subsequently reduced to metallic Iron during the Radiant Tube Furnace (RTF) action. The annealing atmosphere in the DFF contains small amount of water vapour whose concentration is usually expressed in terms of dew point. In an archetypal DFF operation, the atmosphere is composed of waste combustion gases ***with no free oxygen*** and a ***dew point of ≥ +60 ℃*** [7];

here, the thin Iron oxide layer is formed. This combination has enough partial pressure of oxygen to oxidise Iron.

- The steel strip is annealed primarily in a ***Radiant Tube Furnace (RTF)*** where surface oxides, mainly Iron oxide from the cold rolling operation, are reduced in a short period of time. In the RTF, the heating of the strip takes place by radiation which is transmitted internally through heated tubes and the atmosphere is a Hydrogen-Nitrogen gas mixture with usually around ***5% vol. H_2***. The dew point of the annealing atmosphere in the radiant tube furnace usually ranges from ***-50*** to ***10 °C*** [8]. The oxidation potential in the RTF is reducing for Iron oxides, however it is not low enough to reduce the oxides -or prevent further oxidation- of other selected elements.
- Finally, the steel is rapidly cooled down in the ***Jet Cooled Furnace*** by means of a cold jet of a mixture of nitrogen and Hydrogen to 300°C and it is immersed into the Zinc bath.

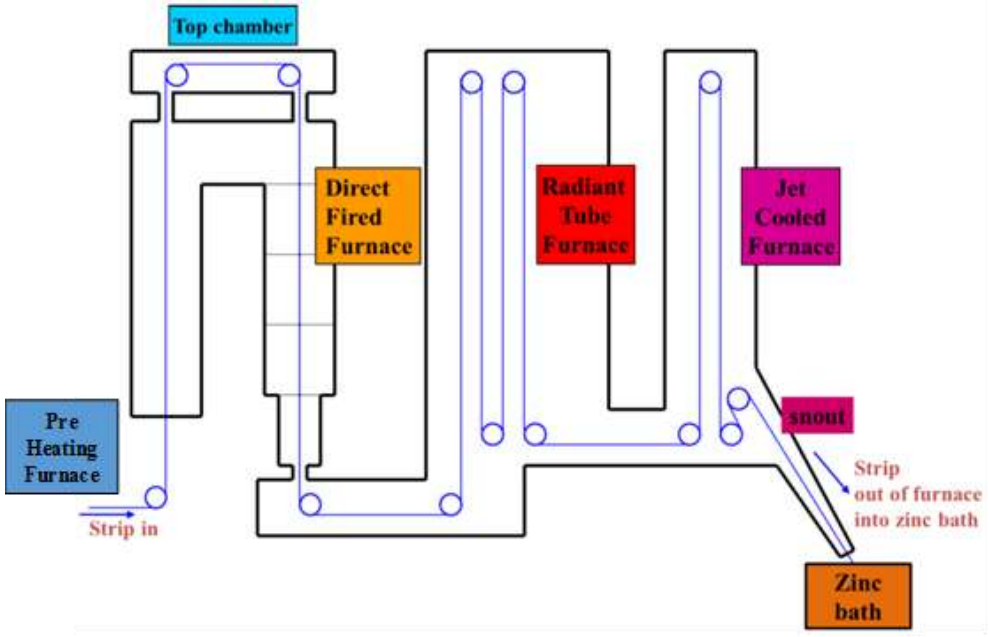

Figure 3 Schematic representation of the annealing section of an industrial continuous galvanizing.

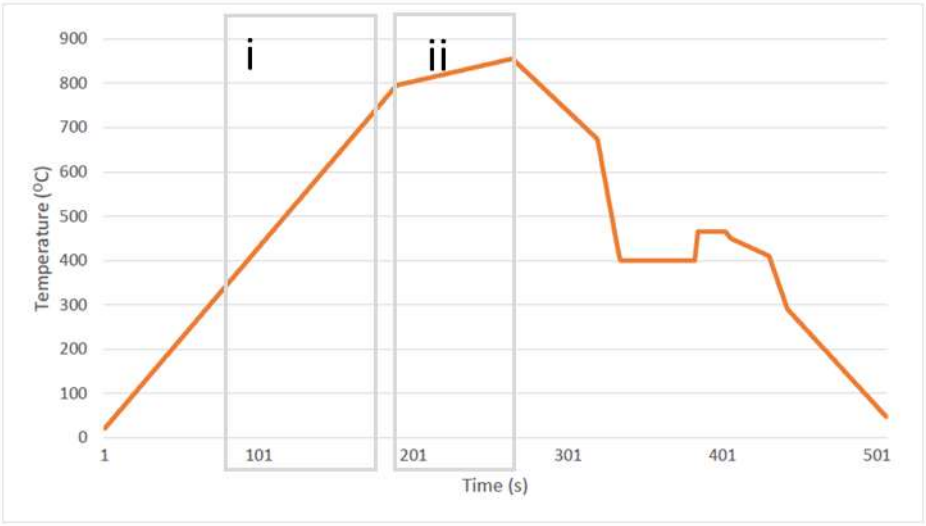

Figure 4 Annealing temperature profile used in this research; (i) DFF section, and, (ii) RTF section.

DFF and RTF are the sub-processes inside annealing that are of interest for this project which have been indicated in the annealing curve shown in Figure 4.

Some of the alloying elements in AHSS (e.g. Mn, Si, Cr and Al etc.) have high affinity to Oxygen and oxidation of these alloying elements is thermodynamically favourable under industrial annealing conditions. The final galvanizing quality of AHSS is, to a large extent, influenced by its high temperature oxidation behaviour during the annealing process because oxides of alloying elements formed on the steel surface can significantly reduce the wettability of liquid Zinc [9], and thus impair the adhesion between Zinc coating and steel substrate. Therefore, one of the biggest challenges for automotive steel makers is to prevent the formation of alloying element oxides at steel surface prior to galvanizing. The oxidation phenomenon is discussed in the subsequent chapter.

Selective Oxidation

Although the annealing atmosphere of the CAL is reducing for iron oxide, it is oxidizing for the alloying elements such as Al, Si, Mn and Cr. Thus, the alloying elements in the steel tend to segregate to the surface upon annealing and form stable oxides. Presence of the oxides of the alloying elements at the surface reduces the wettability between the molten zinc and the steel. Poor wetting between the liquid zinc and the steel surface causes delamination of the zinc coating and occurrence of the bare spots; see Figure 6.

Formation of the stable oxides on the surface is inevitable and their reduction is not feasible from industrial and economical point of view. Hence, an alternative solution is to screen the formed external oxides with a barrier such as iron. Wüstite can be formed on the steel surface by increasing the oxidizing power of the annealing line beyond the equilibrium oxygen partial pressure for Wüstite (FeO) formation (DFF section in Figure 3). The Wüstite layer can be reduced completely during the subsequent annealing line (RTF section in Figure 3) [10]. Ideally, the steel surface should be covered with a layer of iron at the end of the process.

Selective oxidation will occur when there are one or more alloying elements in the steel that can form stable oxides when the oxidising conditions are not enough to oxidise the major element, iron. The implication is that the alloying elements form selective oxides even with the reducing atmosphere conditions of the reduction step in the furnace, i.e., the RTF. As seen in Figure 5, in a normal DFF operation the atmosphere is composed of waste combustion gases with no free oxygen and a dew point higher than + 60 °C; here, a relatively thin Wüstite layer (< 100 nm) is formed. When the steel is introduced in the RTF section, the scale layer is reduced in a short period of time, and the selective alloying elements, which are diffusing towards the surface, have sufficient time to reach it and react with the oxidising agents in the atmosphere, forming subsequently selective oxides at the surface (external oxides) [7] [8].

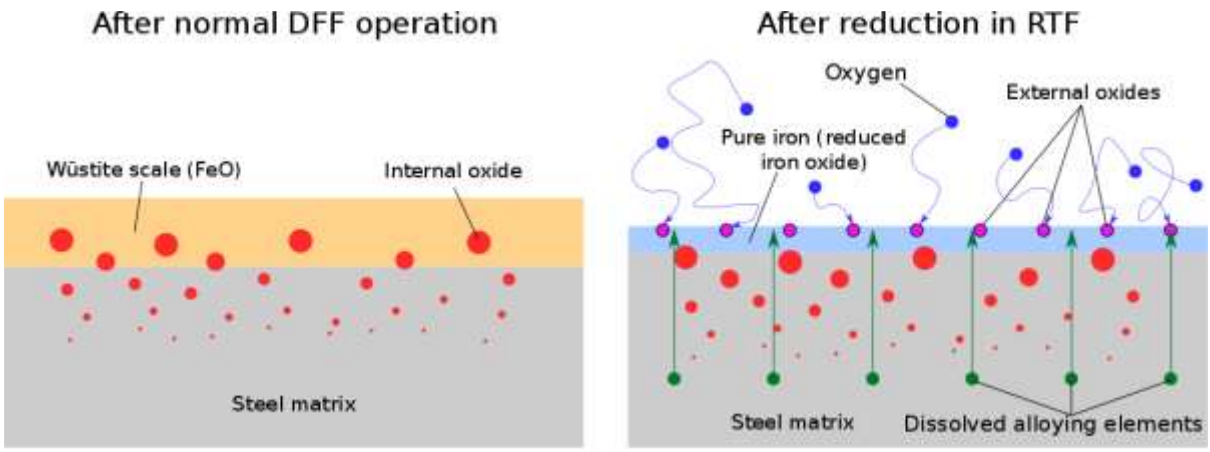

(i) (ii)

Figure 5 Schematic representation of the oxide concentration in the steel surface region in a normal operation after (i) oxidation in the DFF and after (ii) reduction in the RTF [7].

If there is a considerable concentration of selective oxides on the steel surface, the Zinc does not adhere properly and that may cause some superficial defects, such as dewetting, bare spots and/or delamination when bended; see Figure 6. These superficial defects decrease the quality of the steel, or render it unusable.

(i) (ii) (iii)

Figure 6 Defects encountered while coating steel surface with Zinc using Hot Dip Galvanisation: (i) larger bare spots (more than 0.5 cm^2), (ii) smaller bare spots (less than 0.5cm^2), and, (iii) delamination after bending.

As it becomes clear that different dew point temperatures are needed in different sections of the annealing process; Samples were annealed at -30, 0 and 10 °C to compare the changes in concentration of oxides and alloying elements occurring as a function of changing dew point temperatures in the RTF. Analysis of samples annealed at different dew point temperatures are presented in Chapter 4. For the sake of simplicity, the dew point temperature was kept at 0 °C in the RTF process for the samples treated with the EPC process.

Coating Techniques

The major downside for any kind of steel is its poor corrosion resistance. In order to avoid such corrosion and eventual rusting, the AHSS sheets are coated with Zinc or a Zinc based alloy.

Hot Dip Galvanisation

Hot Dip Galvanisation (HDG) is done right after the CAL in which the steel is submerged in a bath of molten Zinc (melting temperature of pure Zn is 420 ℃), so that a protective coating layer is adhered to the steel sheet surface. When the steel is immersed in the bath, Aluminium added to the Zinc bath (0.2-0.4 % wt.) reacts with the steel surface to form an inhibition layer of Iron-Aluminium intermetallic (Fe_2Al_5). It was reported that in the diffusion coating from the bath with 0.2 % Al, $FeZn_7$ phase forms a continuous layer above Fe_2Al_5. Coatings from the bath with 0.3 % Al have separate crystals of $FeZn_7$ phase embedded in the intermetallic layer of Fe_2Al_5. With increasing concentrations of aluminium in the zinc bath, the density and thickness of the Fe_2Al_5 layer increase [11]. This is because the Iron-Aluminium reaction has a much higher driving force than the Iron-Zinc reaction and for this reason, the Iron-Aluminium reaction dominates in Iron-Aluminium-Zinc system even for low Aluminium contents in the molten Zn bath [12].

The thickness of the inhibition layer depends on the immersion time and the weight percent of Aluminium present in the Zinc bath. Its role is to inhibit the reaction of Iron directly with Zinc to form the unfavourable $FeZn_{13}$ intermetallic. The best adherence is achieved when the inhibition layer forms uniformly on the surface of the clean steel. Refer Figure 7 for a pictorial representation of a typical HDG coated sample.

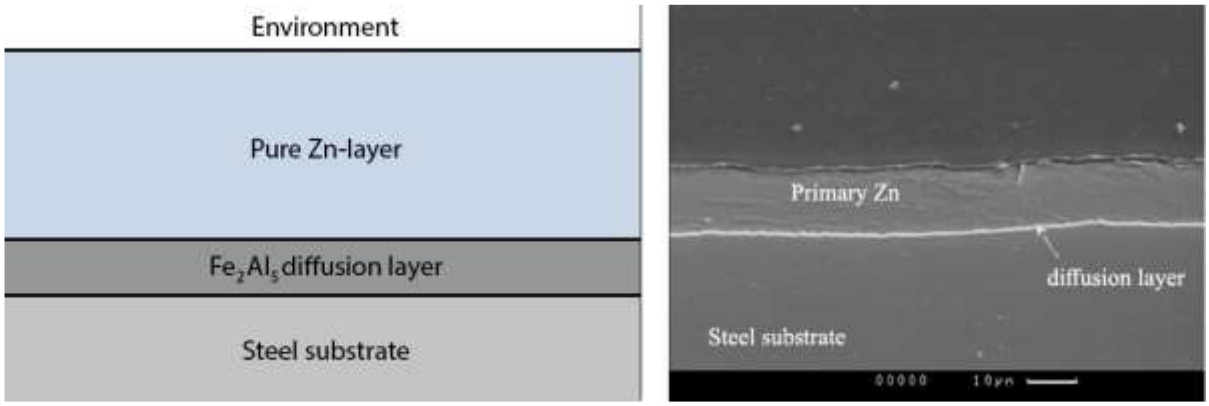

Figure 7 On the left a schematic representation is shown of the layers formed in the galvanized coating. On the right a backscattered electron image of the HDG-coating is displayed. The coating on steel strip displayed is the coating when Aluminium is added to the Zn-bath [13].

However, due to the limited solubility of Aluminium in liquid Zinc, intermetallic phases will precipitate from the bath forming particles commonly referred to "dross". $Fe_2Al_5Zn_x$ floats on top of the surface of the bath and can easily be removed from the bath by skimming its surface. At lower bath Al contents, δ-$FeZn_{10}$ (delta) or ζ-$FeZn_{13}$ (zeta) will precipitate from the bath. These intermetallics have a higher density than liquid Zn and sink to the bottom of the bath and are more difficult to remove. Oxidation of the bath metals (ZnO and Al_2O_3) also contributes to dross formation [13]. Wherever there is an abundance of surface oxides, Aluminium from the bath is consumed at those regions in the reduction of other surface oxides formed during the process of annealing. In other words, the dearth of the inhibition layer in the bare spots, indicate the former presence of selective oxides externally and the Al is consumed reducing the oxides and forming Al_2O_3, not leaving enough Al in the bath and time to form a uniform inhibition layer needed for a uniform Zn coating. The alumina thus formed

which contributes to the formation of oxidic dross floating in the Zn bath are formed by the following reactions:

$$3MnO + 2Al \rightarrow 3Mn + Al_2O_3 \quad \text{(i)}$$
$$Cr_2O_3 + 2Al \rightarrow 2Cr + Al_2O_3 \quad \text{(ii)}$$
$$3SiO_2 + 4Al \rightarrow 3Si + 2Al_2O_3 \quad \text{(iii)}$$

and so on with other oxides less stable than Al_2O_3 [14].

Physical Vapour Deposition

Physical Vapour Deposition (PVD) has several advantages over other conventional coating processes:

- Systematic cost reduction studies carried out by each automotive manufacturer on a model-by-model basis have found that Physical Vapour Deposition is a possible cost-saving alternative to HDG [15].
- It is reported that adding Magnesium with Zinc and Aluminium can increase the corrosion resistance of the coating manifolds as compared to several other Zn binary systems like Zn-Al, Zn-Ti, Zn-Ni and Zn-Cr [16]. A large range of coating compositions are possible with the PVD technique depending upon the application. However, it is not as easy to coat a steel strip in a Zn-Mg bath using HDG as compared to Zn-Mg-Al or Zn-Al coatings because of excessive dross formation. The presence of Al in the Zinc bath suppresses the oxidation of the Mg [17].
- PVD enables coating a substrate using a combination of single layer materials with very different properties. This multilayer concept seems to be the most versatile and promising with respect to properties and performance in almost all fields of application. Different concepts can be combined in a coating, tailored for specific requirements [18].
- Electroplating has the disadvantages of high energy costs, environmental impact and also the risk of Hydrogen embrittlement [19]. PVD is conducted in a closed vacuum chamber and does not involve using hazardous chemicals (as in electroplating), fulfilling the strict environmental regulations [20].
- HDG of steel is performed at ~460°C. At such temperatures, cracking of the substrate can occur during the galvanizing process. These cracks are sometimes covered by the Zn coating and are not detected until the steel structure is subjected to loading, or even until the first inspection [21]. PVD offers a coating deposition rate at lower substrate temperatures (~250°C). At such low temperature ranges, detrimental interface reactions and microstructural evolutions and other high-temperature related issues are minimized [20].

Thus, Physical vapor deposition (PVD) is a promising alternative method for coating deposition on AHSS as compared to HDG or electroplating. For PVD coatings to have good adhesion, the surface of the substrate must be free from oxides, dirt and grease from previous operations. Therefore, EPC might be an attractive pre-surface treatment to remove these surface contaminations and oxides from the steel substrate.

Scope of thesis

The type of steel used in this thesis was cold rolled DP800 steel with the aim of cleaning and removing any contaminants from the surface that could affect the wettability of Zinc during Hot Dip Galvanisation or during Physical Vapour Deposition by using the Electrolytic Plasma Cleaning technique.

Problem Description

To increase the adhesion of Zinc coating on the steel surface, it needs to be devoid of contaminants such as oil, dirt etc., as well as surface oxides of iron and other alloying elements. The focus of this thesis would be on whether Electrolytic Plasma Cleaning is effective enough to be used as a pre-cleaning step prior to coating the steel. Therefore, the successful removal of oxides from the steel surface along with other impurities by the application of a stable plasma is the challenge that will be tackled throughout this thesis.

Research Questions and Objectives

The main objective of this research is to find out whether Electrolytic Plasma Cleaning is a suitable pre-cleaning step for steel surfaces, in particular cold rolled DP800 steels in order to achieve a good coating adhesion. To fulfil this, the following questions need to be answered:

- What are the adjustable parameters that can be optimised during the Electrolytic Plasma Cleaning process to produce a stable plasma that can clean a steel surface effectively?
- How does this process influence the surface chemistry and microstructure? How can the surface be analysed in order to confirm or reject the plausibility of Electrolytic Plasma Cleaning being an effective measure to clean the steel surface?
- Would it be a viable option to scale up as a pre-cleaning step for steel?

Outline

The following chapter, comprises the background and necessary information about the cleaning process in question, i.e., Electrolytic Plasma Cleaning. This chapter also explains the effects of changing the parameters.

The experimental methodology and the surface characterisation techniques used in this work are described in the third chapter.

The fourth and fifth chapters encompass the results obtained from the performed experiments and an explicit discussion of these results, respectively.

The sixth chapter concludes the work done in the thesis and the seventh chapter provides some recommendations for future work.

The eighth chapter focuses on the industrial feasibility of the EPC process and the challenges that the process might come across if it is scaled.

The ninth chapter contains all the appendices and the tenth chapter presents all the references used in this project.

2 Electrolytic Plasma Cleaning

What is Electrolytic Plasma Cleaning?

As mentioned in the second chapter, preparation of any AHSS require annealing which can lead to oxidation of Iron and other alloying elements in the steel. In addition, the storage of cold rolled strip steels involves the application of protective barrier films, oil coating or greasing which can also introduce surface contamination by organic substances. Electrolytic Plasma Cleaning (EPC) is a potential pre-treatment technique in the manufacturing of coated steel components that are prone to formation of mill-scales, pigmented films and oxides. The process becomes even more interesting because it could be integrated as a pre-cleaning measure not only after annealing prior to cold rolling but possibly after hot rolling to remove the thick oxide layer formed as a result.

The process operates at cathodic polarisation of the working electrode. Plasma discharges in the space between the anode and the workpiece provide cavitation effects at the electrode surface as well as heating, melting and re-solidification of a thin surface layer. As a result, the contaminants are removed by pressure waves or are decomposed in the plasma discharge by thermolysis (dissociation of molecules by heat) and radiolysis (dissociation of molecules by radiation) [22]. A typical surface morphology exhibits micro-craters and spheroidal nodules after the EPC treatment; see Figure 8, resulting in a typical 3 to 4-fold increase in surface roughness [23]. This however can be mitigated by application of pulsed current providing control over the impact of plasma discharge on the surface [24]. Formed amorphous or nanostructured surface layers could increase corrosion and erosion resistance [25] but reduce the fatigue strength of the material [24].

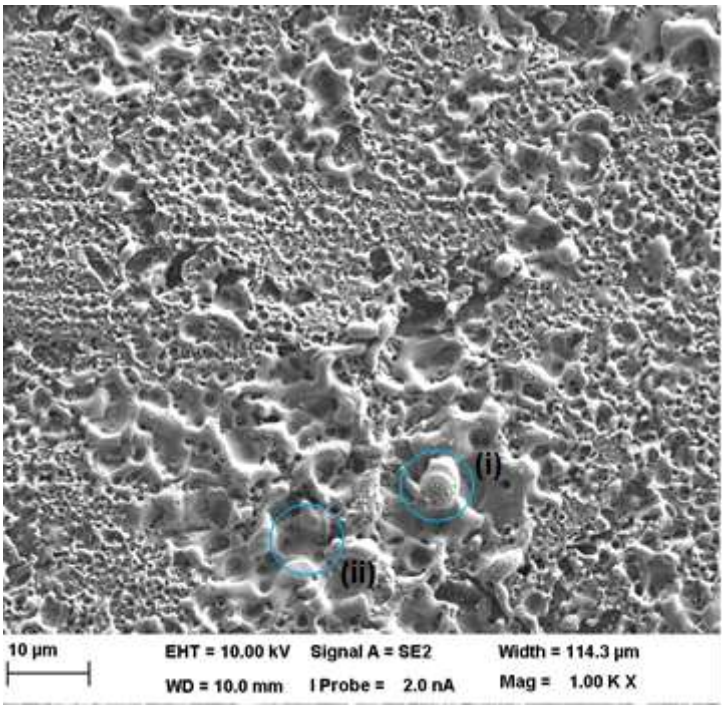

Figure 8 EPC treated sample (i) Spheroidal nodules, and, (ii) Craters.

The electrolysis of aqueous solutions exhibits several electrode processes. Common anode processes include oxygen evolution (iv) and metal oxidation (v). Depending on electrolyte chemical activity, the latter could result in either surface dissolution or formation of an anodic oxide film (vi). Hydrogen evolution (vii) and/or cation reduction (viii) occur on the cathode surface:

$$2H_2O \rightarrow O_2 \uparrow + 4H^+ + 4e^- \quad \text{(iv)}$$

$$Me \rightarrow Me^{n+} + ne^- \quad \text{(v)}$$

$$xMe^{n+} + {}^3/_2\, xnH_2O \rightarrow Me_xO_n + xnH_3O^+ \quad \text{(vi)}$$

$$2H^+ + 2e^- \rightarrow H_2 \uparrow \quad \text{(vii)}$$

$$Cat^{n+} + ne^- \rightarrow Cat^0 \downarrow \quad \text{(viii)}$$

Plasma electrolysis has a similar configuration to a conventional anodising or electroplating process. Figure 10 shows a conventional electrochemical process used for anodising or electroplating. However, the applied electrode potential in all the electrolytic plasma processes is much higher than that of the conventional processes. The bi-phase ***electrode - electrolyte*** system normally encountered in conventional electrolysis is transformed into a four-phase ***electrode - dielectric - gas(plasma) - electrolyte*** couple for the anodic oxidation processing or a three-phase ***electrode - gas(plasma) - electrolyte*** couple for the cathodic processing [25] [26].

In order to understand the mechanism behind the cleaning process, one has to gain an idea about the numerous Electrolytic Plasma Processes that exists.

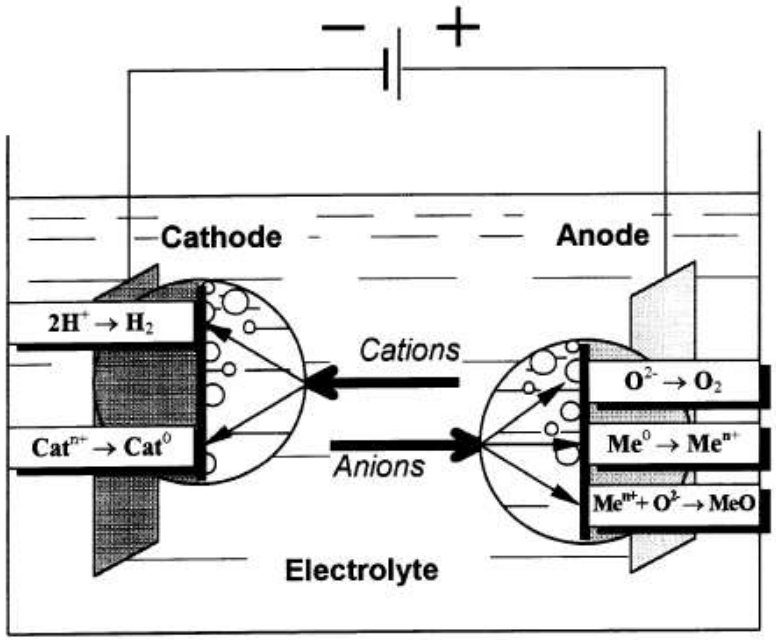

Figure 9 A standard electrochemical cell [26].

Types of Electrolytic Plasma Processes

Attempts have been made to use Electrolytic Plasma Processing (EPP) as an innovative technique of surface treatment and coating for improving surface topographies and coating quality of metallic materials [27] [28] [29].

The formation of plasma on the surface of anodic or cathodic substrate depends on the polarity of applied voltage. For the anodic EPP, it has been usually associated with surface passivation and coating, leading to oxidizing, carburizing, and/or nitriding of the electrode surface [30], for example, Aluminium oxidation reaction is induced on metal-electrolyte interface and with this polarity the surfaces usually yield a layer of oxides, which service as a barrier for corrosion and wearing resistance. The cathodic EPP has been used for preparing metal nanoparticles or depositing metallic coating [25] [29]. Moreover, it has been realized that the cathodic EPP can both remove surface contaminants and form Zn or Al coating on stainless steel and high Nb-TiAl alloys [26] [28].

The other way to differentiate electrolytic plasma discharge is categorizing the process according to the different configurations. The possible configurations and shape of discharge zones have been listed in Figure 10 [31]. The configurations (a) to (g) are the conventional non-contact discharges, where a small gap is kept between electrode and solution. **The type (h) is referred as contact glow discharge, where the electrode is immersed in solution. Such configuration enables vapour formation between metal and liquid. The breakdown voltage, V_B, (>100V, 1 atm) of such a configuration is much lower than the ones for non-contact discharges (>1000V, 1 atm). Hence, contact discharge is a more versatile candidate in real applications.** The target metal also could have contact with liquid frequently under certain condition.

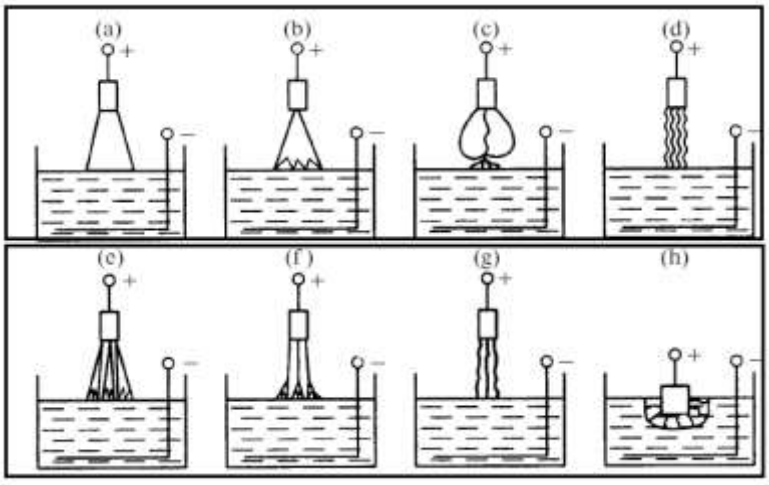

Figure 10 Types of Vapour-air discharge [31].

The following conclusions were arrived upon with regards to the ***Contact Glow Discharge Electrolysis (CGDE)*** phenomenon : (a) vaporization at an electrode, is the prime requisite to initiate the CGDE in an aqueous phase; (b) an electrode-electrolyte area where the conditions help both easier vaporization and easier onset of hydrodynamic instabilities would be the location of CGDE; and (c) the nature of the glow discharges at an anode is quite different from that at a cathode [32].

Process Description

Cathodic EPP for cleaning AHSS involves two characteristic phenomena- (i) electrolysis of a liquid environment by application of different electrical potentials between the workpiece material(cathode) and an anode at lower voltage; and (ii) the production of an electrical discharge at, or in the vicinity of, the cathode at higher voltage. Hydrogen generation by electrolysis is marked by bubble formation. **At sufficiently high voltages a normal electrolysis switches over to the CGDE in which glow discharges take place across a gaseous envelope covering the cathode. The transition from normal electrolysis to CGDE is marked by the growth of a gaseous sheath over the cathode, which indicates the initiation of ionisation. Compared to lower voltages, bubble formation due to electrolysis continues but at a reduced rate.** A typical electrode current–voltage characteristic curve of the electrolytic cathodic process is shown in Figure 11.

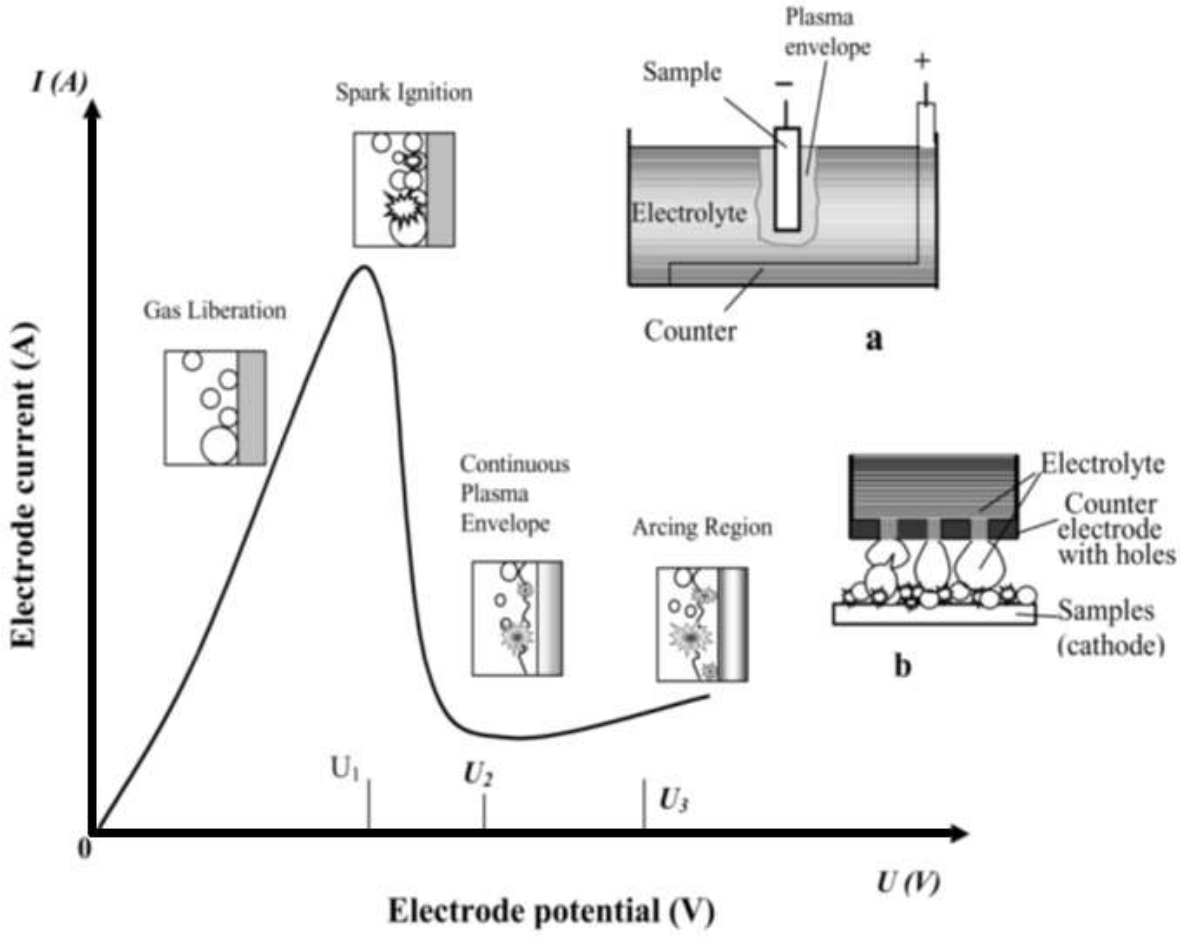

Figure 11 Current-voltage dependence in cathodic electrolytic plasma discharge [25].

The normal glow discharge zone, U_1–U_2, is the work region, where the electrode current decreases but plasma intensity increases when the electrode voltage increases from U_1 to U_2. U_1 is also the breakdown voltage. The cathodic workpiece can be either immersed in the electrolyte Figure 11 (a), or electrolyte can be poured over it through perforations in the anode Figure 11 (b). However, the corresponding slope of the electrode current–voltage curve in the U_1–U_2 segment is different in these two cases. For the configuration shown in Figure

11 (a) the current sharply drops from the highest point to the lowest point when the electrode voltage increases from U_1 to U_2. For the configuration in Figure 11 (b) the slope of the U_1–U_2 line (i.e. current reduction rate) is less steep than that for Figure 11 (a). Irregular sparking is observed when U_1 is reached which becomes continuous with increasing electrode voltage till U_2. When the voltage is at U_2, the cathode is surrounded by a continuous gaseous vapor plasma, which is characterized by a significant drop in current. This is the operating regime of EPC, where plasma is stable, and where controlled surface treatment can be carried out. This regime was discovered by Kellogg and hence is called the ***Kellogg region*** [23]. After U_3, there is continuous formation of arc which melts the metal undesirably.

As mentioned, contact discharge configurations, Figure 10 (h) and Figure 11 (a) have a breakdown voltage lower than that of their non-contact counterparts. Therefore, a submersible contact discharge setup was designed and built. A sharp drop in current is expected when the breakdown voltage is reached.

For EPC, Sodium Carbonate (Na_2CO_3) is added to demineralised water which participates in the process but ultimately remains in solution. The ions due to adsorption gradually concentrate on the Hydrogen bubble surface and the bubbles thus turn into small capacitors. The electrical field between the positive ions at the bubble surface and the negatively charged steel surface ionizes the Hydrogen gas in the bubble, resulting in a high temperature plasma. This occurs quickly once Hydrogen starts forming.

Kinetics of Plasma Discharge

The plasma in this study is mostly composed from Hydrogen. However, one report suggests the presence of plasma from water vapour as well [31]. Plasma formation takes place during vaporisation. During EPC, vapour formation takes place by two ways- (i) electrochemical reactions, and, (ii) Joule heating.

Gas formation through electrochemical reactions

In the initial stage of EPC (till U_2), the temperature of the electrode is not high enough to evaporate the surrounding electrolyte and the electrolyte remains as liquid. The only gas evolving mechanism is by the electrolysis of water molecules which produces H_2 gas at the cathode (hydrolysis). The amount of gas evolved follows Faraday's law in electrochemistry which is given by:

$$m = \frac{qM_{mol}}{Fz} \Rightarrow m = \frac{\int IdtM_{mol}}{Fz} \qquad \text{where } q = \int Idt \qquad \text{(ix)}$$

where, m is the mass of Hydrogen gas generated at the cathode, q is total charge involved in reaction, I is the current passing through active surface, M_{mol} is molar mass of Hydrogen in grams/mole = 2.016 and z is the number of charges involved in the reduction/oxidation reaction. Here, M_{mol}, F and z are constant. Any change in the charge transfer can influence the production of Hydrogen gas. Hence, changing input current or current related properties can influence the hydrogen production.

In order to generate a plasma, a continuous vapour gas envelope has to be formed which results in the drop of current. Therefore, as the power increases, the current drops and hence, the liberation of Hydrogen gas is lowered with increasing power.

For cathodic EPPs, hydrolysis occurs when an external power is supplied. Microscopic sized Hydrogen bubbles are generated and dissolved in electrolyte, Equation (xi). The dissolved H_2 will coalesce to form macroscopic bubbles as the local electrolyte become saturated. The nucleation of macroscopic bubbles usually initiates at local defects, for instance, local concaved regions [31].

The anodic and cathodic reactions are given below:

Anode: $2H_2O \rightarrow O_2 + 4H^+ + 4e^-$ (x)

Cathode: $2H^+ + 2e^- \rightarrow H_2;$ (xi)

Gas formation through Joule heating

Since a gaseous phase is essential for plasma initiation, it is found that when the current starts to drop across the electrodes, there is an increase in temperature, locally, that vaporises the electrolyte around the interaction area. To demonstrate the local Joule heating effect, a simplified heat transfer model is given in the following equation, assuming no flow through the anode.

$$Q_1 = mC_P\Delta T + m\Delta H_{vap} \quad \text{(xii)}$$

where Q_1 is the energy required to vaporise m grams of electrolyte by raising the temperature from room to boiling temperature, ΔT, C_P is the specific heat capacity of water at constant pressure and ΔH_{vap} is the latent heat of vaporisation of the given electrolyte, the values of which are provided in Table 3. Here, water can be assumed as the electrolyte which is vaporised to steam due to the very low concentrations of salt used.

Therefore, water vapour is formed by Joule heating and Hydrogen gas by the electrolysis of water at higher voltages. Although the amount of hydrogen produced reduces comparatively as the current drops at high voltages. The formation of gases does not contribute to the formation of plasma rather the discharge is initiated because of the vaporisation [32]. Keeping this in mind, additional energy needs to be supplied to ionise the Hydrogen and water vapour thus produced in between the electrodes; see Equation (xiv). It is worth noting that the water vapor has a lower ionization potential compared to Hydrogen; see Table 3.

$$Q_{plasma} = Q_1 + Q_{ionisation\ potential\ H_2} + Q_{ionisation\ potential\ H_2O} \quad \text{(xiii)}$$

Specific Heat Capacity of water (kJ/kgK, @60 ℃)		3.97
Latent heat of vaporisation of water (kJ/kg)		2260
Ionisation Potential (J)	Water Vapour	2.01×10^{-18}
	Hydrogen	2.47×10^{-18}

Table 3 Numerical values of important intrinsic parameters.

Parameters

The parameters taken into account in this study were divided categorically; ones which directly affected the plasma generation, others which influenced the steel surface, and parameters which influenced both the steel surface and the plasma; see Table 4.

Parameters	
Plasma	**Surface**
Concentration of Salt	Geometry
Temperature of Electrolyte	Treatment Time
Material of the Anode	
Inter-Electrode Gap	
Flow Rate	

Table 4 Parameters taken into consideration and their classification.

Concentration of Salt

Concentration of Na_2CO_3 solution is directly proportional to the conductivity of the bath. More current is running through the circuit when the concentration is increased for a given voltage. Therefore, higher current ensures more hydrogen formation by electrolysis; see Equation (ix).

Diluting the Na_2CO_3 solution meant that there is an increase in the circuit resistance as fewer ions are available for charge transport. This leads to a reduction in the conductivity of the circuit which implies that more power is needed to reach a given breakdown voltage.

$NaHCO_3$ solution was used as electrolyte for the plasma process by [23]. One literature suggested using Na_2CO_3 or K_2CO_3 solutions in concentrations of ≤500 g/L [30]. 40 g/L and 75g/L of Na_2CO_3 were used by [27] and [31], respectively. There was neither a consistency in literature when it came to the quantity of salt used nor did any literature shed light on why a particular quantity was needed. For the sake of standardisation and to draw comparisons with results found in literature, the experiments in this research have been performed using 10 to 100 grams of Na_2CO_3 in 20 L of demineralised water which roughly translates to 0.005 to 0.05 M and is orders of magnitude less than what is reported in existing literature. In this research an estimate was made of how much Na_2CO_3 salt would be needed which is presented in Chapter 5.

Temperature of Electrolyte

At lower temperature, the Na_2CO_3 remains as a solid inside the bath. As the temperature of the bath approaches 60-70 °C, the plasma formation is more continuous and arcing is reduced. In metallic anodes, increasing temperature means increased resistance; see Equation (xiv) which means that there is an increase in Joule heating essential for vaporisation. Resistance of graphite materials was found to increase monotonically with increasing temperature up to 3000 °C after passing through its minimum at around 1000 °C [33]. The resistivity of water reduces with increasing temperature.

$$\rho_t = \rho_0 [1 + \alpha (T - T_0)] \quad \text{(xiv)}$$

where ρ_0 is the resistivity at a standard temperature, ρ_t is the resistivity at T °C, T_o is the reference temperature and α is the temperature coefficient of resistivity. The temperature increases during of Joule heating which results in the increase of resistivity.

The temperature can reach as high as 2000 °C, locally, where the plasma interacts with the surface. This instantaneous high local temperature results in the local melting of the workpiece surface. The relatively cool electrolyte (≤100 °C) surrounding the hot gas bubbles causes the cooling of plasma and the workpiece. Due to the high surface temperature followed by quenching, microstructural changes and formation of metastable structures can take place on the workpiece surface [29] [30].

Anode

The anodes to be described and evaluated in this thesis are listed in Table 5.

Material	Geometry
Copper	Height = 20 mm Diameter = 20 mm No. of holes= 4
	Height = 20 mm Diameter = 20 mm No. of holes= 37
Steel	Height = 20 mm Diameter = 20 mm No. of holes= 4
Stainless-Steel	Height = 20 mm Diameter = 20 mm No. of holes= 37
Graphite	Height = 20 mm Diameter = 20 mm No. of holes= 4 (on the side of the cylinder)
	Height = 20 mm Diameter = 20 mm No. of holes= 37
	Height = 20mm $Diameter_1$ = 20mm $Diameter_2$ = 16mm
Titanium	Height = 20 mm Diameter = 15 mm Porous

Table 5 Types of anode used; the material and the geometry used.

Material

In order to initiate this project, the material for the anode that gave the best surface properties had to be selected. For this purpose, five types of anode materials were used. Copper, Steel, Stainless-Steel, 3D printed Titanium and Graphite. These materials were chosen because previous researches have shown deposition of Zinc on the steel surface using a Zinc anode during the EPP process [25] [28]. The deposition of Zinc is possible because of its relatively low melting point. It was decided to select metals with a higher melting points than that of Zinc and gage the temperature reached at the interaction sight by checking which anode melts

and which doesn't. Graphite has been the most widely used anode material in literatures. Hence, Graphite was also included along with the metals.

The metal anodes were unsuitable for cleaning because deposits of the anode and corresponding oxides of the anode material were found on the steel surface; see Chapter 4. This is attributed to the high local temperatures and electric field in the interaction region.

No deposits were reported on the steel surface by literature when a graphite anode was used [28] [29] [34] [35] . Within this project, it is found that the use of Graphite as anode keeps the electrolyte comparatively clean from debris. Furthermore, no deposits from the anode were found on the steel from the Graphite anode. Figure 12 shows a damaged Titanium anode which has melted and partially oxidised. At high temperatures, the anode tends to melt and oxidise instantaneously which leads to oxide deposition on the steel substrate. Such oxides are undesirable for coating purposes.

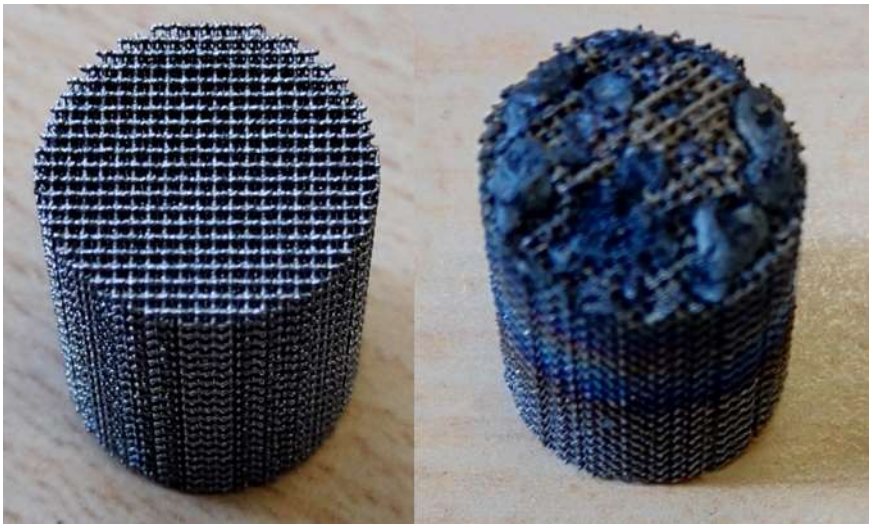

(i) (ii)

Figure 12 (i) New, and, (ii) Used (melted and oxidized) titanium 3D printed anode.

Geometry

Holes were made in the anode to facilitate the flow of electrolyte through it. Initially, while utilising the metal anodes, these holes were fewer and larger in diameter. As the project progressed, it was decided to reduce the size of the holes and increase their numbers so that the flow of electrolyte through the anode would act as a coolant and prevent the anode from melting and falling on the workpiece. This perforated geometry was also utilised for the graphite anode. The shockwaves from the plasma generation interacts with the graphite near these perforations; being softer than the metals, the graphite disintegrated around these sites on the application of higher power; see Figure 13.

(i) (ii)

Figure 13 (i) Unused graphite anode, and, (ii) Used graphite anode.

The critical current density under conditions of the appearance of stable plasma is known to depend on a number of factors, including the shape (planar or round), size and orientation of electrode [30]. For example, when the anode cross-section area reduces with the increasing number of holes, the formation of a stable plasma should take place at a lower voltage as the current density increases. The time interval for the formation of gas bubbles also drastically reduces with an increase in the current density [36]. A solid anode with one duct in between for electrolyte flow having similar cross-section area as the perforated graphite anode was sought; see Figure 47-(i). Using a solid graphite anode improved the overall surface; refer Results and Discussion.

Inter-electrode distance

Prior to finding an appropriate inter-electrode distance, submergence needs to be ensured for CGDE. Partial submergence ensured generation of plasma but it wasn't regular and the effects of the irregular plasma is visible macroscopically in Figure 14.

(i) (ii)

Figure 14 Samples of DP800 treated with a (i) partially submerged, and, (ii) fully submerged Stainless-Steel anode.

The gap between the anode and the cathode affect the capacitance effect of the Na^+ ions, the Hydrogen bubbles and the negative workpiece. Closer spacing between the electrodes results in a greater electric field (V/d=E) and higher current because of less distance for the charges to travel which means more generation of Hydrogen gas; refer Equation (ix). This, however, changes when the flow is decoupled from the anode where changing distance only results in changing electric field. It was observed that at higher inter-electrode gaps the plasma could

not interact with the cathode and was only limited around the anode; see Figure 15 (ii). The plasma, thus formed, only manages to form a few arcs between the electrodes during the whole treatment time; refer Figure 16. Thus, for this project, the gap was limited between 1 mm to 6 mm as it was seen that after a distance of approximately 4 to 5 mm the plasma was unable to interact with the steel surface continuously leading to arcing; see Figure 16 (i), for the variation in the surface due to changing electrode distance.

(i) (ii)

Figure 15 Plasma when the gap is: (i) 1mm, and, (ii) 5mm.

Flow rate/Speed

The flow rate, $\dot{f}$ is directly proportional to the conductivity of the circuit. Moreover, increasing flow rate leads to a cooling effect locally (more turbulence at the interaction site). This increases the required energy to form a stable plasma as more energy is involved in the water vaporisation due to the additional effect. The turbulence has a detrimental effect on plasma electrolysis because it inhibits the formation of Hydrogen bubbles on the cathode surface. Higher flow rates negatively affected the formation of plasma [37] . When the flow was varied between 120 to 600 L/hr, the plasma cleaning was not satisfactory after ≈ 360 L/hr [37].

The effect of flow rate on the generation of plasma is twofold:

- Increasing flow rate increases cooling locally by increasing turbulence, thus increasing the power to generate the plasma.
- The increased turbulence hinders the formation of Hydrogen by electrolysis as well as the bubble formation on the workpiece, thus increasing the power required to generate the plasma.

A lower flow rate means that the cooling effect at the interaction site is reduced. This lowers the treatment time as the steel surface burns and blackens in the absence of adequate cooling. On the other hand, at a higher flow, more power is needed to achieve the plasma thus leading to a dull, impacted surface. Refer Figure 16 (ii) to interpret what is happening on the surface of the steel due to changing flow.

Frequency & Treatment time

The most effective cleaning was achieved when a pulsed DC source was used with a frequency of 10 kHz [24]. The power supply used for this project had a range of 10 to 200 kHz. When varied during experiments, frequency was found to be a "fine-tuning" parameter, and hence, was not considered in this investigation.

[28] found that as the treatment time increased the surface became rougher after varying treatment times from 0 to 180 seconds on a Stainless-Steel sample. [35] found that the maximum cleaning was achieved at ≅ 40 seconds for Q195 Steels. The increase in surface roughness was attributed to the lack of energy initially to form the plasma, resulting in small change in the surface roughness of the steel. It was found that as the reaction continued, the breakdown of electrolytic plasma bubbles constantly released a large amount of energy on the sample surface, resulting in the surface roughness increasing. This surge in energy is consistent with the results of [32]. Joule heating leads to surface melting. Prolonged treatment can make the steel soft, increasing the number of defects on the surface and the formation of multiple discharging channels. All of these have a great effect on the increase of discharge hole diameter (i.e., roughness). It was observed that the surface was restructured considerably, if treatment exceeded 45 seconds. Therefore, the treatment times were kept between 5 seconds and 45 seconds; refer Figure 16 (iii) to understand the effect of treatment time on the surface.

(i) (ii) (iii)

Figure 16 DP800 Steel surface after (i. a) 1 mm, and, (i. b) 5 mm inter-electrode distance, (ii. a) $\dot{f}$=60 L/hr (ii. b) $\dot{f}$=160 L/hr, (iii. a) 50 seconds, and, (iii. b) 20 seconds.

These considerations based on the parameters defined above lead to the following ranges.

Parameters	Minimum	Maximum
Concentration of salt	0.0047M of Na_2CO_3	0.047M of Na_2CO_3
Temperature	30 °C	80 °C
Inter-electrode distance	1 mm	6 mm
Flow Rate	60 L/hr	200 L/hr
Current Density (for 10A, based on geometry)	3.5 A/cm²	3.8 A/cm²
Resistivity (based on material of anode)	$1.68 \times 10^{-8}\ \Omega m$	$1.5 \times 10^{-5}\ \Omega m$
Time	5 sec	45 sec

Table 6 Extremities of the parameters used.

3 Experimentation

Experimental Setup

The EPC setup is as shown in Figure 17 follows. The workpiece (9) is held in place using the holder (10) and submerged in the electrolyte inside a plexiglass container (1) of dimensions $295 \times 487 \times 536$ mm^3. The workpiece is grounded. The anode (8) is housed inside the PVC tube (6) of 24 mm in diameter, and is connected to the main power supply (11), a DC Pinnacle Plus+ Series Single Magnetron Power Supply with maximum output of 5 kW. The anode is connected to the main power supply using an insulated copper rod (7) which supplies power to the anode. This copper rod resides inside the PVC tube as well. When the container is filled with the electrolyte, a submersible pump (3) from Rule-Industries (model no. iL280P 12 Volt DC – 4.5 Amp) the pump power supply (4) is used to circulate the electrolyte. The flow rate is changed by using this power supply. The electrolyte enters the pump inlet (2) from where it goes through the flow meter (5) which indicates the current flow rate and re-enters the bath after going through the PVC tube and perforations or holes in the anode. The gap between the two electrodes is adjusted using a height controller (12) which translates rotational input into a longitudinal travel output.

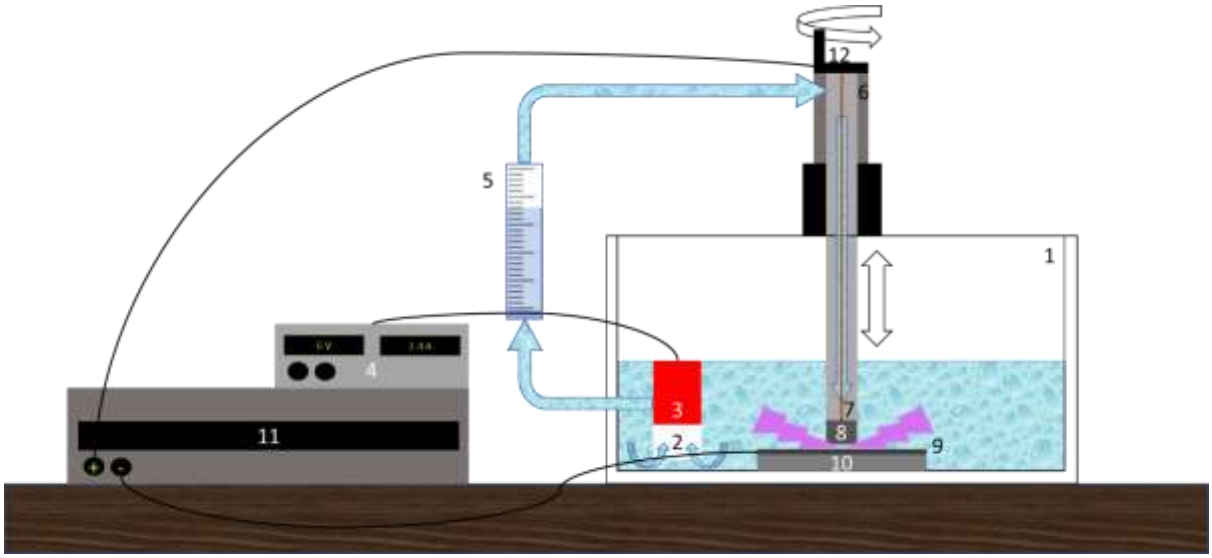

Figure 17 Schematic representation of the EPC setup: 1) Plexiglass container containing the Na_2CO_3 electrolyte (295x487x536 mm^3), 2) Pump inlet, 3) Pump, 4) Pump power supply, 5) Flow meter, 6) Hollow PVC tube, 7) Electrical contact to the anode housed inside the PVC tube, 8) Anode housed inside the PVC tube, 9) Workpiece, 10) Stainless Steel workpiece holder, 11) Plasma power supply, and, 12) Height controller for the PVC tube to change the anode-cathode gap.

A similar setup was developed to study the effects of de-coupling the flow through the anode; see Figure 18. Rather than having the flow through the anode, it was separated altogether from the anode.

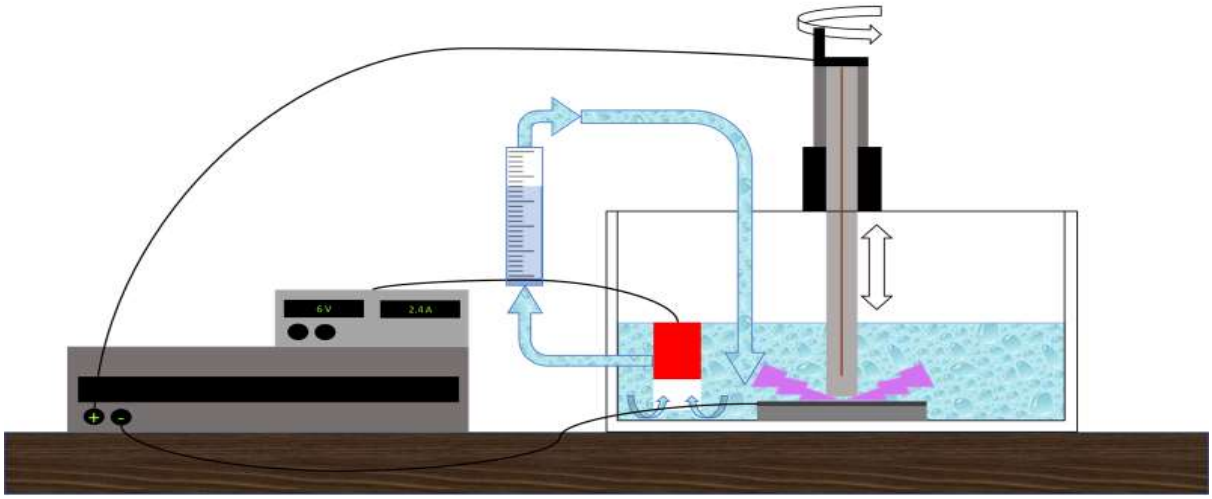

Figure 18 Setup with de-coupled flow.

Setup Limitations

- The temperature of the bath is not controllable within the setup. The Joule heating phenomenon increases the temperature of the electrolyte to operating conditions. Cooling the bath implied not using it for a few minutes. There wasn't a robust temperature controller.
- As the temperature of the bath increased over time, the water from the electrolyte also started to vaporise which led to an increase in the concentration of the solution as the experiments progressed over the course of the day.
- The system becomes excessively sensitive to changing height as the inter-electrode gap is reduced. This posed a challenge at lower heights as the height controller for the anode was not as accurate. On top of that, even the slightest of curvature induced while cutting the samples affected the treatment by treating only the side that had a lower gap owing to the curvature; see Figure 19.

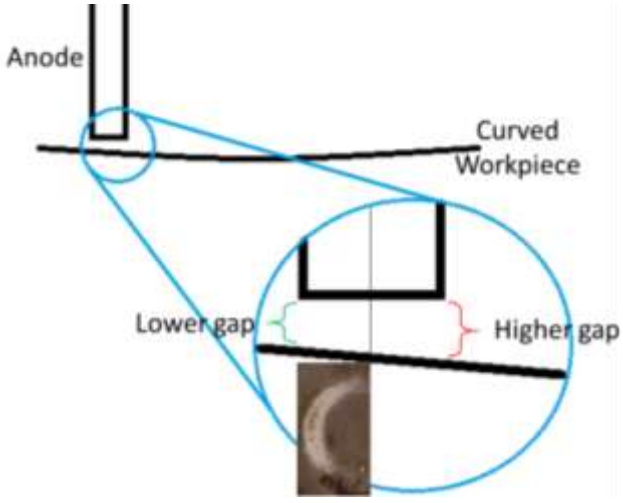

Figure 19 Half-treated sample due to the height difference introduced by the curvature of the steel sample.

- When using a graphite anode, the graphite particles pollute the solution turning it black in colour. Graphite is known for its conductive properties. Therefore, as the experiments progressed the overall conductivity of the system may have been elevated because of the dispersed graphite particles polluting the bath.

These limitations did hinder the investigation but not to the extent where they jeopardise the analysis.

Procedure

- A sample of DP800 is annealed at 50 °C dew point temperature inside the DFF and 0 °C dew point inside the RTF following the annealing curve given in Figure 4 after cold rolling. This annealed sample is fixed on the Stainless-Steel workpiece holder; Figure 17-10.
- Na_2CO_3 salt along with demineralised water is poured in the container as per the prescribed molarity. 20 litres of demineralised water were used for this purpose.
- The water pump is started to ensure that the Na_2CO_3 is mixed thoroughly with the water.
- The anode-cathode gap is adjusted.
- Next, the flow rate is set.
- Then the main power supply is switched on and an input power is set in order to obtain a plasma.

Methodology

Firstly, a dew point temperature was needed so that all the samples used in the experiments have the same or comparable amounts of surface oxides. Hence, 0 °C was chosen as the standard dew point for all the experiments. The samples were annealed following the curve given in Figure 4; at 50 °C dew point in the DFF and 0 °C in the RTF. The annealed samples underwent EPC treatment with different anodes and geometries. Numerous advanced characterisation and analysis techniques were used to evaluate the treated steel surface. These techniques are elaborated in the next sub-section. The desired material and geometry for the anode were established prior to finding an optimal working range for the remaining parameters in order to achieve a stable plasma.

In this project two problems were tackled problems simultaneously; to define a parametric range for production of a stable plasma and to find which parameters work best for the treatment. Having two major parts in this project meant that before trying to define the optimal plasma parameters, the anode material and geometry needed to be confirmed so that further experiments could be carried out using the same anode.

Analysis Techniques

The steel substrate after treatment was evaluated based on several criteria, namely, surface morphology, wettability, topography and chemistry to find which anode material and

geometry gave the best results in terms of removal of oxides, roughness and wettability. Some of the analysis techniques mentioned below can provide information on the surface as well as about the sub-surface conditions.

Scanning Electron Microscopy

Scanning Electron Microscopy (SEM) is a characterization technique that images the sample surface by scanning it with a high-energy beam of electrons in a raster like pattern. The electrons interact with the sample at and close to the surface (up to a few 100 nm). Secondary and backscattered electrons are detected, each provide different information as they are the results of different interactions; see Figure 20. In combination with Energy Dispersive X-ray Spectroscopy (EDS), information about the sample's surface topography and chemical composition is provided.

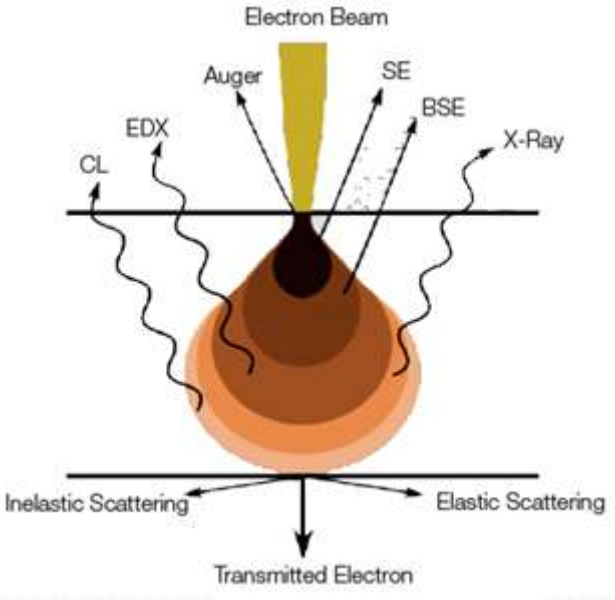

Figure 20 Schematic of the interaction volume of Scanning Electron Microscopy.

Secondary Electrons

Secondary electrons are the result of electron emission of surface atoms, initiated by the inelastic collisions with the 'primary' high-energy electrons. These secondary electrons have a low energy, and require a mean free path to escape from the sample. Only for the top few nm of the sample, the secondary electrons are unaffected. Therefore, secondary electrons provide information about the morphology of the sample surface.

Backscattered electrons

Backscattered electrons are reflected 'primary' electrons, which have elastically collided with the atoms. These electrons provide information about the composition of the sample. As the backscattered electrons have a higher energy than secondary electrons, they provide compositional information up to 100 nm from the surface. In such an image, the (average) kinetic energy of the elements is displayed as function of brightness: heavier elements will occur brighter than light elements.

Energy Dispersive X-ray Spectroscopy

Often, SEM imaging is combined with energy dispersive EDS. EDS is a technique to determine the elemental composition of the sample surface. It is based on the interaction of the 'primary' electrons with atoms, with the emission of X-rays as a result. As each element has a unique electron structure, the wavelength of the emitted X-rays is a characteristic of the element. EDS provides compositional information up to $\approx 1\ \mu$m.

Glow Discharge Optical Emission Spectroscopy

Glow Discharge Optical Emission Spectroscopy (GDOES) is a destructive technique that is used to obtain the elemental composition of the sample from the surface down to more than 150 microns with a depth resolution that can be as good as 1 nm. It combines plasma sputtering, and, electron excitation and relaxation to detect elements. During the analysis, an Argon plasma is generated by applying a voltage between the anode probe and the cathode workpiece. Ionised Argon atoms are accelerated towards the sample and the sample surface is bombarded with Argon ions which sputter away atoms from the sample surface. These sputtered atoms are excited in the plasma and upon relaxation (de-excitement) they emit photons with a characteristic wavelength. The number of photons generated and their corresponding wavelengths are then used to determine the composition of the sputtered layer.

Sessile Drop Experiment

The sessile drop is the standard arrangement for optical measurement of the contact angle using drop shape analysis. Drop shape analysis is an image analysis method for determining the contact angle from the shadow image of a sessile drop. The contact angle is given by the angle between the calculated drop shape function and the sample surface, the projection of which in the drop image is referred to as the baseline. It is a measure of the wettability of a solid by a liquid [38].

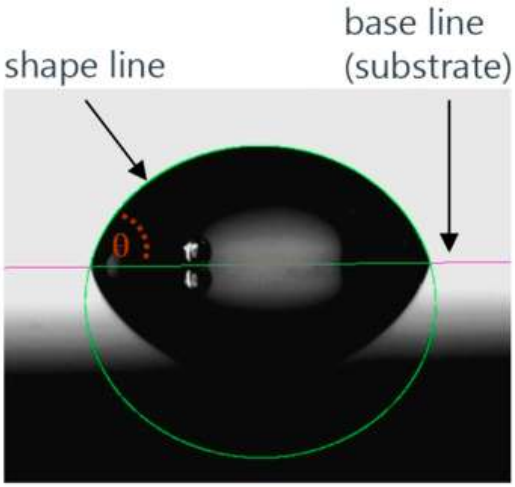

Figure 21 Sessile drop with fitted contour (shown in green).

In the case of complete wetting (spreading), the contact angle is 0°. Between 0° and 90°, the solid is wettable and above 90° it is not wettable [39].

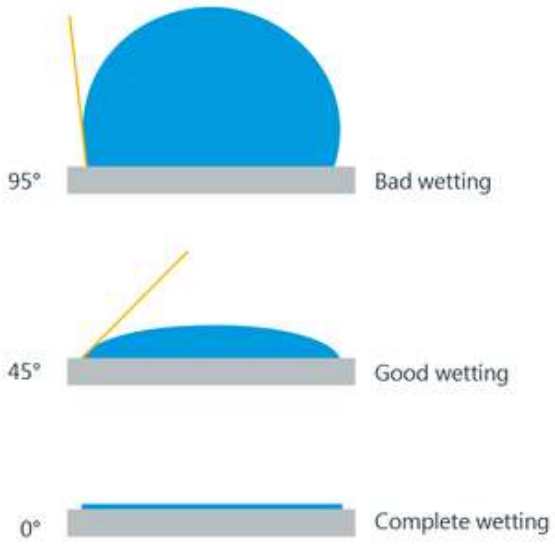

Figure 22 Contact angle on different materials.

The static contact angles were measured for 15 seconds and an average of that was taken as a single measurement. This was repeated 3 times for each sample to check for consistency in measurement. The contact angle can vary as a function of time and location. Inhomogeneities and changes in wetting over time can, therefore, be detected by means of the static contact angle measurements. The EPC treatment modifies the surface and whether the modifications are homogenous or not can be determined by static contact angle measurements.

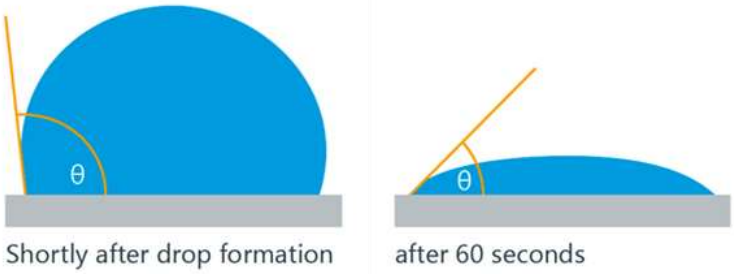

Figure 23 Changing contact angle with respect to time.

Profilometry

Profilometry is a technique used to extract topographical data from a surface. This can be a single point, a line scan or even a full 3D scan. The purpose of profilometry is to get surface morphology, step heights and surface roughness. This can be done using a physical probe or by using light. Both the techniques have been used in this project and are elaborated below.

Stylus Profilometry

Stylus profilometers use a probe to detect the surface, physically moving a probe along the surface in order to acquire the surface height; see Figure 24. This is done mechanically with a feedback loop that monitors the force from the sample pushing up against the probe as it scans along the surface. A feedback system is used to keep the arm with a specific amount of

torque on it, known as the 'setpoint'. The changes in the Z position of the arm holder can then be used to reconstruct the surface.

Stylus profilometry requires force feedback and physically touching the surface, so while it is extremely sensitive and provides high Z resolution; see Figure 24 for orientation, it is sensitive to soft surfaces and the probe can become contaminated by the surface. This technique can also be destructive to some surfaces. Since a stylus profilometer involves physical movements in X, Y and Z while maintaining contact with the surface, it is slower than non-contact techniques. The stylus tip size and shape can influence the measurements and limit the lateral resolution.

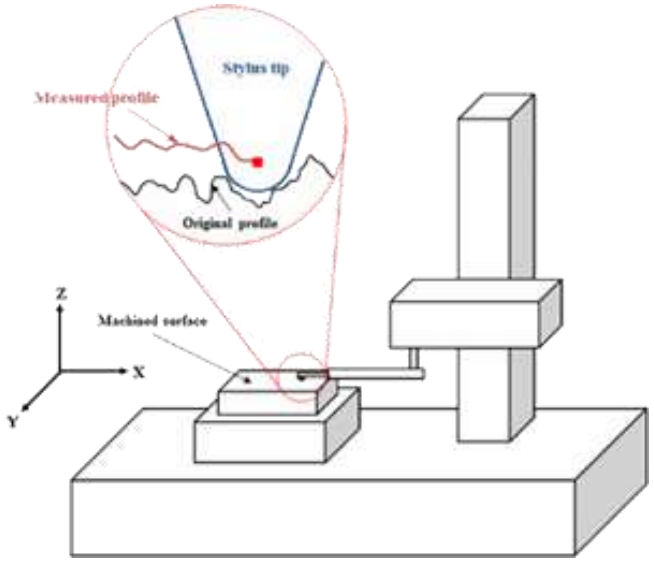

Figure 24 Schematic of a stylus profilometer.

Confocal microscopy

Confocal microscopy is an optical method for obtaining three-dimensional images of surface textures and objects. With a reflected-light method, the roughness of a surface can be accurately measured without contact.

With a confocal microscope, a point light source is generated with the help of a pinhole aperture. The light returning from the object passes through a second pinhole aperture, or the same aperture a second time, and impinges on the detector, as a rule a video camera. An image of the illuminated object area is formed with a very low depth of field, i.e. the light intensity reduces sharply above and below the focal plane so that only this plane is displayed.

A rotating aperture disk with holes arranged in the form of a spiral (Nipkow disk) is used to detect the whole surface of the object rather than just one point. Modern instruments use a micro-lens disk instead of or in combination with pinhole apertures. This increases the light yield, thus also enabling poorly reflecting or even transparent objects to be displayed. For 3D scanning, the distance of the lens from the object is adjusted in tiny increments, thus building up a spatial image from the sharply displayed planes [40].

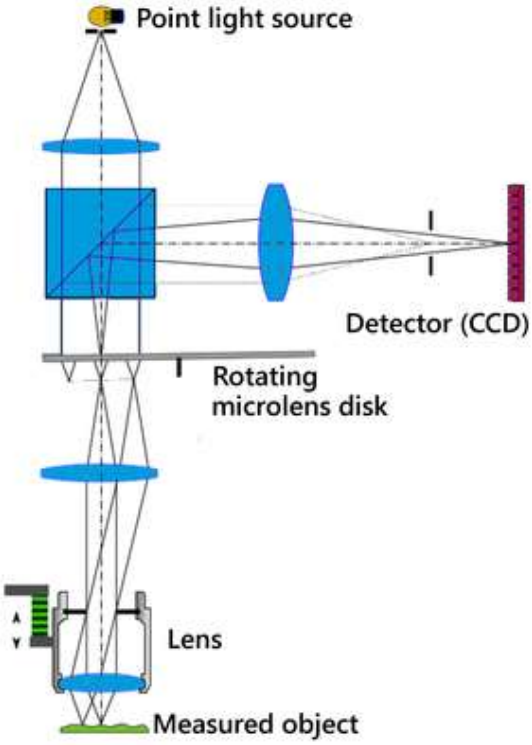

Figure 25 Working principle of confocal microscopic technique [40].

4 Results

Annealing

The enrichment of alloying elements on the surface of the steel substrate during annealing and their oxidation described in Chapter 1, was evaluated by performing GDOES depth profilometry on samples treated at dew point temperatures of -30, 0 and 10 °C in an HNx (5 % H_2; 95 % N_2) atmosphere. The results of the following are presented below on the basis of alloying elemental weight percentage.

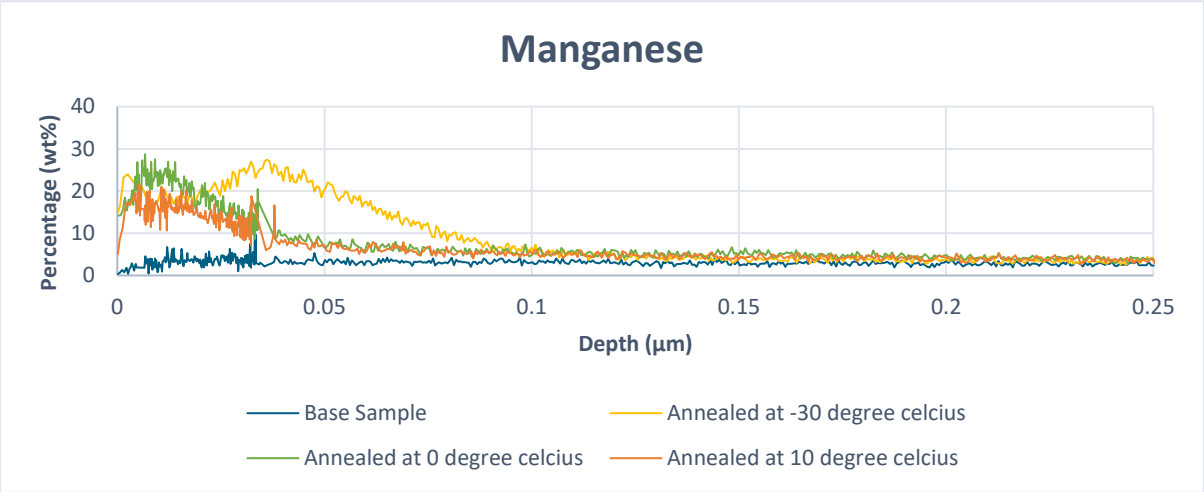

(i)

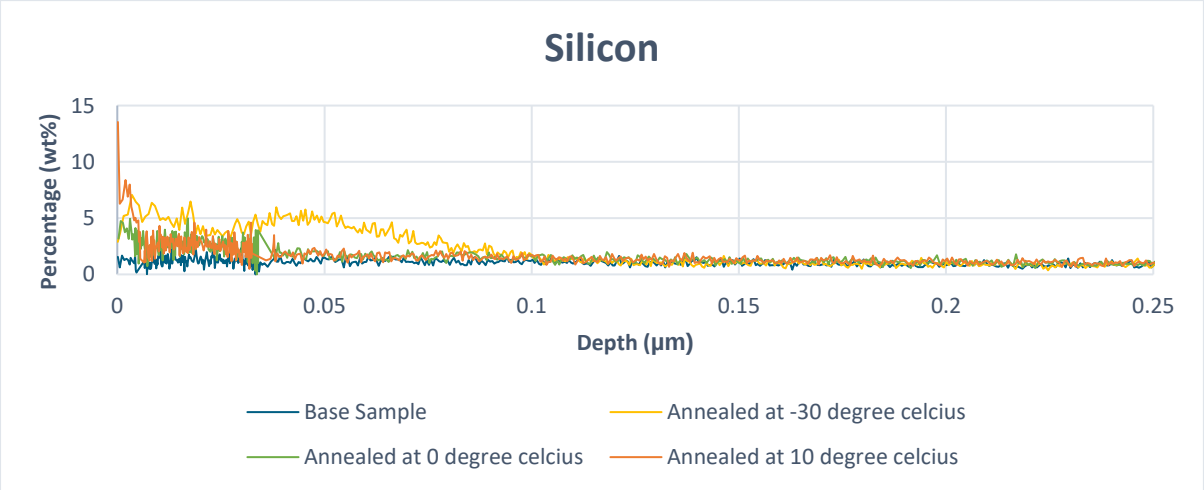

(ii)

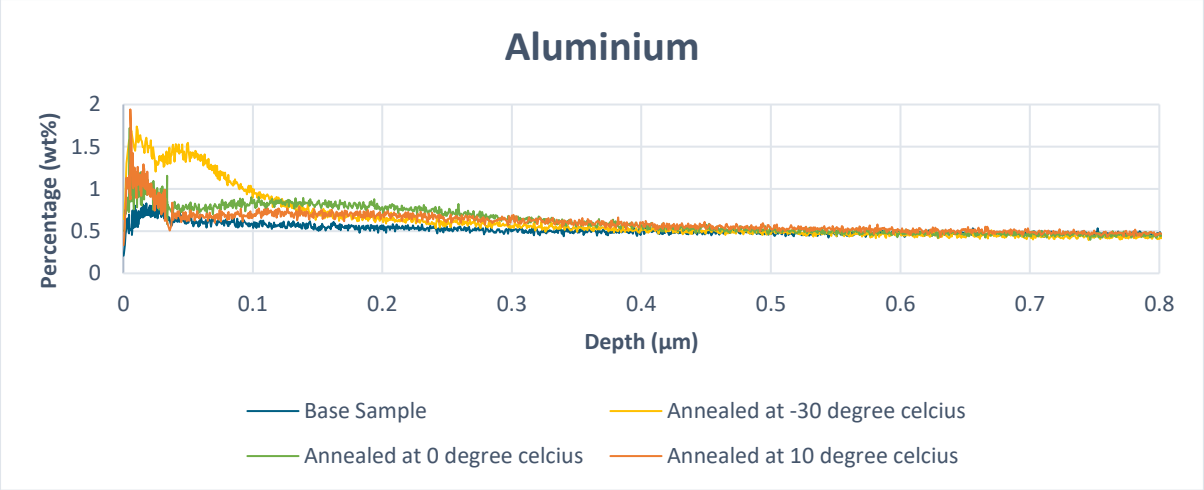
Aluminium
Percentage (wt%)
2
1.5
1
0.5
0
0
0.1
0.2
0.3
0.4
0.5
0.6
0.7
0.8
Depth (µm)
Base Sample
Annealed at -30 degree celcius
Annealed at 0 degree celcius
Annealed at 10 degree celcius

(iii)

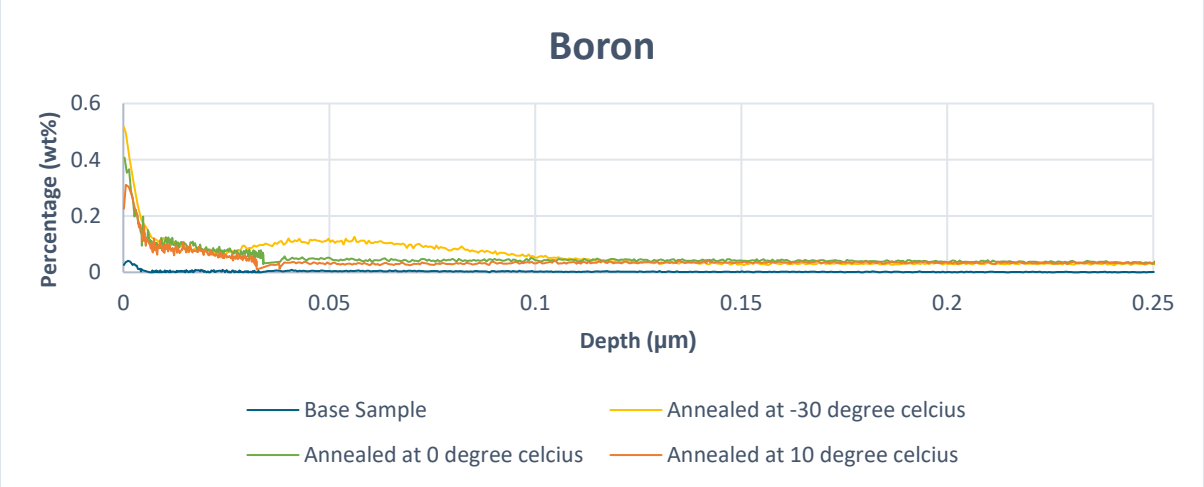
Boron
Percentage (wt%)
0.6
0.4
0.2
0
0
0.05
0.1
0.15
0.2
0.25
Depth (µm)
Base Sample
Annealed at -30 degree celcius
Annealed at 0 degree celcius
Annealed at 10 degree celcius

(iv)

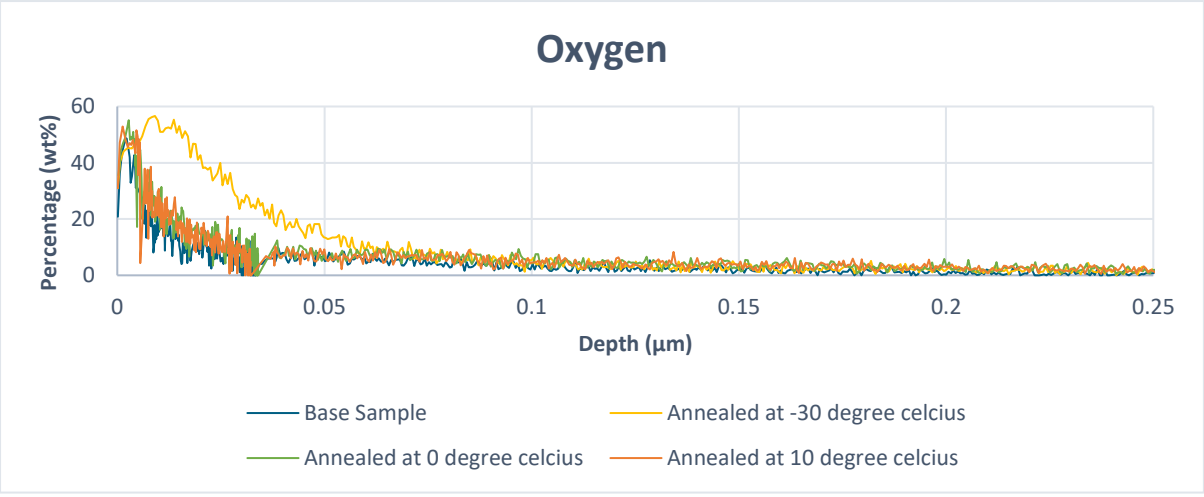
Oxygen
Percentage (wt%)
60
40
20
0
0
0.05
0.1
0.15
0.2
0.25
Depth (µm)
Base Sample
Annealed at -30 degree celcius
Annealed at 0 degree celcius
Annealed at 10 degree celcius

(v)

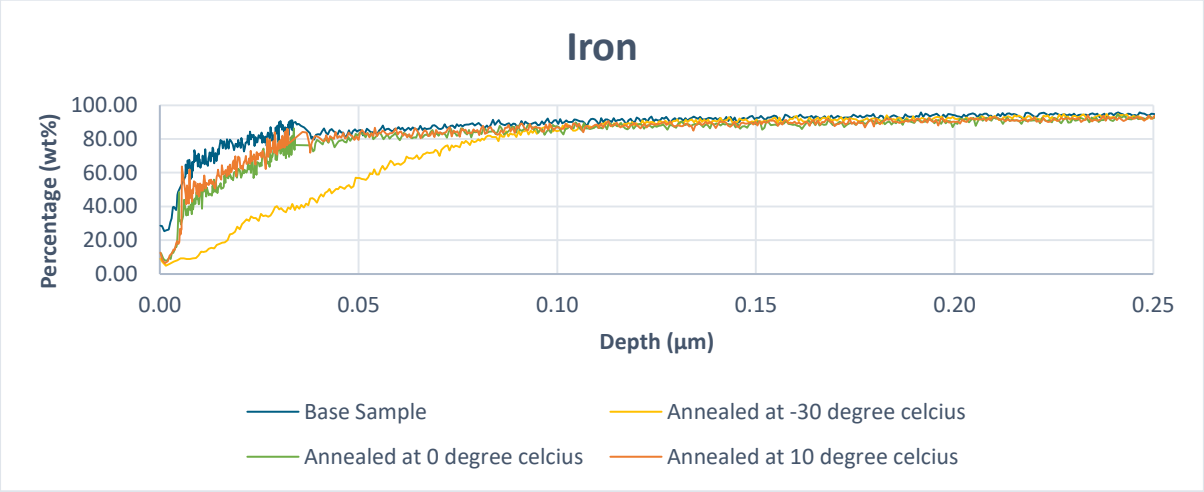

(vi)

Figure 26 GDOES depth profilometry of (i) Manganese, (ii) Silicon, (iii) Aluminium, (iv) Boron, (v) Oxygen, and, (vi) Iron in samples annealed at different dew point temperatures.

As it is clearly visible from the above placed graphs that during annealing, irrespective of the annealing conditions, alloying elements namely Mn, Si, Al and B segregate to the surface to form external oxides or, possibly, nitrides in the case of Boron [41], Figure 26 (i) – (iv). Hence, annealing of DP800 steel is not sufficient to remove oxides from the surface. It needs a pre-cleaning step to improve the surface for subsequent coating.

Hot Dip Galvanisation

After confirming the selective oxidation of alloying elements on the steel surface, the effect of dew point temperature on the coatability of the steel substrate is assessed by coating a few samples using the HDG process after varying the dew point temperatures in the RTF sub-process during annealing between -30, 0 and 10 °C. These different annealing conditions resulted in visible variations when analysing them macroscopically after coating with Zinc; see Figure 27. At -30 °C dew point, the steel surface was covered with a dull coating, marked by the blue box in Figure 27 (i). Generally, as the dew point increased, the coating on the steel surface improved and there was reduction in the size of the bare spots occurring; see Figure 27.

(i) (ii) (iii)

Figure 27 Samples previously annealed at dewpoints of (i) -30 °C, (ii) 0 °C, and, (iii)10 °C inside the RTF coated using HDG process.

Upon further investigation of the surface using SEM & EDS imaging techniques, an abundance of Mn and Si were confirmed in the bare spots on the steel surface; see Figure 28 and Appendix 1 for more information on the surface properties. As seen in Figure 27 (i), the sample annealed at -30 °C had most of its surface filled with a dull coating which was found to be the brittle and unwanted $FeZn_{13}$ phase. This indicates that the Aluminium was consumed in reducing the oxides of Mn and Si. Therefore, the diffusion layer (Fe_2Al_5) wasn't formed leading to a poor Zinc coating. Instead of the diffusion layer or inhibition layer, $FeZn_{13}$ crystals were formed on the steel surface.

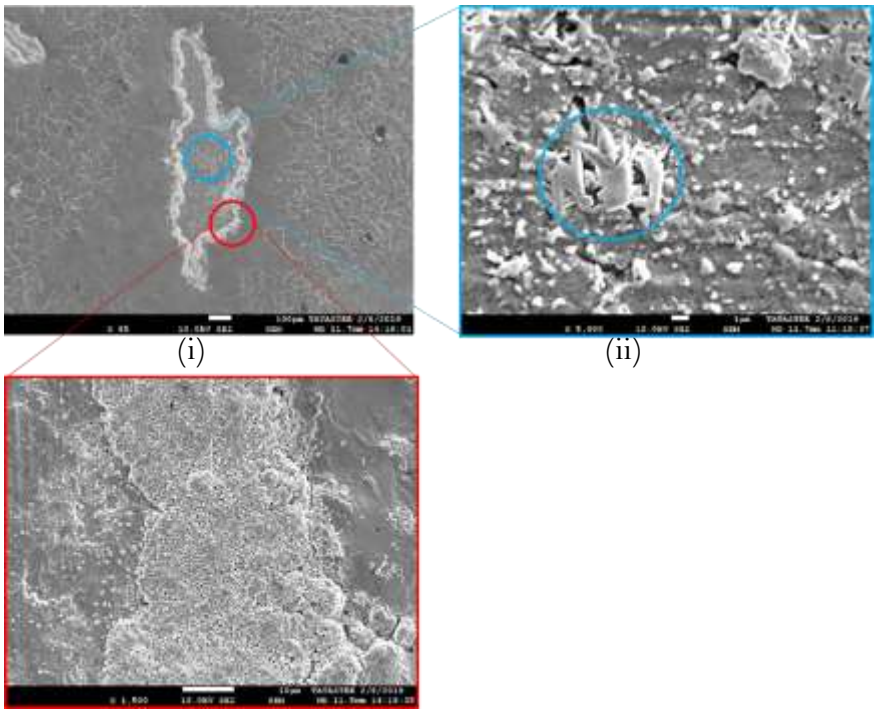

(i) (ii)

(iii)

Figure 28 (i) Bare Spot, (ii) $FeZn_{13}$ crystals, and, (iii) No Fe_2Al_5 diffusion layer present inside the bare spot, abundance of $FeZn_{13}$ crystals on the boundaries and proper Zinc adhesion outside of the bare spot.

Considering the surface enrichment of oxides and evaluating the surface after Zn coating, samples were annealed at dew points of 0 °C in the RTF sub-section during annealing for the EPC process for to avoid complications associated with annealing.

Once the problem of selective oxidation associated with the annealing of DP800 was witnesses at first hand, samples of dimensions 120 × 80 × 1.5 mm^3 were annealed and brought in for EPC treatment. The anode that could clean the steel surface most effectively, retain the wettability of the steel surface and produce the most homogenous surface after treatment needed to be found. The anodes in this study, were being evaluated on the basis of material and geometry. Studying the surface morphology, wettability and topography of the steel after EPC treatment helped decide on the material for the anode. The topographical measurements also help find the right geometry for the anode. The results of these analyses are published below.

Surface Morphology

The local temperatures during the EPC treatment exceed 1500 °C at the interaction site which results in anodic deposition and occurrence of surface re-melting. All the metal anodes used for treating the DP800 resulted in the deposition of the anode material onto the steel substrate. The formation of nodules and craters are a sign of the surface re-melting and immediate cooling phenomenon. The following pages of the report include SEM images of the treated samples as a function of changing anode material.

Steel Anode

A steel anode was used because the substrate being cleaned was steel. When using a steel anode, droplet of steel ≈10 μm in diameter are deposited on the sample surface after treatment; refer Figure 29 and Appendix 2.

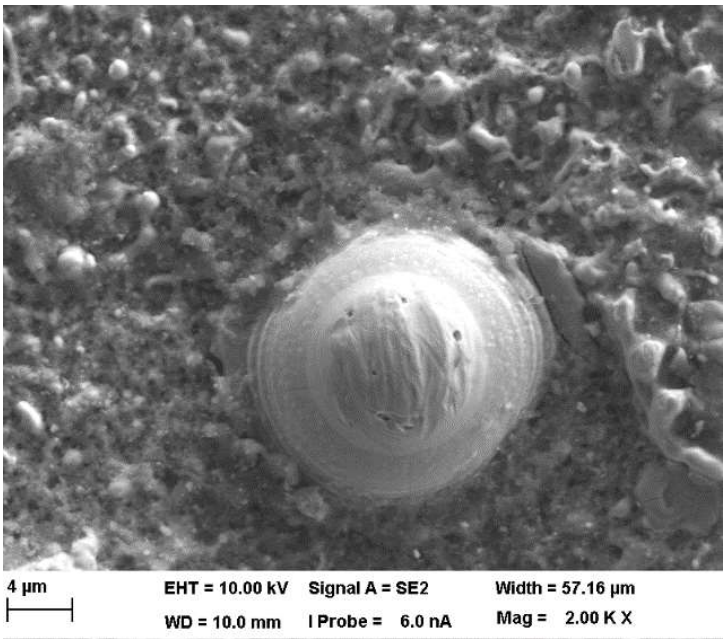

Figure 29 Droplet from a steel anode on the DP800 substrate (Appendix 2).

Titanium Anode

For the Titanium anode, a porous 3D printed prototype was use. It was used as a test anode because Titanium has a high melting temperature (1668 °C) and the porosity brought about by the 3D printing was thought to be sufficient to cool the anode and prevent its melting. Porous materials, in general, have higher power density and are researched extensively in the context of energy storage [42] [43]. Metal foams with small pores and thin cell walls have been found to have very high electrical resistivity [44]. This led to insurmountable amounts of melting at the anode, previously unencountered; see Figure 12. A porous anode was thus unsuitable for our applications. Nevertheless, Titanium deposits of $\approx 200\ \mu m$ were found in samples treated with a 3D printed titanium anode; see Figure 30 and Appendix 3.

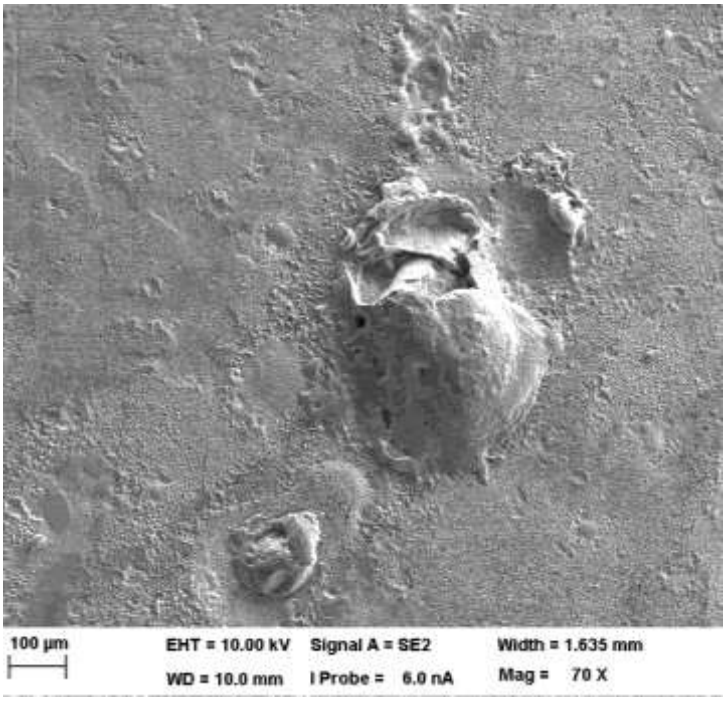

Figure 30 Titanium droplet on a DP800 steel substrate (Appendix 3).

Stainless-Steel Anode

A ferritic Stainless-Steel anode was used which has a high Chromium and low carbon content. Overall there was an increase in the Chromium content on the surface of the DP800 steel. A high percentage of Carbon was present at the corrugated blackened region that runs across Figure 31. The significant rise in Chromium and Carbon content is a direct consequence of the dissolution of Carbides present in the Heat Affected Zone (HAZ) of the Stainless-Steel anode on heating. During welding of Stainless-Steel, these Carbides transform preferentially into Chromium Carbides due to the immediate cooling provided by the electrolyte during the cleaning action. These newly formed Chromium Carbides precipitate on the grain boundaries, depleting Chromium from the region immediately adjacent to the boundary, resulting in a local loss of chromium and a reduction in corrosion resistance. If sufficient chromium carbides are formed this results in a network of steel along the grain boundaries sensitive to corrosion, or in other words, the steel has been sensitised. This sensitisation occurs in the HAZ region that has seen temperatures between 600 and 900 °C and times that may be as short as 50 seconds. Since Titanium deposits were observed on the steel surface from a Titanium anode in the previous

section, the temperatures needed for sensitisation phenomenon to occur at the Stainless-Steel anode could be achieved. This combined with the high electric field results in the possible deposition of Chromium Carbides on the DP800 steel surface.

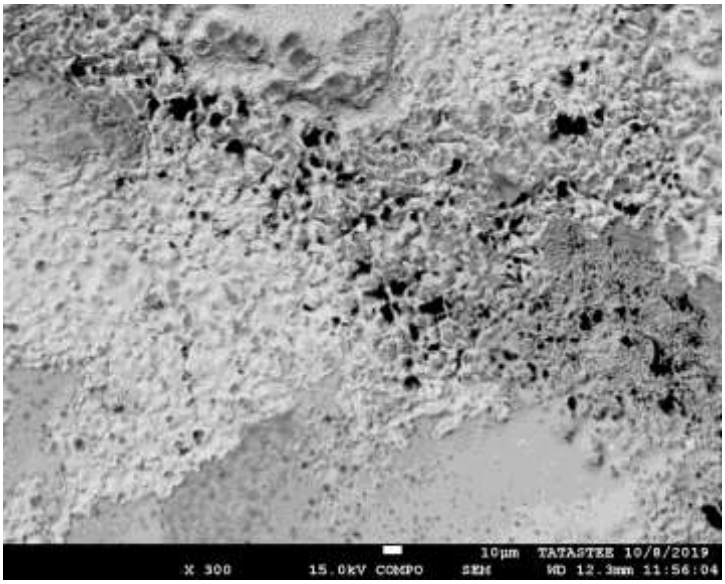

Figure 31 Sample after treatment with Stainless-Steel anode (Appendix 4).

Copper Anode

Copper was selected as a test anode material because it has a high conductivity which was initially believed to positively influence the generation of plasma, for instance, by bringing down the breakdown voltage. Copper also had the lowest melting temperature out of all the anode materials used. Therefore, Copper and Copper oxide deposition was expected. Figure 32 shows the presence of particles rich in Copper and Oxygen on the samples that were treated with a Copper anode. Sodium is also found in the form of thorn-like structures on the steel surface. These thorn-like structures did contain Copper and Oxygen as well; see Appendix 5. Such structures were not found in samples treated with any other metal.

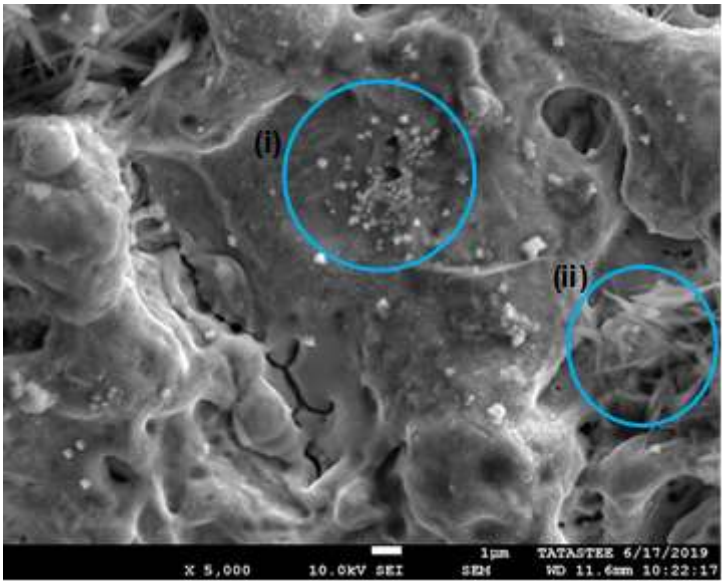

Figure 32 (i) Possible Copper Oxide particles (Appendix 5, Figure 57), and, (ii) Thorn-like structures with Na (Appendix 5, Figure 58) on a DP800 sample treated with a Copper anode.

Graphite Anode

It became apparent through the course of the experiments that any metallic anode is bound to melt and either deposit itself or its oxides onto the treated steel surface. Thus, Graphite was used as an anode to prevent this unwanted deposition. The Graphite anode provided the most promising results in terms of wettability (Figure 34), surface roughness (Table 8) and surface morphology; refer Figure 33.

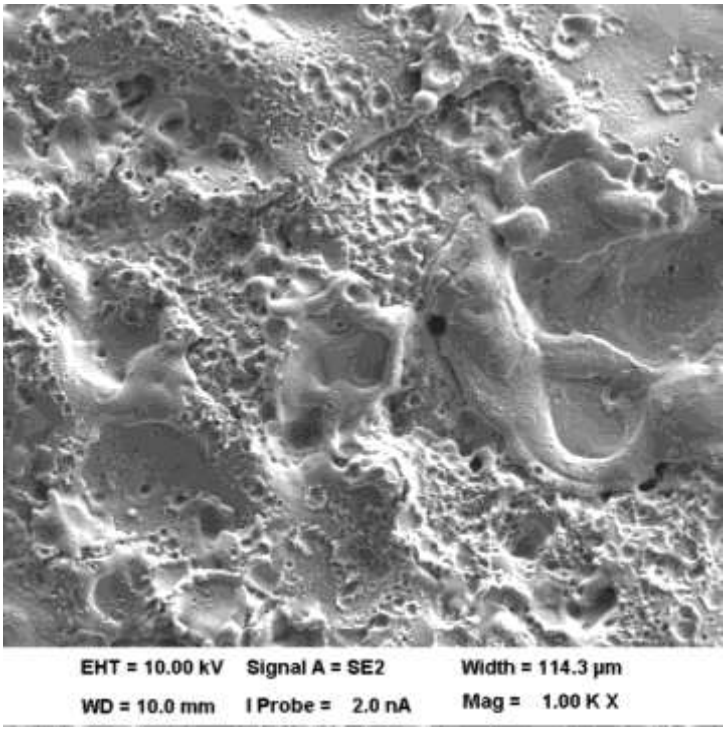

Figure 33 A DP800 sample treated with a Graphite Anode (Appendix 6).

The Graphite used in this project was procured from Toyo Tanso USA Inc. It is a special grade graphite which has ultra-heat resistance, excellent electrical conductivity and chemical resistance; refer Table 7.

Grade	Bulk Density	Hardness	Electrical Resistivity	Flexural Strength	Compressive Strength	Tensile Strength	Young's Modulus	Coefficient of Thermal Expansion	Thermal Conductivity
	Mg/m^3	HSD	$\mu\Omega \cdot m$	MPa	MPa	MPa	GPa	$10^{-6}/K$	$W/(m \cdot K)$
ISO-68	1.82	80	15.5	76	172	54	13.2	5.6	70

Table 7 Important properties of Graphite used [45].

Surface Wettability

Sessile droplet experiments were performed on treated samples to investigate the changes in the surface wettability of the steel substrate. Surface wettability measurements help to indicate the adhesion performance of the given surface. This is performed on samples treated with different types of anode materials. Both treated and untreated samples were analysed using demineralised water for the sessile drop experiment. There was an increase in the

contact angle for the samples treated with Copper, Steel and Stainless-Steel anodes while a reduction of contact angle only in the case of the Graphite anode; see Figure 34.

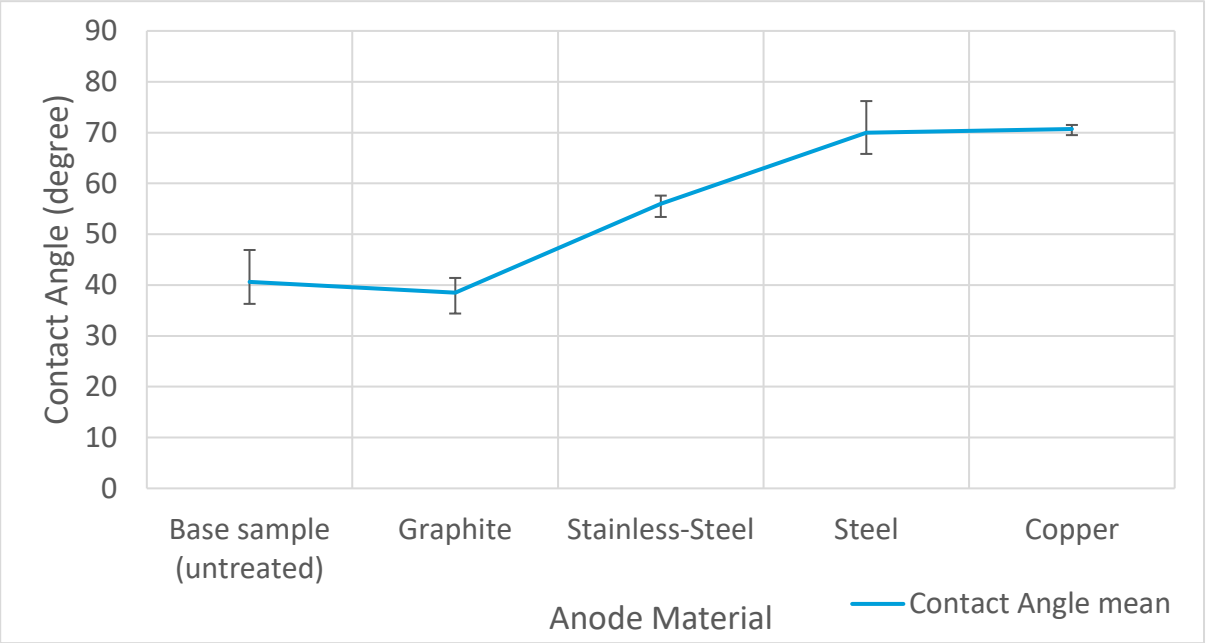

Figure 34 Contact angle measurements for EPC treated and untreated samples using anodes made out of different materials.

Surface Topography

Surface topographical measurements were performed to understand the effect of anode material, geometry and treatment time. A 3 to 4-fold increase in the average surface roughness, R_a, of Stainless-Steel sample was observed after the EPP treatment [23]. When stylus profilometry was performed after EPC treatment on DP800 samples, the anodes with the same geometry performed identically with no noticeable change in surface roughness. Even the redeposited anode material in the case of the Stainless-Steel and Copper anode did not play a significant role in changing the surface roughness; see Table 8. These measurements also show that a solid graphite anode performs better than its perforated counterpart and other metallic anodes. The average surface roughness deteriorates with increasing treatment time.

Anode Material	Untreated Sample	Steel	Stainless-Steel	Copper	Graphite		
Geometry		h = 20 mm Ø = 20 mm No. of holes =4 ($Ø_h$ = 4 mm)	h = 20 mm Ø = 20 mm No. of holes = 37 ($Ø_h$ = 1 mm)	h = 20 mm Ø = 20 mm No. of holes = 37 ($Ø_h$ = 1 mm)	h = 20 mm Ø = 20 mm No. of holes = 37 ($Ø_h$ = 1 mm)	h = 20mm $Ø_1$ = 20mm $Ø_2$ = 16mm	h = 20mm $Ø_1$ = 20mm $Ø_2$ = 16mm
Treatment time (sec)		20	20	20	20	20	30
R_a (μm)	1.3	1.5	1.3	1.3	1.3	1.1	1.9

Table 8 Surface Roughness of treated sample as a function of anode material and geometry.

To gain more information on the effect of treatment time and inter-electrode gap on the surface roughness of the steel substrate, confocal microscopy was performed on samples treated with a solid graphite anode; see Figure 35. Since deposition of anode material is undesirable, samples treated with other anode materials were not considered. It was found that the R_a of the treated regions increased with increasing treatment time and inter-electrode distance. More information on the results obtained can be found in Appendix 7.

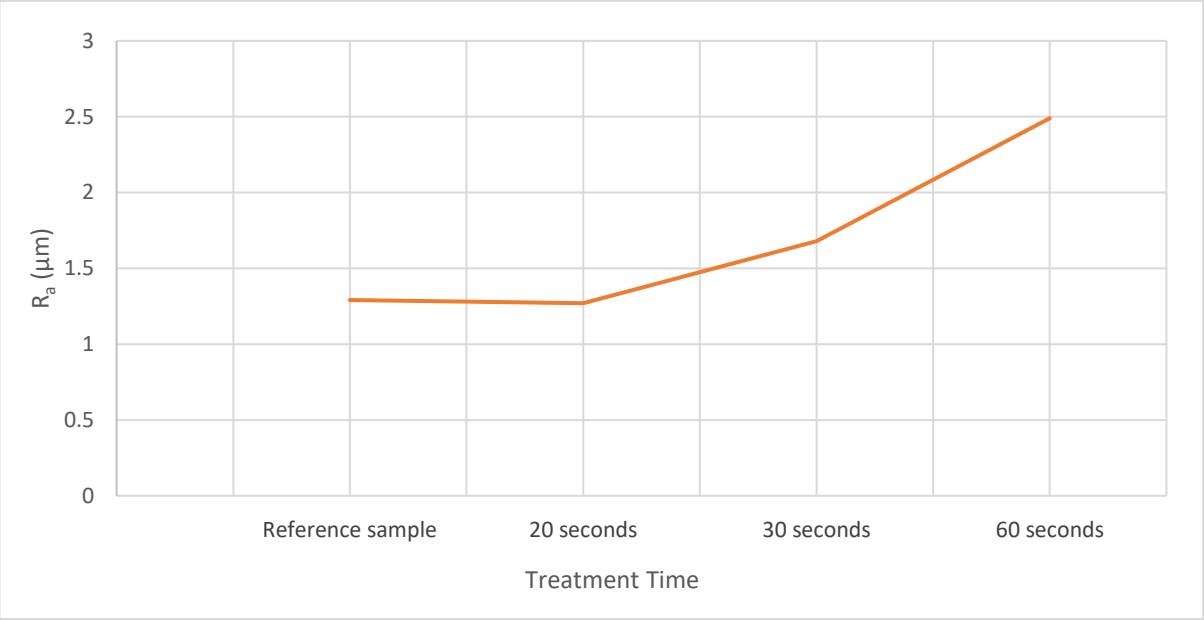

(i)

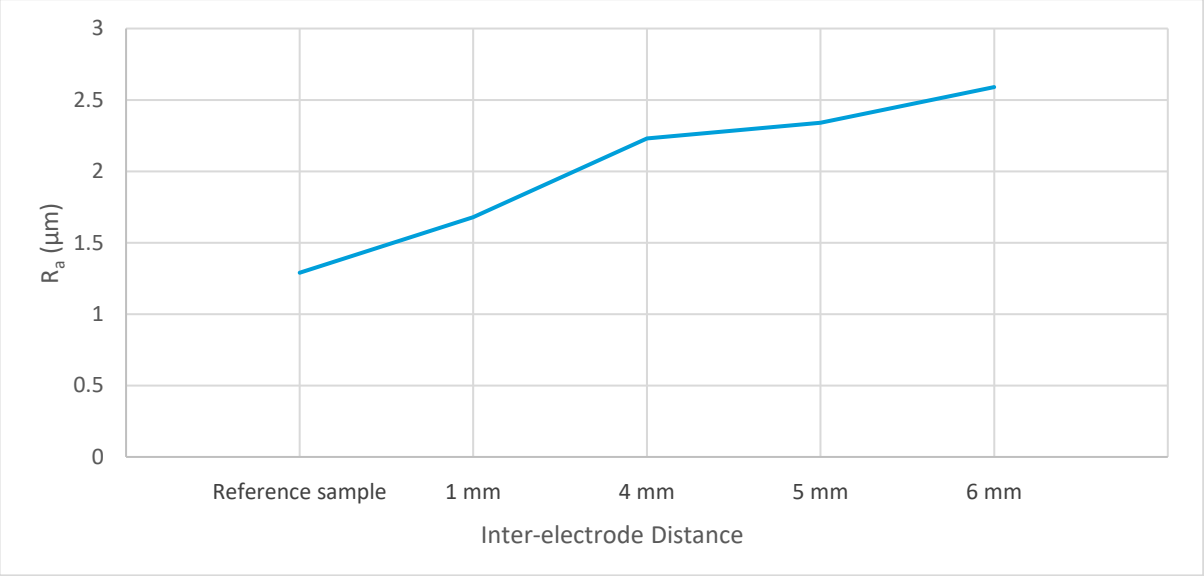

(ii)

Figure 35 Surface Roughness as a function of (i) Treatment Time, and, (ii) Inter-electrode Distance.

Cross-sectional SEM was performed on treated and untreated samples to get more insight on the spheroids and craters; see Figure 36. The samples were treated for 60 seconds and with an inter-electrode distance of 1 mm.

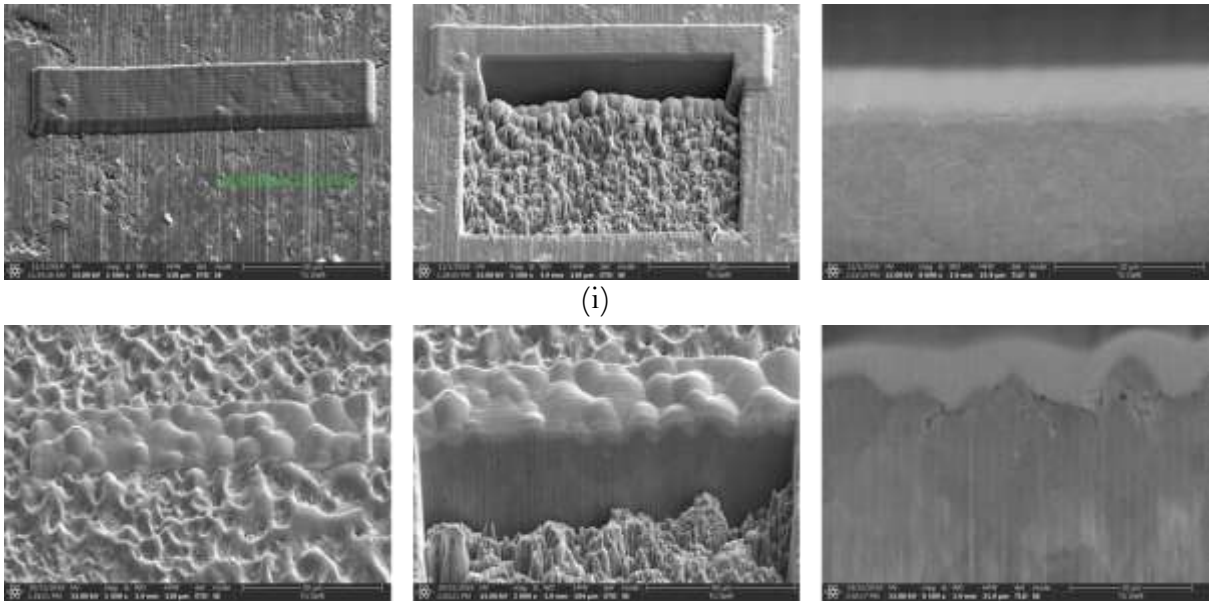

Figure 36 Cross-Sectional SEM of (i) untreated DP800 sample, and, (ii) treated DP800 sample.

The nodules and craters on the treated sample change the elevation considerably on the micrometres scale. On a closer look; see Figure 37, it is found that the wave height is ≅ 3 μm and the wave length is ≅ 4 μm which is comparable to the roughness difference measured using confocal microscopy. The size of these defects is likely to decrease as the treatment time decreases from 60 seconds.

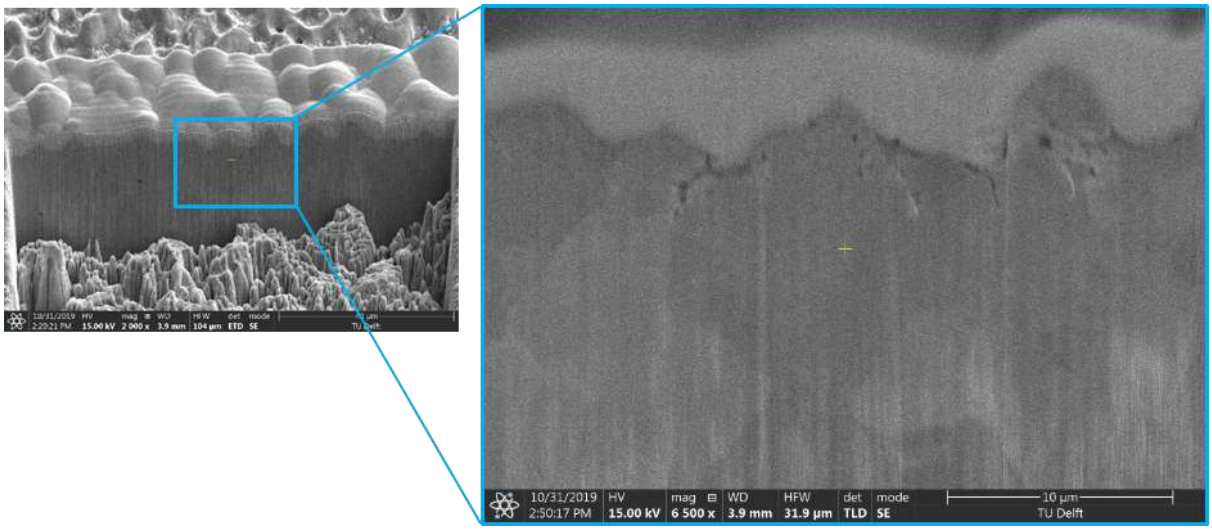

Figure 37 Sideview of nodules and craters on an EPC treated DP800 sample.

Chemical Analysis

Samples annealed at 0 °C were treated with a Copper anode (sample name T1, T2 and T3) and a Graphite anode (sample name T4, T5 and T6). When GDOES depth profilometry was performed on samples T1, T2 and T3, significant amounts of Copper and Oxygen were found on the samples owing to the treatment being performed with a Copper anode compared to samples T4, T5 and T6 which were treated with the graphite anode; see Figure 38 and Figure 39. The Oxygen weight percentage of the samples treated with the Graphite anode reduced.

This reduction isn't as much as was estimated based on the SEM and EDS analysis of the same surfaces. GDOES also detected the presence of Sodium on the samples; more weight percentage of Sodium was found in the samples treated with a Copper anode; refer Figure 40, confirming the thorn-like occurrences made out of Sodium, Copper and Oxygen seen in Figure 32 (ii). Deposits of Copper were also found on the samples treated with the Graphite anode but the weight percentage of Copper found was very less (~ 2 to 6 % on the surface) as compared to the ones treated with the Copper anode (~ 30 to 70 % on the surface); refer Figure 38. The presence of Copper provides micro-galvanic sites on the steel surface for the Copper to oxidise and form a greenish patina on the samples treated with the Copper anode; see Figure 41. Similar Copper deposits were detected by GDOES when treated with other anode materials; refer Appendix 8. These depositions could be linked to the electrical contact between the anode and the power supply which is provided through a copper rod (Figure 17-7). This rod melts due to the high heat generated during the plasma.

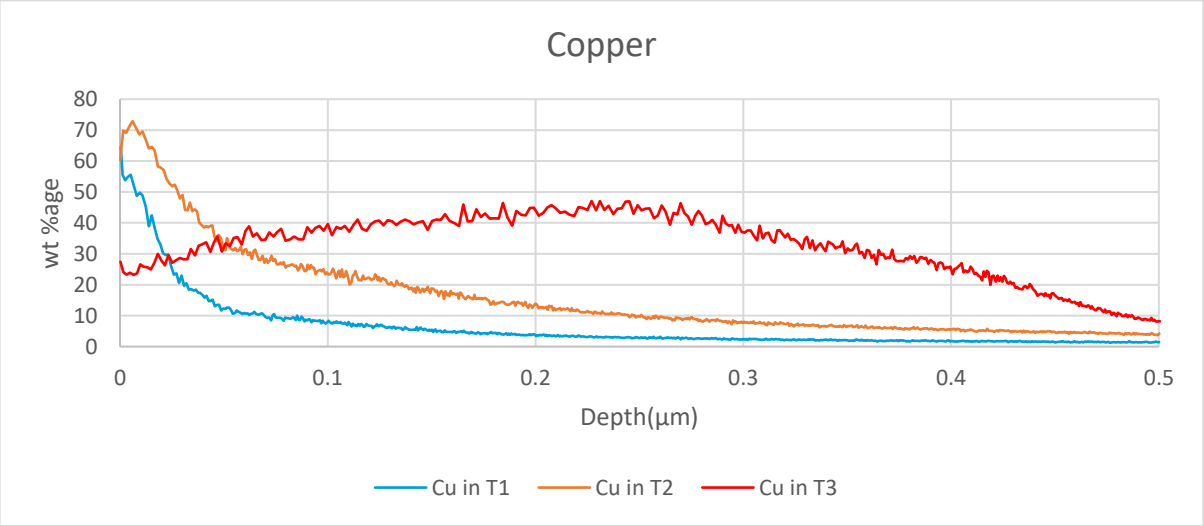

(i)

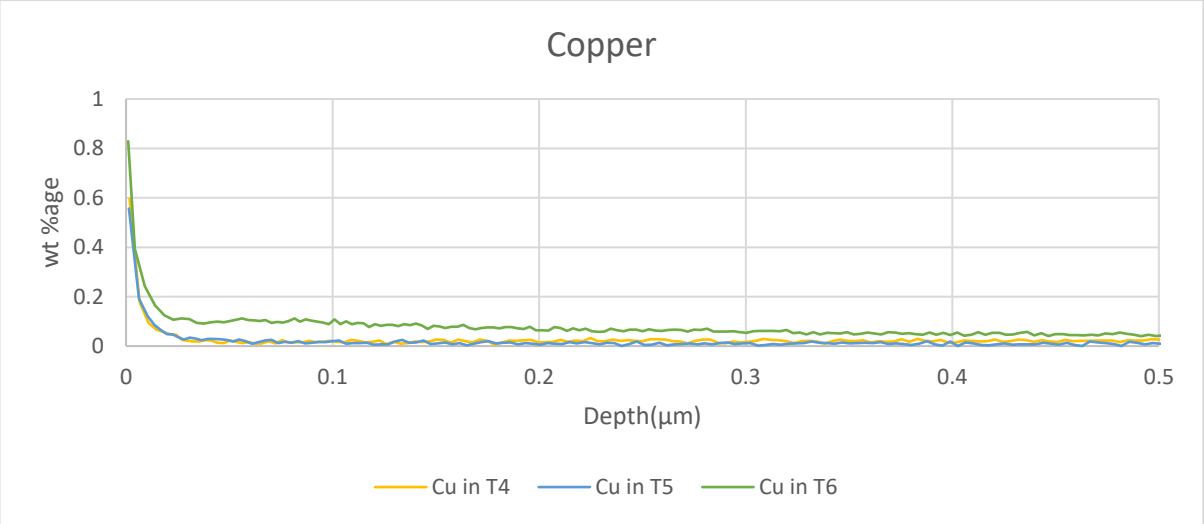

(ii)

Figure 38 GDOES depth profilometry to detect Copper in samples treated with a (i) Copper anode, and, (ii) Graphite anode.

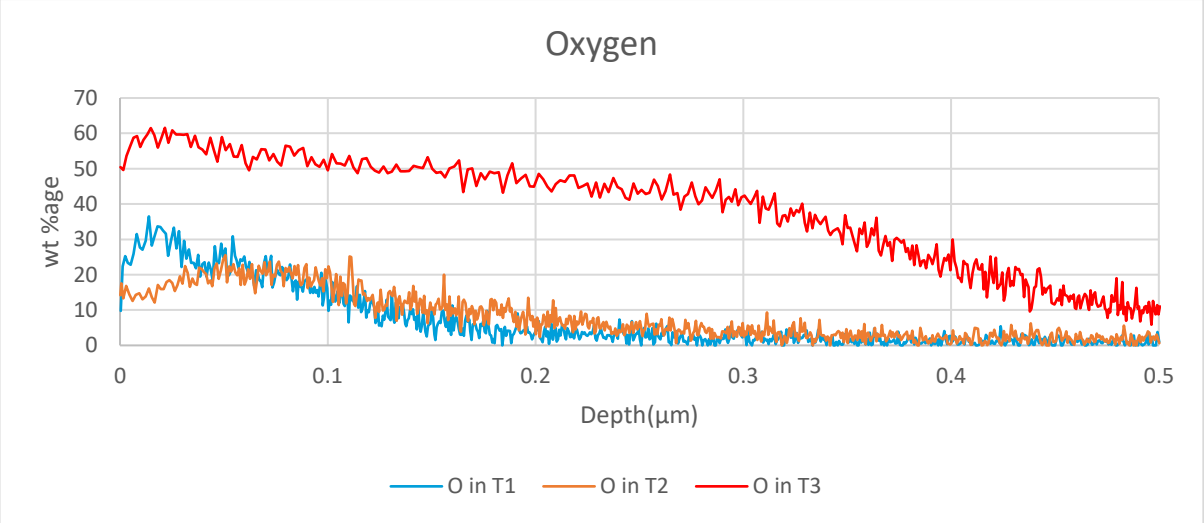

(i)

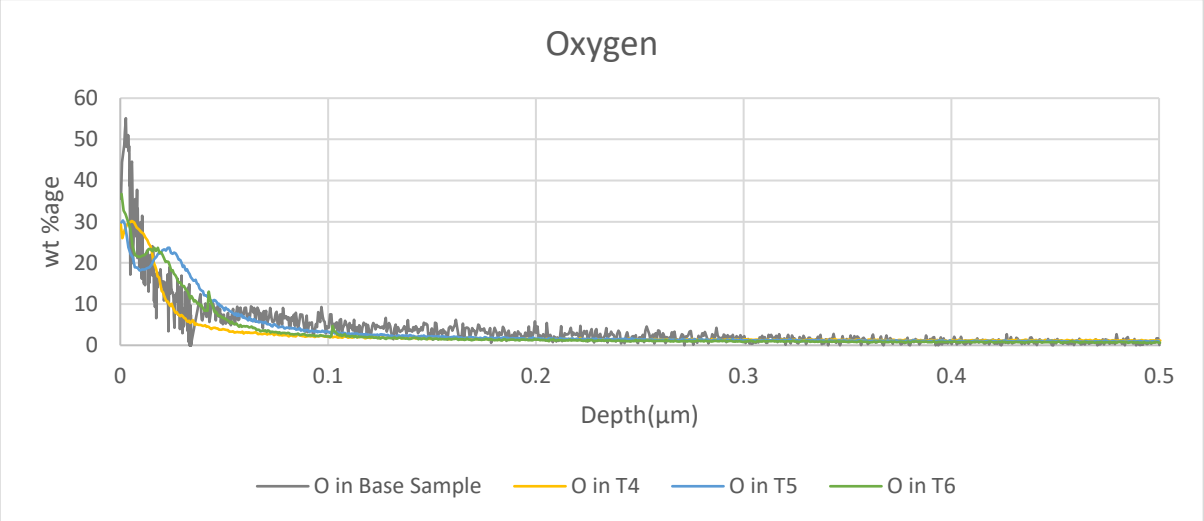

(ii)

Figure 39 GDOES depth profilometry to detect Oxygen in samples treated with a (i) Copper anode, and, (ii) Graphite anode.

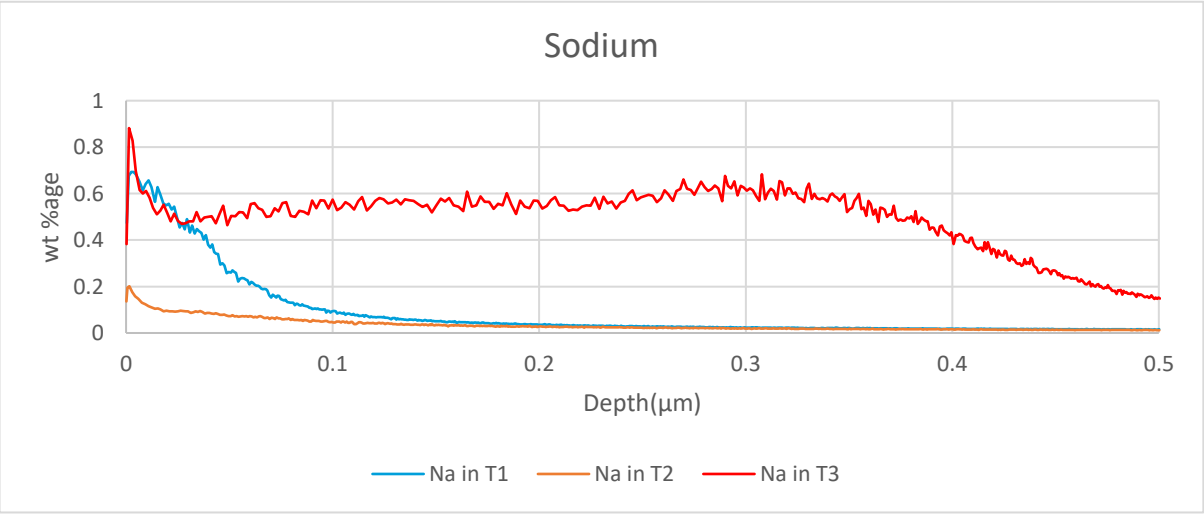

(i)

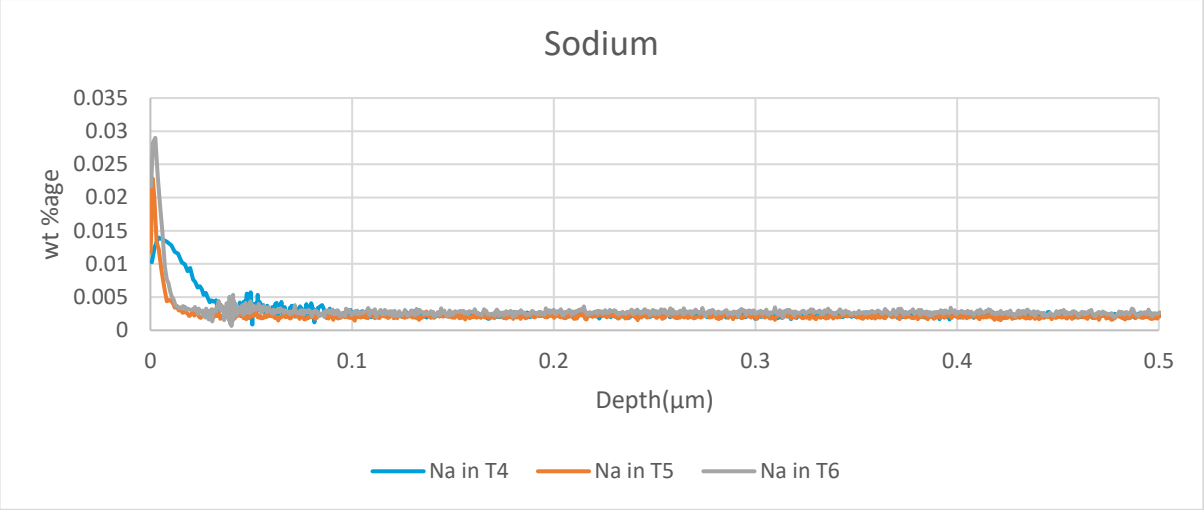

(ii)

Figure 41 GDOES depth profilometry to detect Sodium in samples treated with a (i) Copper anode, and, (ii) Graphite anode.

Figure 40 Greenish patina on the sample treated with a Copper anode.

Plasma Analysis

Parameters, namely, concentration of salt, temperature of electrolyte, material of the anode, inter-electrode distance and flow rate have an influence on the plasma generation. Temperature has been excluded from this analysis because of the inability to control it within the setup used. Furthermore, as metallic anodes deposited unwanted anode material on the steel substate, Graphite was chosen as the material for the anode because of its ability to disintegrate rather than melt. The geometry of the anode taken for the plasma analysis was solid with a single cylindrical duct through it for electrolyte flow. This geometry outperformed others when linear profilometry was performed on treated samples; see Table 8.

Concentration of Electrolyte

Changing the concentration has negligible influence on the generation of plasma. It is seen in Figure 42 that the V_b and the corresponding current value for a $\dot{f}$ = 60 L/hr are almost identical for the 0.0047 M solution and the 0.0283 M solution at approximately 300V to 350V and 7A

while the same could be said for the 0.0094 M and 0.0189 M solution where $V_b \approx 200$ V and $I \approx 11$ A. This offset could be attributed to the reducing anode cross-section or the increasing temperature of the electrolyte which were not measurable.

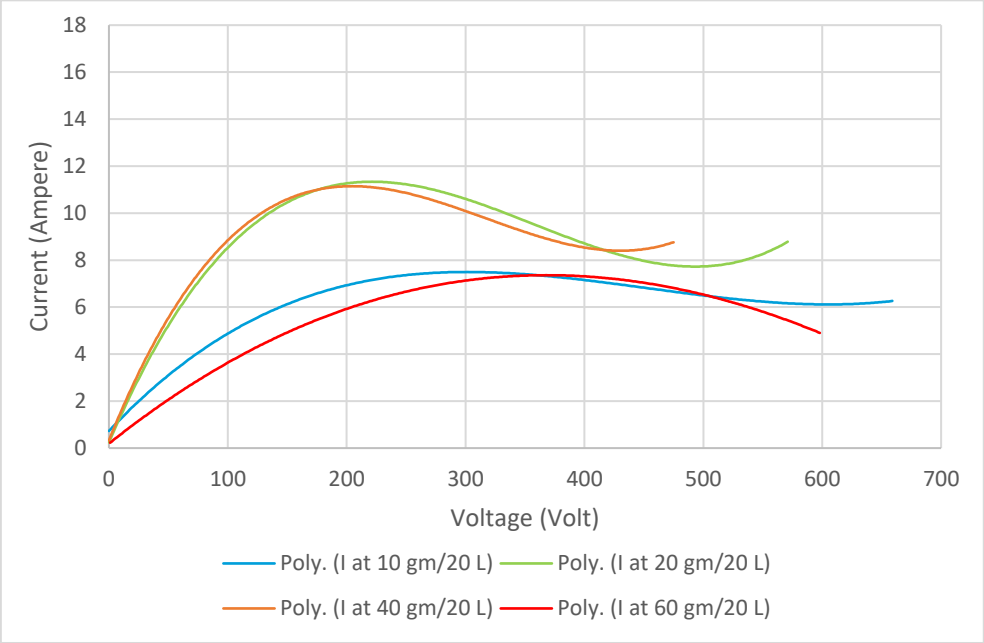

Figure 42 Current v/s Voltage as a function of concentration.

Inter-electrode Distance

Inter-electrode distance between 1 to 2 mm ensured a continuous plasmonic interaction between the two electrodes. As the gap increases, the plasma discharge at the anode is unable to interact with the workpiece due to the reducing electric field and hence the voltage needs to be increase in order to compensate for the increasing gap; see Figure 43.

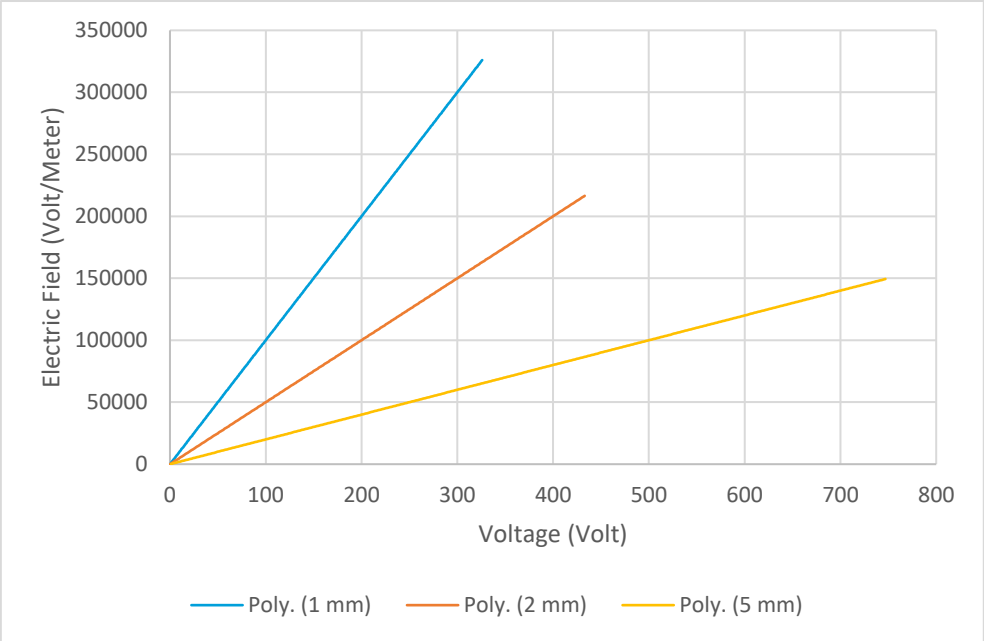

Figure 43 Electric Field v/s Voltage as a function of inter-electrode distance.

The increasing distance increases the resistance of the system and lowers and current passing through the electrolyte; refer Figure 44. More energy is needed to start vaporisation which is reflected by the increasing breakdown voltage as the height increases.

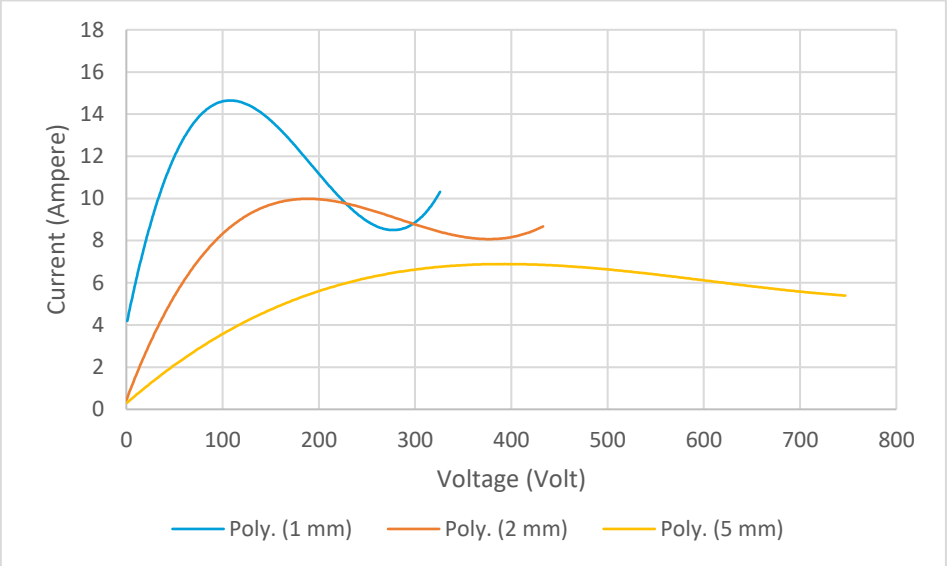

Figure 44 Current v/s Voltage as a function of inter-electrode gap.

Flow Rate

It was observed that at $\dot{f} = 160$ L/hr it was difficult to produce a continuous plasma and at $\dot{f} = 200$ L/hr there was no plasma formation even at 5 kW of input power. See Figure 45 for the V-I characteristics for a concentration of 0.0189 M. For 200 L/hr, the V-I curve is not even in Kellogg region because there was no more input power available to supply. This is attributed to the higher turbulence caused by the flow leading to increased heat dissipation and decreased Hydrogen and bubble formation on the workpiece. Therefore, lower $\dot{f}$ of 60 to 80 L/hr are preferred. [37] suggested that flow rates between 120 to 360 L/hr could produce a plasma, these flow rate values were quite high for the setup used in this investigation.

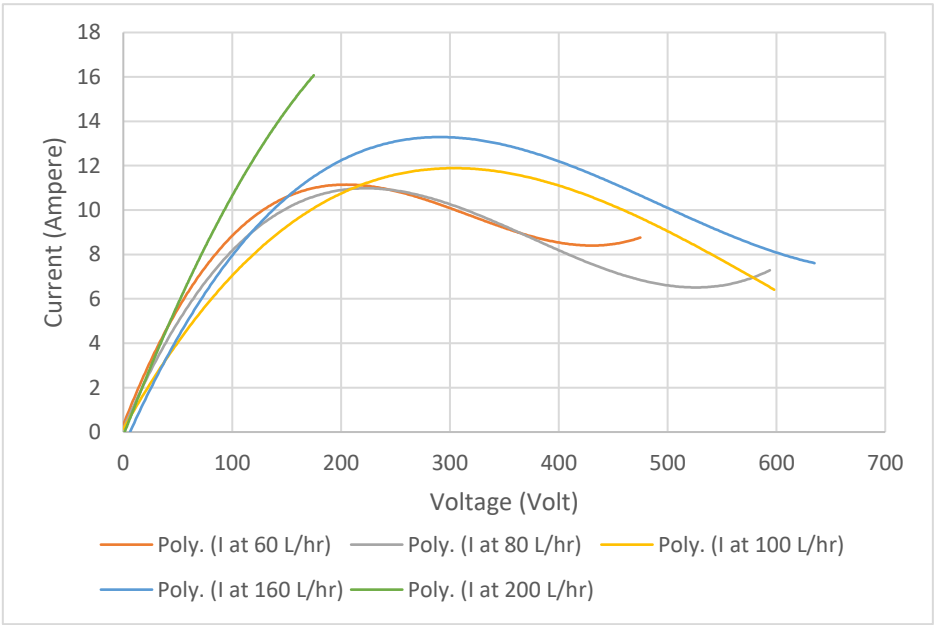

Figure 45 Current v/s Voltage as a function of flow rate.

5 Discussions

1. ***Anode Material:*** Using metallic anodes led to anode melting and deposition of anodic oxide on the substrate. Sodium deposits were also detected due to the electrolyte used. This led to an increase in the contact angle thus reducing the wettability of the treated samples. However, with a graphite anode, such depositions were brought down to a minimum and the contact angle for a graphite treated sample was, in fact, found to be lower as compared to other anode materials.

   The current and resistance for Stainless-Steel, Graphite and porous Titanium anodes were compared under increasing input power to gain insight about the degradation process; see Figure 46.

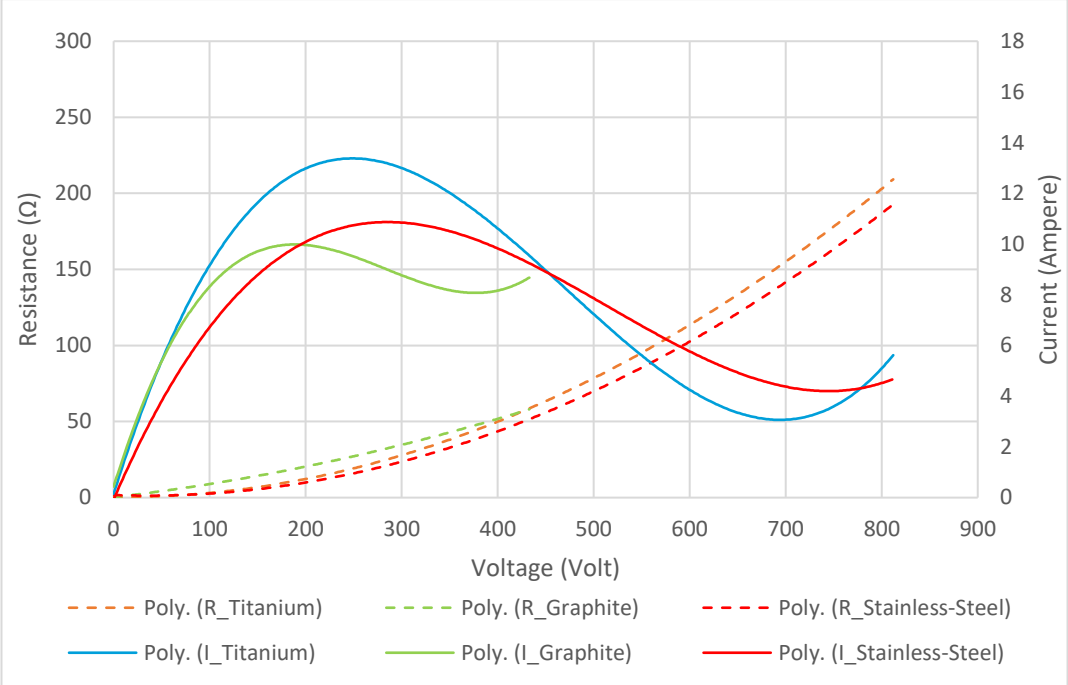

Figure 46 Current and Resistance v/s Voltage as a function of changing anode material.

Graphite has the highest electrical resistivity (15.5 μΩ·m), followed by the ferritic Stainless-Steel (~ 1.5 μΩ·m) and Titanium (~ 0.67 μΩ·m). The increase in peak current from ~ 10 A to 13 A as a function of changing electrode material, suggest this decrease in electrical resistivity from Graphite to Titanium. The Kellogg region started at a V_B ~ 180 V for the graphite anode and within the 200 to 300 V range for the Stainless-Steel and Titanium anode. The Kellogg region for the graphite anode was the least, between ~ 180 and 380 Volts, amongst the materials evaluated above. The Kellogg regions for the other anodes were ~ 2.5 times that of the graphite anode. However, the power requirements to form a continuous plasma for graphite at ~ 1800 W when compared to the metals. Therefore, the implication is that while using a graphite anode can generate a plasma at a lower input power of ~ 1800 W but it needs better supervision and controllability as the operation window is small.

2. ***Anode Geometry & Surface Roughness:*** Surface Roughness of the steel substrate was affected by the anode geometry and minimum or negligible effect was seen as a result of changing the anode material. At first, it was thought that having more holes on the anode is beneficial for a more homogenous steel surface. However, it was observed that the area around the holes were preferentially attacked and became prone to erosion. This phenomenon was prominent in case of a graphite anode (Figure 13) as the metallic anodes were more susceptible to corrosion than erosion. Hence, a graphite anode was fabricated where the flow of electrolyte was through a single cylindrical duct located in the centre of the anode rather than through a cluster of smaller holes. Nonetheless, the disintegration of the anode continued to take place at the edges of this cylindrical duct; refer Figure 47.

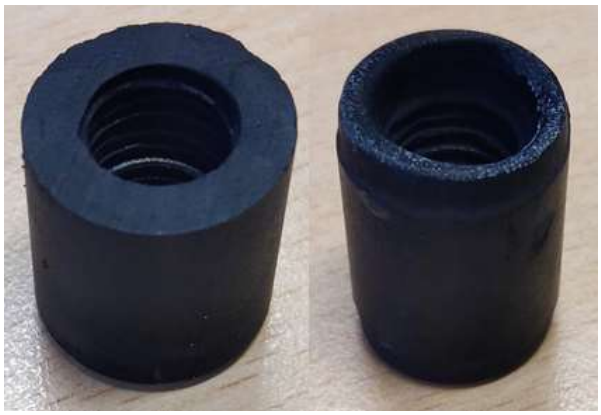

(i) (ii)

Figure 47 Graphite anode with cylindrical duct through it for electrolyte transport (i) used, and, (ii) unused.

Having solid carbon material around the cylindrical duct of the graphite anode provided a continuous area for plasma interaction giving a shiny homogenous surface which was not possible to achieve when the graphite anode had perforations resulting in a dotted pattern on the surface; refer Figure 48.

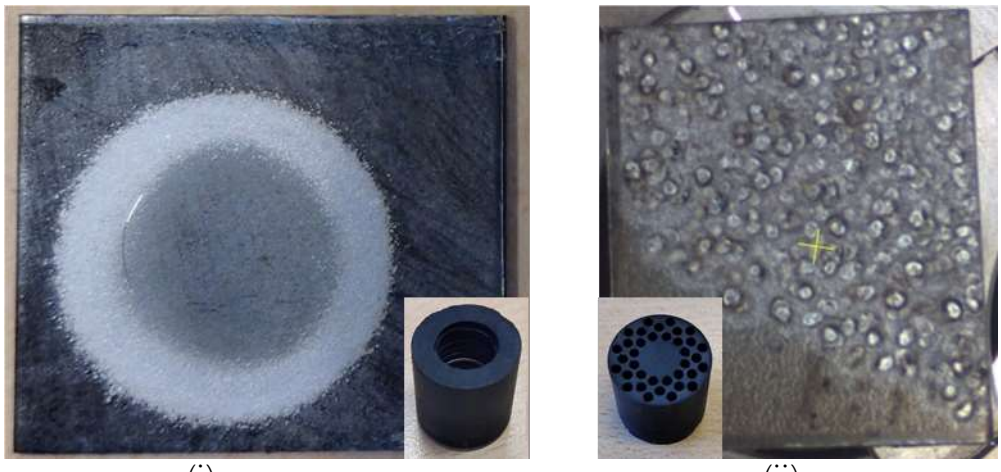

(i) (ii)

Figure 48 Sample treated with (i) a solid graphite anode comprising of a cylindrical duct through it, and, (ii) a graphite anode with 37 holes.

3. ***Influence of treatment time & inter-electrode distance on surface roughness:*** The surface roughness of the steel surface increases with the increasing treatment time and inter-electrode gap.
   - More treatment time implies more surface melting and solidification which will increase the number of craters and nodules as well as increase the size of the craters.
   - Increasing inter-electrode gap increases the amount of water needed to be vaporised as well as reduces the electric field. Thus, more power is needed to vaporise the water and to achieve the V_B. Figure 35 (ii) shows the deterioration of the surface (increasing R_a) with increasing inter-electrode distance and Figure 44 shows the increasing V_B as a result of widening inter-electrode gap.

     A plausible correlation can be drawn between the weld penetration in an Arc Welding process and the size of the craters formed during EPC treatment. The inter-electrode distance is analogous to arc length in welding. During Arc Welding, keeping the same wire feed rate, as voltage increases, the arc length gets longer and as voltage decreases, the arc length gets shorter. The length of the arc determines the width and size of the arc cone. As arc length decreases, the arc cone becomes narrower and the arc is more focused; see Figure 49. Conversely, as arc length increases, the arc cone becomes wider and the arc is broader. The result is a weld bead that is wider and flatter and the level of weld penetration may increase very slightly [46].

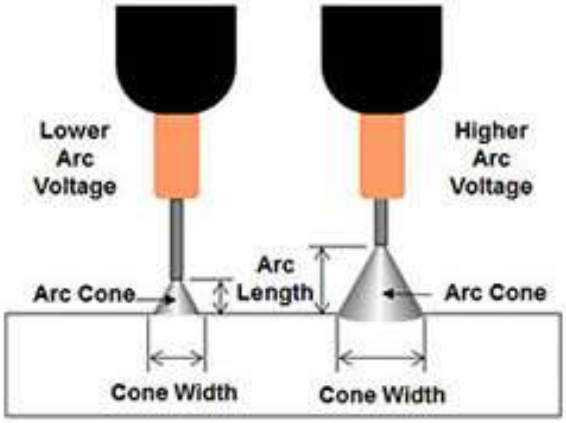

Figure 49 Variation in the arc length and cone with respect to arc voltage in Arc Welding process [46].

4. ***Concentration of electrolyte:*** Concentration was an inconsistent parameter as per literature. The results presented in this report failed to arrive at a concrete stance on its importance in the plasma generation process.

   The dissociation of Na^+ from Na_2CO_3 helps to develop the capacitance effect between the Na^+ ions, the Hydrogen bubbles and the cathode workpiece. However, it was observed that varying the concentration did not play a role in the plasma formation process. While changing the concentration of the electrolyte used can influence the V-I characteristics of a circuit, and the mass of Hydrogen produced during electrolysis; it neither has an influence on the vaporisation process and, as a result, nor on the plasma formation.

Through simple stoichiometric calculations, it was found that approximately 2.6 mg/L of Na_2CO_3 or a molarity of 2.54×10^{-5} M was sufficient to produce a plasma. This value was arrived on considering a few assumptions. The calculation is presented in Appendix 9.1. Hence, after the required molarity is supplied to ensure complete coverage of Hydrogen bubbles by Na^+ ions, **the amount of Na_2CO_3 used in the bath is of negligible importance to the plasma generation.**

5. ***Flow & Setup configuration:*** Literature reported the generation of plasma with $\dot{f}$ from 120 to 360 L/hr. In this project, the electrolyte was initially flown through the anode which did not allow the generation of plasma at such higher flow rates. As mentioned previously, plasma for cleaning applications could only be produced when lower $\dot{f}$ between 60 to 100 L/hr were used. A good surface was achieved between 60 and 80 L/hr.

   De-coupling the flow through the anode, reduces the turbulence in the interaction site greatly. Reduction in turbulence increases the resistance and the effects of Joule heating. As a result, plasma generation was observed at 300 L/hr when the flow was detached from the anode, whereas the plasma discharge on the steel substrate was sparse at 160 L/hr and unachievable at 200 L/hr in case of the setup where the flow was through the anode; see Figure 45.

   Separating the flow from the anode, lowers the input power drastically and aids in the formation of plasma at lower electrolyte temperatures. Figure 50 indicates the current and resistance for the corresponding voltage of a 0.0047 M solution with an inter-electrode distance of 1 mm and a flow rate of 100 L/hr but one has the electrolyte flow through the anode and the other has the flow detached from the anode. There is a noticeable increase in the resistance and a considerable reduction in the current for a given voltage. This is because when the flow is through the anode, instantaneous cooling and

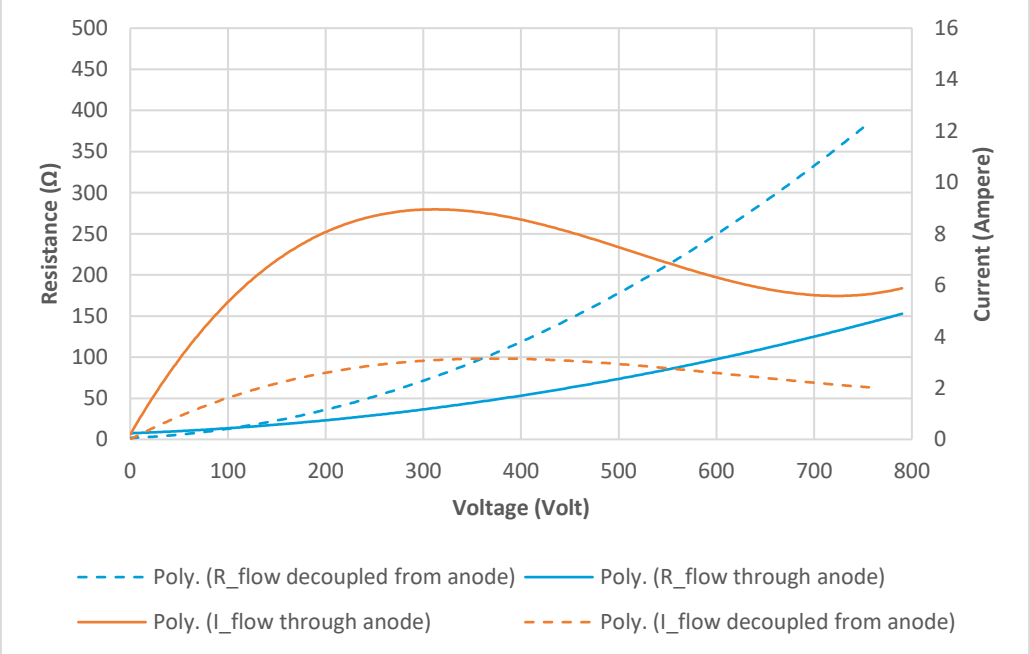

Figure 50 Current and resistance v/s voltage when flow is through the anode and when it is de-coupled.

replacement of electrolyte is taking place in the interaction region. Hence, more power is necessary to initiate instantaneous vaporisation and also to heat the electrolyte.

6. ***Hysteresis:*** It was observed during the experiments that there is a hysteresis in the current and resistance values when the Kellogg region is reached; see Figure 51 (i). There is a dramatic rise in the resistance from 40 to 80 Ω when the power is approximately increased from 2000 to 3000 W. This lies in the Kellogg region as a dip in current can be seen; refer Figure 51 (ii). The vaporisation increases the resistance but when the energy is sufficient for complete ionisation, the resistance reduces (plasma being more conductive than gases). Therefore, the transition between vaporisation and ionisation could be an apparent reason for the hysteresis in resistance and current.

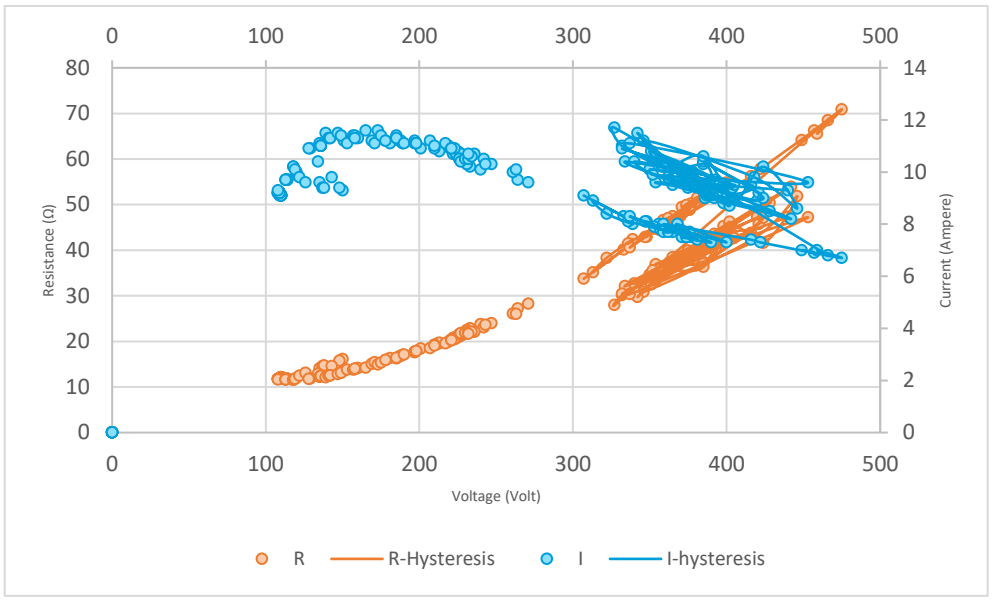

(i)

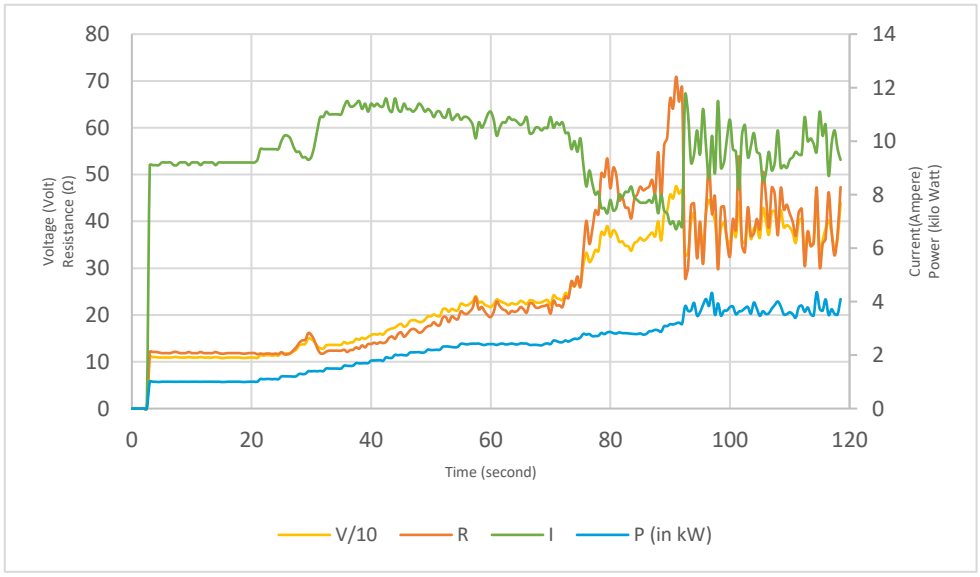

(ii)

Figure 51 (i) The hysteresis in current and resistance with respect to voltage, and, (ii) The change in voltage, resistance and power with respect to time.

6 Conclusions

The main goals of this thesis were to:

- understand the effect of Electrolytic Plasma Cleaning on the steel surface, and,
- find the optimal parametric conditions for the process to be carried out effectively.

While the first part of the project was fairly straight forward, the second part of the project was all the more complex and intertwined, mainly, because of the numerous physical phenomena taking place simultaneously and their combined implications on the plasma generation and on the surface. These interdependencies can be seen in Figure 52. The

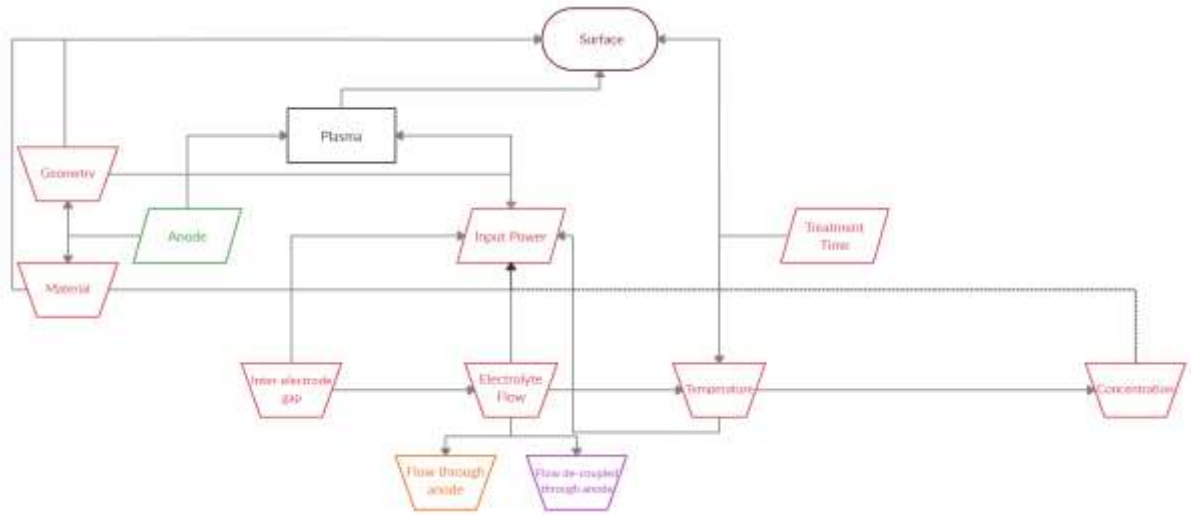

Figure 52 Block Diagram showing the dependencies between different parameters. The boxes in red denote the variable parameters.

concentration of the electrolyte influences the V-I characteristics of the input power but this influence is not as strong because the amount of salt needed to generate a plasma is quite low; see Chapter 5 point 4.

This project was initiated as an investigative effort which meant there were a few limitations in terms of the setup being used. Furthermore, existing literature on this topic failed to provide a clear view concerning the plasma generation. Despite these challenges, the following can be concluded from this research:

1. ***Anode material:*** Out of all the materials used as anode, Graphite gave the best performance because it disintegrates unlike its metallic counterparts which melt at higher powers and deposit on the steel substrate. Moreover, the contact angle measured for a sample treated with a graphite anode was the least compared to other anodic materials.
2. ***Geometry:*** Homogeneity in terms of surface topography can be achieved when a solid piece of graphite is used rather than one with perforations on it. The surface is modified by the plasma to form spheroidal nodules and craters which are approximately 5 μm in diameter. The R_a also increases to about 4.5 μm.

3. ***Treatment time:*** Within the tested power density range of 10 to 40 MW/m², treatments times of ≅ 20 seconds gave the best surface finish macroscopically and in terms of surface roughness.
4. ***Inter-electrode distance:*** Firstly, submergence is important to keep the voltage requirements low and to obtain a homogenous surface.
   Inter-electrode distances of 1 to 2 mm gave the best surface roughness based on confocal microscopic evaluations. The surface finish deteriorated as the distance increased. Increasing distance meant reduction in the amount of current being passed because of the increasing resistance. The breakdown voltage increases, the corresponding current lowers and the resistance is increasing which implies that as the gap increases more energy is required to form a plasma. At inter-electrode distances of 5 to 6 mm the plasma formed at the anode was unable to interact with the cathode apart from a few arcs formed on the surface because of the reduction in the electric field.
5. ***Flow rate:*** A lower flow rate i.e., between 60 to 100 L/hr is necessary when the electrolyte is flowing through the anode to form a plasma. For a good surface, the flow rate range narrows down to 60 and 80 L/hr. Lower flow means less turbulence, which lowers the heat transfer and facilitates rapid heating in the interaction region easing the Joule heating process. Lower flow also means that its easier for bubbles to form on the cathode surface as compared to higher flow rates. The setup becomes almost independent of flow rate when it is detached from the anode.
6. ***Flow through the anode v/s flow de-coupled:*** When the flow is through the anode, the plasma becomes continuous and stable only at higher electrolyte temperatures. However, when the flow is de-coupled from the anode, a stable plasma can be achieved at room temperatures. This is because when the flow is through the anode the resistance of the system is considerably low as compared to when its separated. The increase in resistance for a de-coupled flow is due to the reduction of turbulence at the interaction site which makes it easier to heat up the water and form water vapour by means of Joule heating. Also, when the flow is through the anode, a considerable amount of energy is wasted to vaporise the continuously replaced electrolyte in the interaction zone.
7. ***Temperature:*** In general, higher temperatures of 60 to 80 °C are preferred as higher temperatures promote Joule heating facilitating the generation of plasma at lower input power. As mentioned in the previous point, when the flow is separated from the anode, stable plasma can be achieved at room temperatures.
8. ***Hysteresis:*** Hysteresis in the current and resistance values for the same output voltage occurs when ionisation takes over vaporisation as a direct consequence of decreasing resistance from vaporisation phase to ionisation phase. It is because plasma is good electrical conductor, the conductivity of plasma is much higher than a stable gas.
9. ***Oxides:*** Oxides were effectively removed from the steel surface whenever a plasma was successfully generated.

The dependencies within the parameters shown in Figure 52 are removed as the operational values for the parameters are fixed. The final parametric values and dependencies can be found in Figure 53.

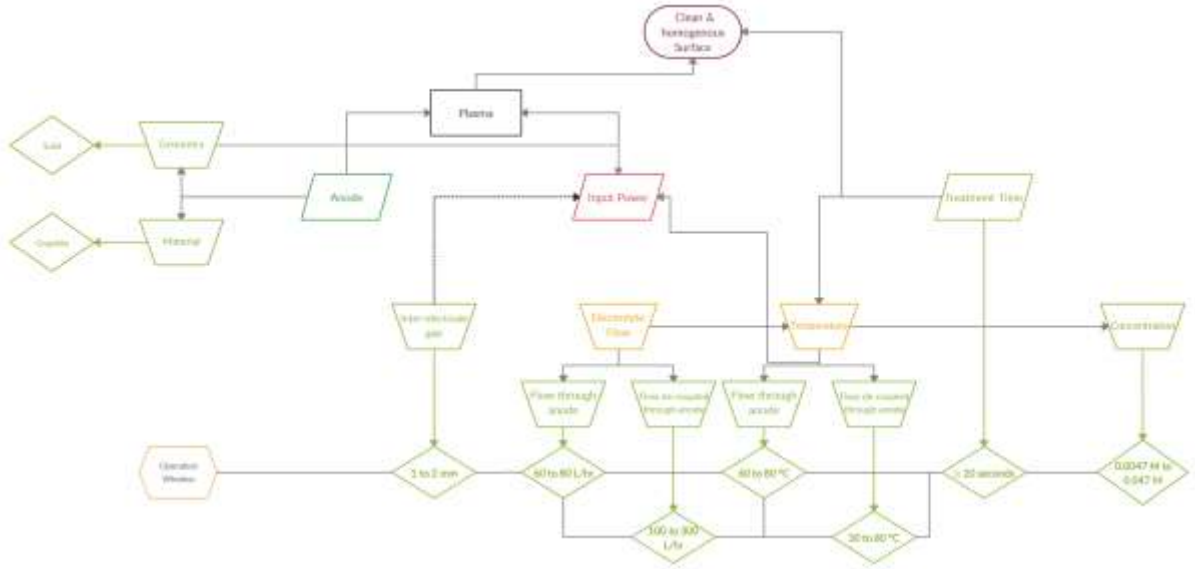

Figure 53 Block Diagram showing the operational window for the parameters investigated. The values are inside the green diamond boxes.

The remaining dependencies can be removed if the electrolyte temperature is regulated and the quantity of water vaporised is compensated to maintain a given concentration.

Flowing electrolyte will always induce turbulence and a cooling effect. Therefore, without a temperature controller, the flow continues to influence the bath temperature. Fixing the treatment time, does not remove the dependency of temperature on treatment time. The treatment time given is only for a single spot. Hence, a sufficiently long time will be needed to clean a strip of steel; see Chapter 8.Therefore, when in use for longer periods of time, without a controller to regulate the temperature, implies that the global temperature of the bath is bound to increase. Moreover, without temperature controllability, the increasing temperature of the bath can change the V-I characteristics of the system.

Vaporisation of water owing to increasing temperature of the bath increases the conductivity of the system. To compensate for the rise in conductivity, the amount of water being vaporised needs to be refilled back into the setup.

Apart from temperature control and water refill, a few more recommendations are provided in the subsequent chapter.

7 Recommendations

1. ***Temperature Controller:*** Since there was no temperature control in the setup used, initial currents were found to be very unstable due to the strong agitation of gas bubbles formed on the electrode surface during the boiling process. Also, more energy was needed to bring the water to boiling conditions. As the experiments progressed through the day, the current performance in the initial stage of an experiment stabilised because the pre-heated electrolyte from previous runs was found to be favourable for the boiling process and lesser energy was needed to raise the electrolyte temperature.
2. ***Conductivity Measurement & Water Refill:*** There is no refilling taking place in the bath to compensate for the water that heats up and vaporises. This led to an increase in conductivity of the circuit as the experiments progressed for the day. Moreover, the dispersion of graphite particles in the electrolyte as a result of the disintegration occurring at the anode also contributes to this increase in conductivity. Hence, it is also beneficial to have a real-time conductivity measurement.
3. ***Connection between Anode & Power Supply:*** Copper deposits were found on the surface of steel because of the Copper rod connecting the anode to the power supply which melts right at the junction where it touches the anode. The rod should be made out of a material that has high electrical conductivity and high melting point, such as Tungsten.
4. ***Graphite Removal Rate:*** The pulverisation of the graphite anode means that the inter-electrode distance increases in real time as the experiments are performed. Even if this removal rate is miniscule it effects the data collected as increasing distance increases the power requirement over time. For industrial purposes, a continuous graphite feed having a feed rate equal to the removal rate would help solve this problem. For further research purposes, measuring the removal rate of the graphite anode and trying to reduce the fragmentation should be considered.
5. ***Better Flow rate control:*** The flow controller used in this experiment did not have error corrections. The distance between the anode and cathode influences the set flow. Hence, once the flow rate changed during the experiment due to the increase in gap as a result of the disintegration of anode or slight bend in the cathode, it had to be corrected manually. The creation of the plasma also has an influence on the set flow as it, sometimes, results in jolts when the plasma is generated. To obtain more reliable results a flow controller which doesn't deviate from its set value needs to be installed.
6. ***Hydrogen & Water Vapour Detection:*** Even though plasma formation is taking place because of ionisation of Hydrogen and water vapour, the contribution of each individual species in the plasma generation at the interaction site is unknown. If the amount of Hydrogen and water vapour produced could be quantified, the energy required to form a plasma can be calculated more accurately.
7. ***Frequency:*** The steel surface needs to be evaluated quantifiably on the basis of pulse frequency.
8. ***Adhesion Test:*** Coating the samples with Zinc after treatment and checking the adhesive strength by using industrial testing methods such as 0T test and BMW test is crucial to determine which parameter combinations perform better.
9. ***Influence of motion:*** The EPC process is being developed with the intentions of being used on cold rolled steels. However, no studies were done on the plasma behaviour under the high-speed rolling conditions of a cold rolling mill.

8 Industrial Feasibility

Energy Requirements

An example of typical dimensions coming out of a cold rolling mill is:

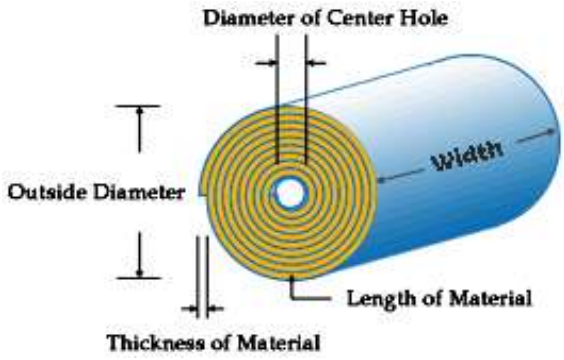

Diameter of Centre Hole	= 0. 610 m
Outer Diameter	= 1 m
Width	= 1.2 m.
Thickness of material	=0.0015 m
Length of steel roll	= 328.76 m
Area of steel roll	= 394.521 m^2

Two anode dimensions have been proposed for industrial applications and the total time needed to clean the aforementioned roll of steel has been calculated assuming that 20 seconds of time is needed to clean a section of the steel based on the results obtained during this project. The calculations are available in the Appendix 9.2. These values are tabulated in Table 9.

	$Anode_1$	$Anode_2$
Cross-section area	$1.2 \times 0.02 = 0.024\ m^2$	$1.2 \times 0.2 = 0.24\ m^2$
Time- taken for treatment	7.6 days	18.26 hours

Table 9 Cross-section area and time taken to clean a 394.521 m^2 of cold rolled strip steel.

As per the discussion, it was reasoned that having a setup with the flow separated from the anode requires lower input power than one where the flow is through perforations on the anode. Based on experimental trials, the power density and the energy consumption of the two different setup possibilities have been tabulated in Table 10. These calculations are also included in Appendix 9.2.

	Minimum	Maximum
Flow de-coupled from anode		
Power Density (MW/m^2)	10.6	11.5
Energy Consumed (kWh)	23255	25193
Flow through anode		
Power Density (MW/m^2)	22.1	40.7
Energy Consumed (kWh)	48448	89144

Table 10 Estimated power density and energy consumption for the two possible setups based on flow.

For better understanding of these numbers, the EPC process was compared to the energy consumption of the Netherlands. In the Netherlands, the average electricity consumption per home in 2016 exceeded 2,900 kWh [47]. Therefore, the energy required to clean a strip of cold rolled steel when the electrolyte is flowing through the anode is equivalent to powering

16 to 30 houses which comes down to 7 to 8 houses when the flow is de-coupled from the anode.

Furthermore, in 2017, the total energy consumption in the Netherlands amounted to 3157 PJ [47] or 8.8×10^{11} kWh. Each coil of steel with the dimensions mentioned above weighs ~ 4.5 tonnes. 8.8×10^{11} kWh is sufficient to clean 4.43 to 8.15 million tonnes of steel when the electrolyte flow is through the anode whereas when the flow is separated, it could possibly clean 15.7 to 17.0 million tonnes of steel. For comparison, the Netherlands produced 6.8 million tonnes of steel in the year 2017-2018 while the world cold rolled steel production was 40.8 million tonnes [48].

Bottlenecks

The biggest challenge for scaling up the EPC process would be the control of all the parameters simultaneously and perform real-time error corrections to stay within the operational band.

The time taken to clean a coil of cold rolled steel even with a larger anode is quite high at 18.26 hours and that is a direct consequence of the ~ 20 seconds of treatment time needed to clean the area of steel under the anode. The treatment time has to come down for this process to fit a conventional rolling mill.

The values for energy requirements stated in the previous section have not considered the additional energy that would be needed to control the temperature of the bath and maintain it within the ideal range. For instance, the plasma generation produces a large amount of heat which tends to increase the temperature of the bath beyond this range and the temperature controller would need to regulate this instantaneously.

9 Appendix

Appendix 1: Bare Spot Analysis

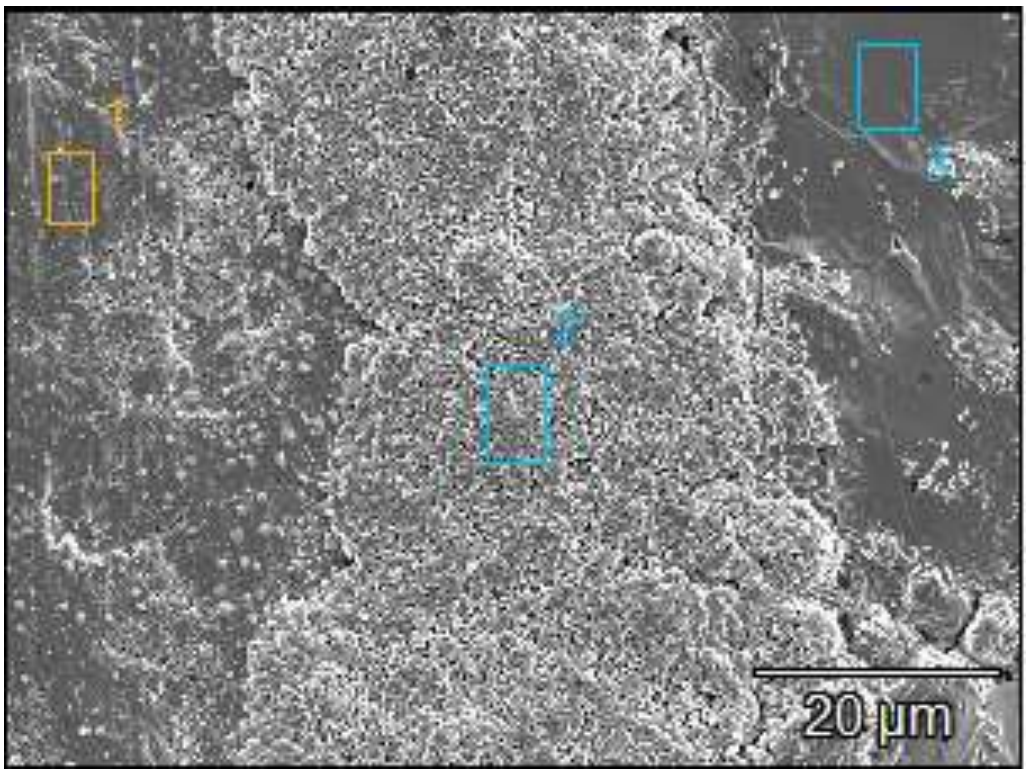

Figure 54 SEM image of (1) Inside Bare Spot, (2) Boundary between bare spot and Zn coating, and, (3) Zn coating.

Weight %

Area	C	O	Al	Si	Ca	Mn	Fe	Zn
1	0.32	3.15	0.29	0.00	0.00	4.69	72.93	18.61
2	0.67	2.56	0.45	0.01	0.00		5.09	91.22
3	0.47	0.37	0.39	0.04	0.02		0.00	98.70

Atom %

Area	C	O	Al	Si	Ca	Mn	Fe	Zn
1	1.40	10.32	0.57	0.00	0.00	4.47	68.35	14.90
2	3.24	9.30	0.98	0.02	0.00		5.30	81.16
3	2.46	1.46	0.92	0.09	0.04		0.00	95.03

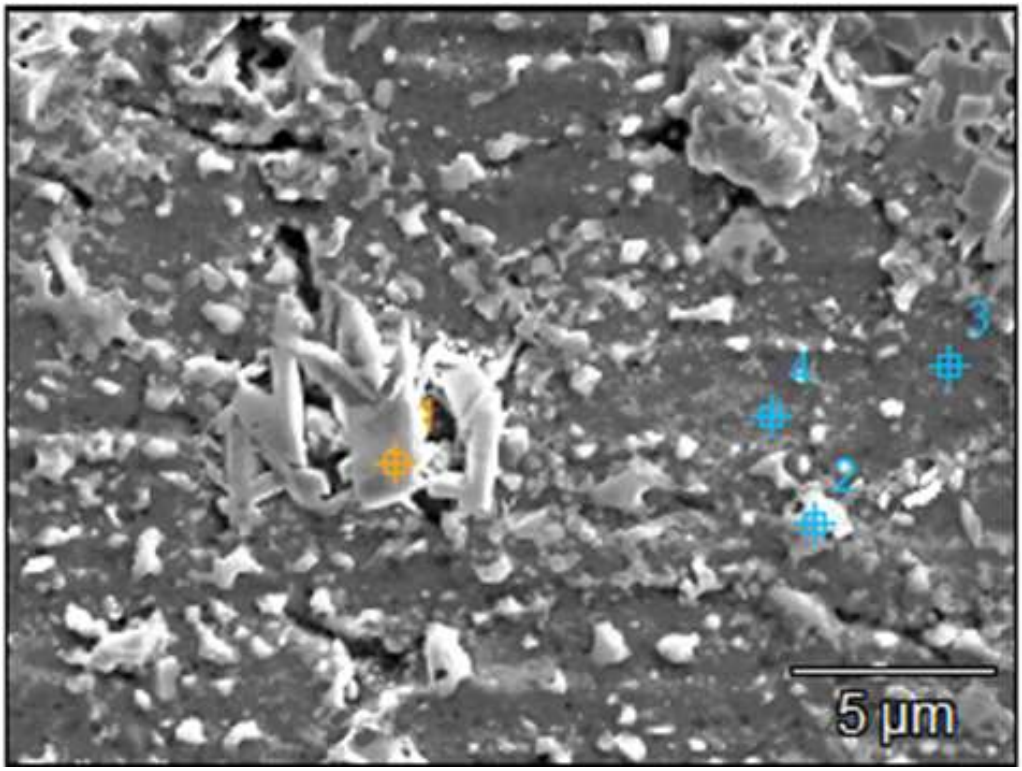

Figure 55 SEM image of $FeZn_{13}$ crystals inside the bare spot.

Weight %

Area	C	O	Al	Si	Mn	Fe	Zn
1	0.64	0.70	0.35			6.46	91.85
2		0.56	0.91	0.07		0.00	98.46
3		8.08	3.20	1.56	13.10	61.80	12.26
4		6.54	3.16	1.49	13.65	68.36	6.80

Atom %

Area	C	O	Al	Si	Mn	Fe	Zn
1	3.26	2.70	0.79			7.09	86.17
2		2.21	2.14	0.16		0.00	95.49
3		22.82	5.37	2.51	10.79	50.04	8.48
4		18.96	5.44	2.46	11.53	56.78	4.83

Appendix 2: Steel droplet on treated sample

Figure 56 SEM image of steel deposit on DP800 substrate.

Weight %

Spectrum	C	O	Na	Al	Si	P	S	Cl	K	Ca	Mn	Fe
29	1.57	0.73		0.05	0.04						0.32	97.3
30	1.61	8.87		0.06	0.09						1.56	87.8
31	25.4	20.9	0.75	0.52	0.39					1.75	3.91	46.4
32	10.9	35.2	0.12	0.09	0.06					36.7	1.03	15.8
33	1.63	14.0	0.07	0.06	0.11						1.78	82.4
34	41.9	17.0	1.28	0.64	0.53	0.20	0.80	0.25	0.24	2.02	3.28	31.8

Atom %

Spectrum	C	O	Na	Al	Si	P	S	Cl	K	Ca	Mn	Fe
29	6.77	2.37		0.09	0.08						0.30	90.4
30	5.85	24.2		0.09	0.13						1.24	68.5
31	47.8	29.4	0.73	0.43	0.31					0.98	1.61	18.7
32	21.0	50.7	0.12	0.07	0.05					21.1	0.43	6.53
33	5.36	34.7	0.12	0.09	0.15						1.28	58.4
34	64.9	19.8	1.03	0.44	0.35	0.12	0.46	0.13	0.12	0.94	1.11	10.6

Appendix 3: Titanium droplet on treated sample

Figure 57 SEM image of Titanium Deposit on DP800 steel surface.

Weight %

Spectrum	C	N	O	Al	Si	Ti	Cr	Mn	Fe
6	0.08	0.2	28.4	4.0		66.1	0.3		1.0
7	2.7		9.4	1.8	0.7	8.0	0.1	6.3	70.9
8	2.5		6.8	5.9	0.3	16.6	0.1	1.6	66.3

Atom %

Spectrum	C	N	O	Al	Si	Ti	Cr	Mn	Fe
6	0.2	0.4	53.1	4.4		41.3	0.2		0.5
7	9.3		23.8	2.7	1.0	6.8	0.1	4.6	51.6
8	8.4		17.5	9.0	0.4	14.3	0.1	1.2	49.1

Appendix 4: Chromium Carbides on treated sample

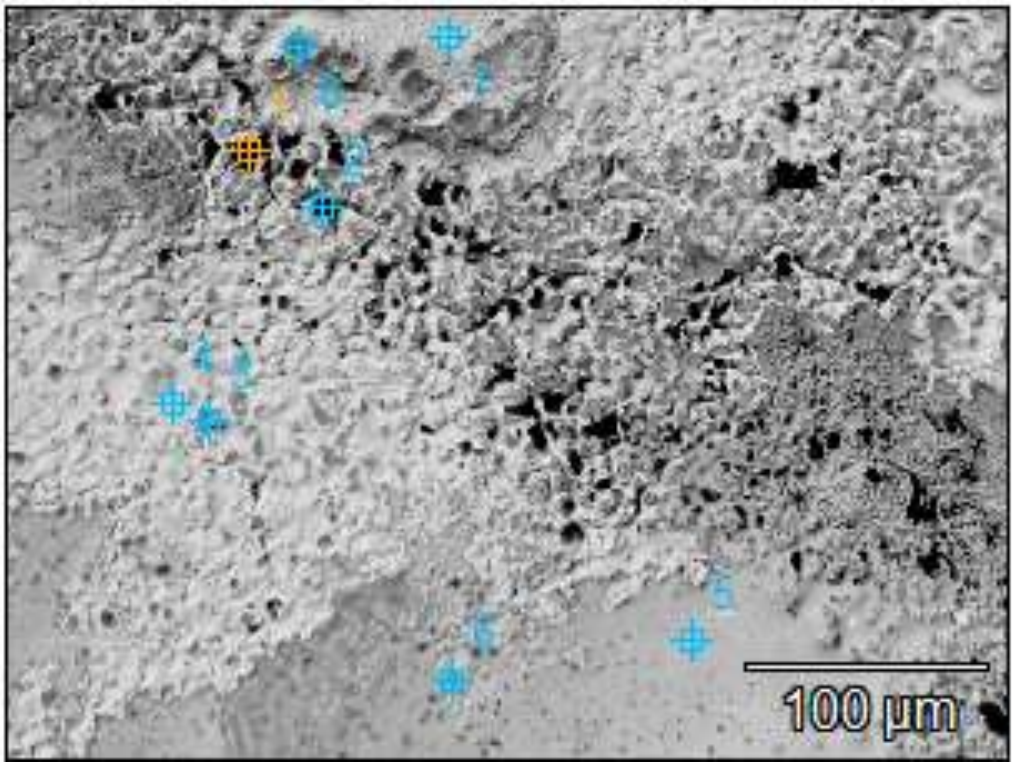

Figure 58 SEM image of plausible Chromium Carbide Deposits on the DP800 surface.

Weight %

Area	C	O	Na	Al	Si	Cr	Mn	Fe
1	24.9	8.7	1.8	1.6	1.1	0.8	3.7	57.6
2	31.3	18.3	2.4	2.3	2.6	1.6	8.3	33.3
3	0.00	8.9		3.0	3.8	3.7	10.9	69.7
4	0.6	3.0		0.02	0.3	0.9	2.7	92.4
5	0.2	9.7		0.8	0.5	1.2	4.1	83.6
6	0.05	17.1		13.0	3.7	1.4	7.7	57.0
7	0.9	3.2		0.1	0.5	0.5	3.1	91.7
8	0.6	19.2		9.1	6.1	3.3	20.7	41.0

Atom %

Area	C	O	Na	Al	Si	Cr	Mn	Fe
1	53.2	13.9	2.0	1.5	1.0	0.4	1.7	26.4
2	54.2	23.8	2.2	1.7	1.9	0.7	3.1	12.4
3	0.00	23.9		4.9	5.9	3.0	8.6	53.8
4	2.6	9.5		0.03	0.6	0.9	2.5	83.9
5	0.8	26.7		1.3	0.7	1.0	3.3	66.2

6	0.1	37.3		16.7	4.5	1.0	4.9	35.5
7	3.7	10.1		0.2	0.9	0.5	2.8	81.8
8	1.7	40.3		11.3	7.3	2.1	12.6	24.6

Appendix 5: Copper Oxide and Sodium particles on treated sample

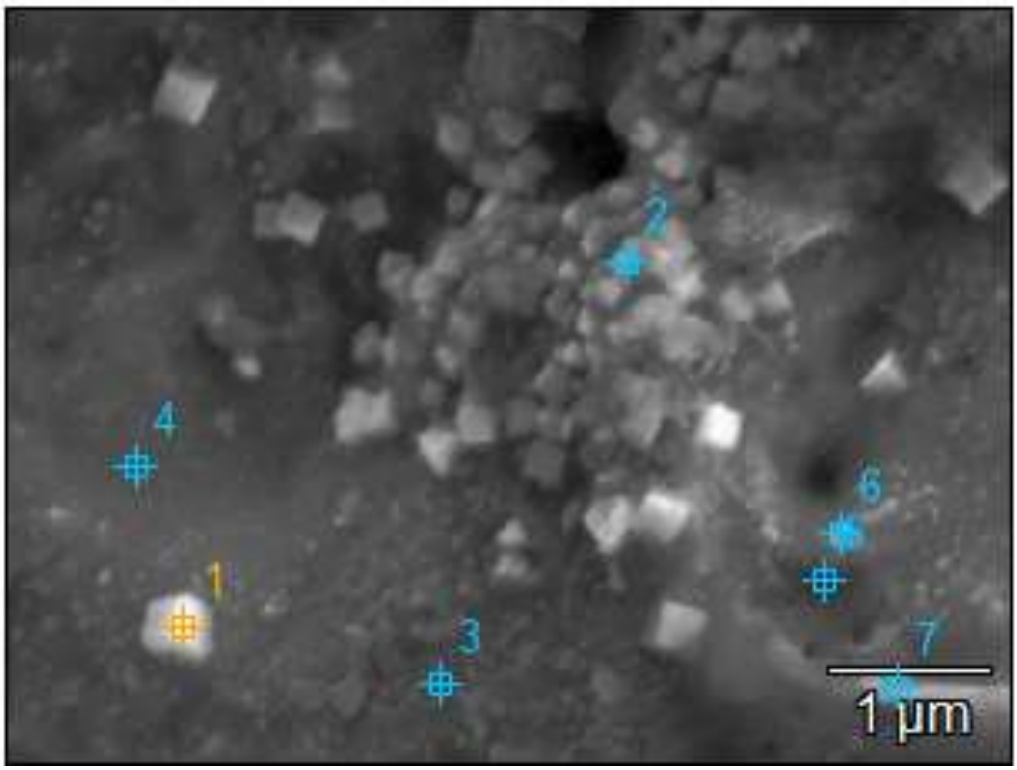

Figure 59 SEM image of Copper particles after EPC treatment of DP800 with a Copper anode.

Weight %

Area	C	O	F	Na	Al	Si	Mn	Fe	Cu
1	1.5	7.6	1.5		0.06	0.04	0.6	20.0	68.9
2	1.9	5.6				0.01	1.1	29.5	62.0
3	0.7			0.9	0.08	0.3	2.1	85.7	10.3
4	0.9				0.04	0.3	2.7	90.2	5.9
5	0.7	2.9		2.9	0.03	0.4	1.8	80.0	11.3
6	1.5	3.9		2.7	0.6	0.6	2.7	74.6	13.4
7	2.6	7.3		10.8		0.05	1.7	55.3	22.5

Atom %

Area	C	O	F	Na	Al	Si	Mn	Fe	Cu
1	5.7	22.2	3.8		0.10	0.07	0.5	16.8	50.9

2	7.6	17.3				0.02	1.0	26.02	48.12
3	3.0			2.0	0.2	0.6	2.08	83.34	8.82
4	3.9				0.1	0.6	2.69	87.71	5.02
5	3.0	8.9		6.2	0.06	0.6	1.61	70.82	8.82
6	5.7	11.3		5.6	1.1	1.0	2.35	62.96	9.95
7	8.5	18.1		18.6		0.07	1.20	39.41	14.07

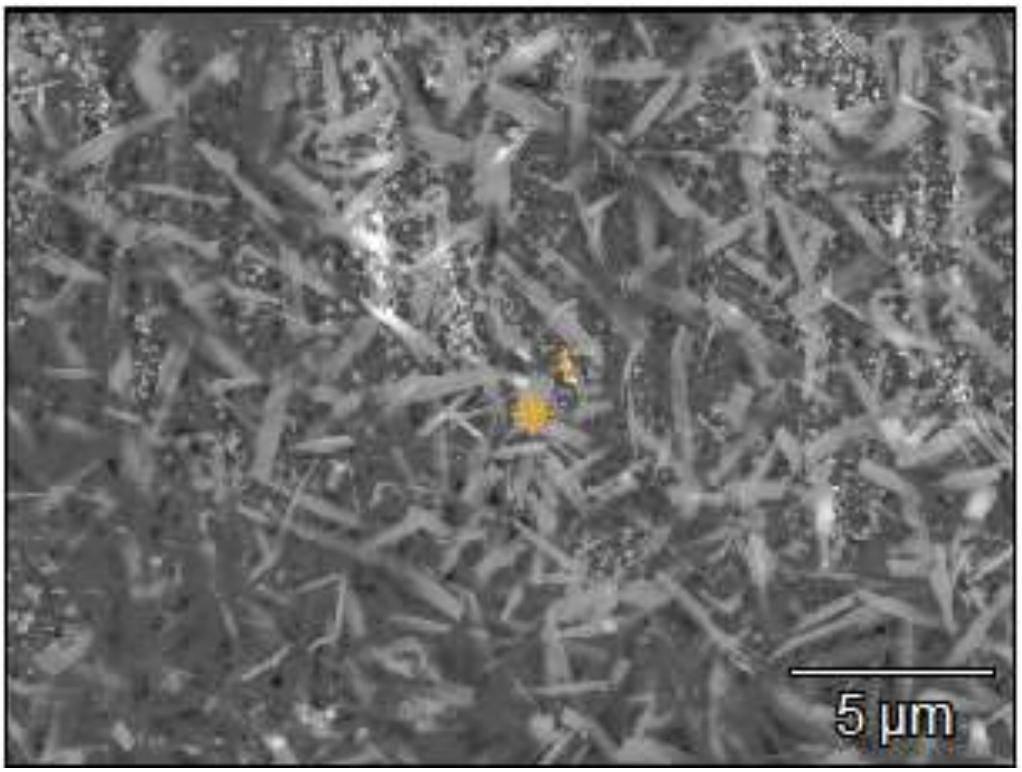

Figure 60 SEM image of Thorn-like structures made out of Na, Cu and O.

Weight %

Area	C	O	Na	Al	Si	Mn	Fe	Cu
1	0.4	7.8	5.5	1.9	0.3	3.6	53.7	26.8

Atom %

Area	C	O	Na	Al	Si	Mn	Fe	Cu
1	1.3	21.3	10.5	3.1	0.5	2.9	42.0	18.4

Appendix 6: DP800 Sample treated with a Graphite anode

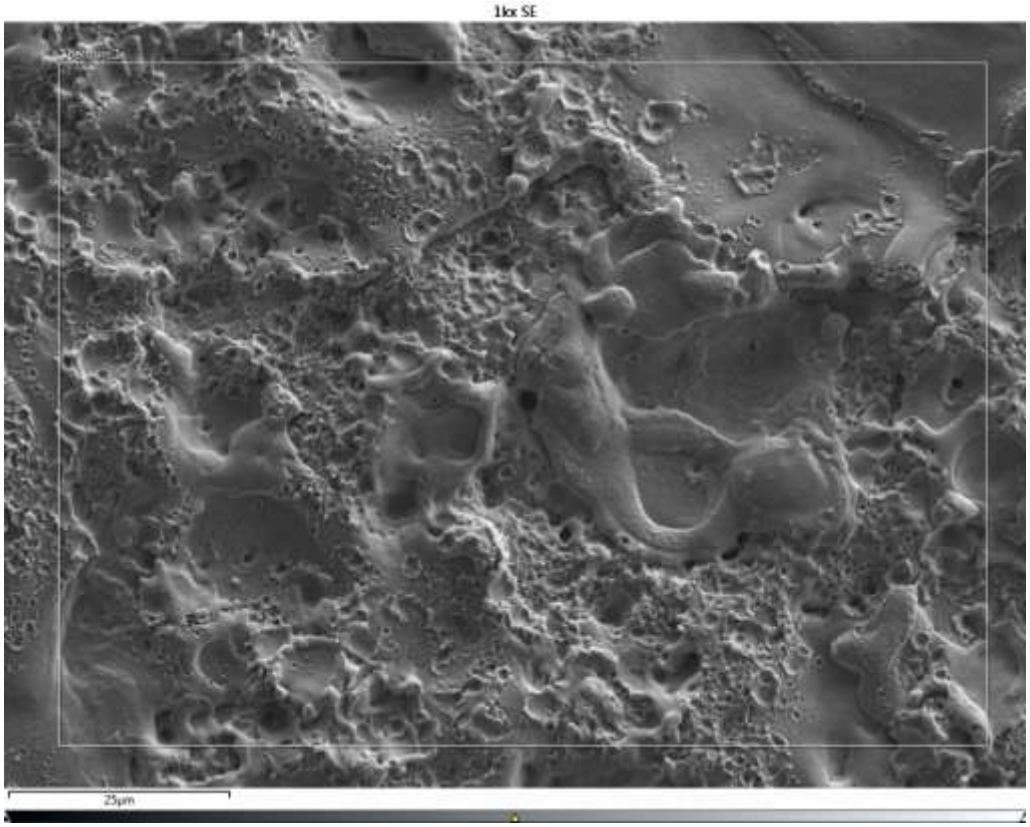

Figure 61 SEM image of steel surface after treatment with Graphite anode.

Weight %

Spectrum	C	O	Na	Al	Si	Mn	Fe
1	1.8	0.7	0.1	0.3	0.2	1.6	95.3

Atom %

Spectrum	C	O	Na	Al	Si	Mn	Fe
1	7.9	2.3	0.3	0.5	0.3	1.5	87.2

Appendix 7: Confocal Microscopy

Surface Roughness (μm)			Pictorial Representation of Surface	Legend
Reference sample		1.29	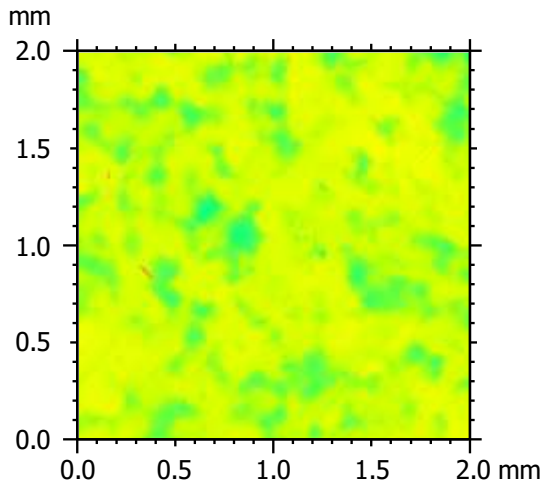	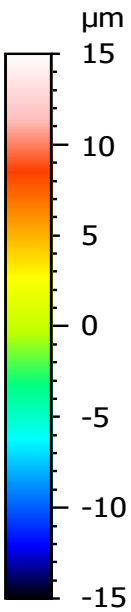
Inter-electrode gap (mm)	1	1.68	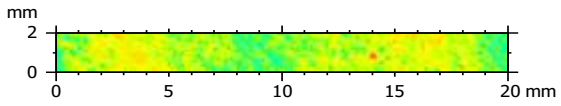	
	4	2.23	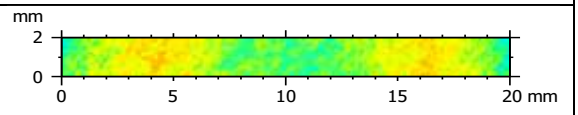	
	5	2.34	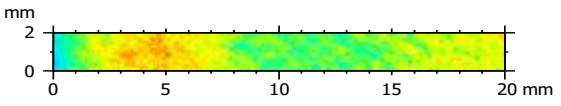	
	6	2.59	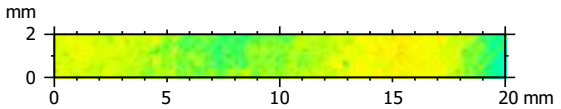	
Treatment Time (sec)	20	1.27	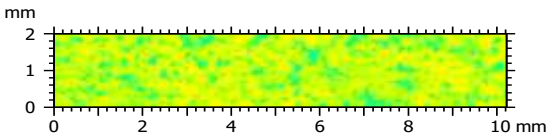	
	30	1.68	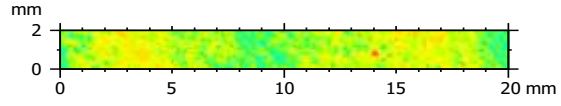	
	60	2.49	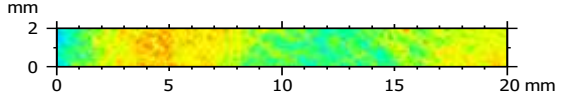	

Table 11 Heat map obtained from confocal microscopy on R_a as a function of inter-electrode distance and treatment time.

Appendix 8: Copper Deposits in treated Samples

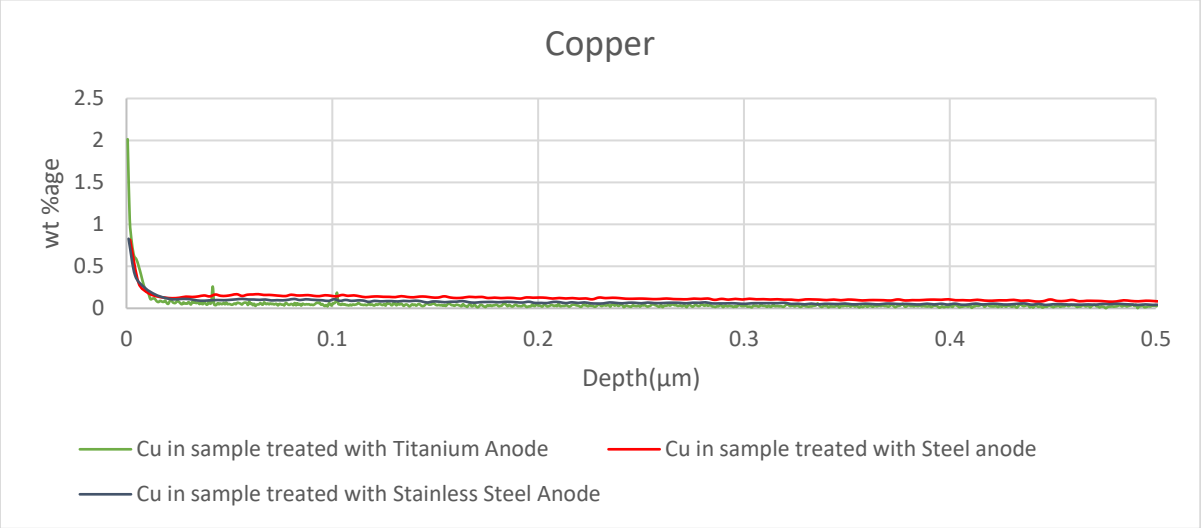

Figure 62 GDOES depth profilometry of Copper in samples annealed at different dew point temperatures.

Appendix 9: Calculations

Appendix 9.1: Molarity of Na_2CO_3 needed

Plasma interaction site = Cross-section area of anode with 20 mm diameter
= 0.0003141 m^3

Volume of electrolyte in interaction site = Cross-section area of anode × Inter-electrode gap (1 mm) = 3.141 × 10^{-4} L

Radius of Na^+ ions = 0.102 nm

For plasma generation, the Na^+ ions must get attracted towards the Cathode and trap H_2 and H_2O vapour to generate the capacitance effect. Hence, the Na^+ ions must ensure complete coverage of the cathode area equal to the anode cross-section area.

∴ Number of Na^+ ions $= \frac{Cross\text{-}section\ area\ of\ anode}{Area\ of\ an\ Na^+\ ion} = 9.61 \times 10^{15}$ ions of Na^+

Dissociation of $Na_2CO_3 \rightarrow 2\,Na^+ + CO_3^{2-}$. Every molecule of Na_2CO_3 gives 2 ions of Na^+.

$\therefore \frac{9.61 \times 10^{15}}{2}$ = 4.8055 × 10^{15} molecules of Na_2CO_3
= 7.98 × 10^{-9} moles of Na_2CO_3.

Molarity of Na_2CO_3 $= \frac{Moles\ of\ Na_2CO_3}{Volume\ of\ water\ in\ the\ interaction\ region}$

$= \frac{7.98 \times 10^{-9}\ moles}{3.141 \times 10^{-4}\ liters} = 2.54 \times 10^{-5}$ M.

1 mole Na_2CO_3, or 105.98844 grams. Weight of Na_2CO_3 needed in each litre of water = 2.54 × 10^{-5} moles × 105.98844 = 0.0027 g

Appendix 9.2: Industrial feasibility

Area of steel roll = length × width = (328.76 × 1.2) m^2 = 394.521 m^2

Area of $Anode_1$ = length × width = (0.02 × 1.2) m^2 = 0.024 m^2

Area of $Anode_2$ = length × width = (0.2 × 1.2) m^2 = 0.24 m^2

Assuming 20 seconds of treatment time,

$Anode_1$ takes = $\left\{\left(\frac{394.521\ m^2}{0.024\ m^2}\right) \times 20\right\}$ seconds = 328,767.5 seconds = 3.80 days

Cleaning both sides = (3.80 × 2) days = 7.61 days

$Anode_2$ takes = $\left\{\left(\frac{394.521\ m^2}{0.24\ m^2}\right) \times 20\right\}$ seconds = 32,876.75 seconds = 9.13 hours

Cleaning both sides = (9.13 × 2) hours = 18.26 hours

∴ $Anode_2$ is taken as the anode applicable for subsequent calculations as the time taken is 10X less than $Anode_1$.

Input power for flow de-coupled from anode = 1200 to 1300 W

Input power for flow through anode = 2500 to 4600 W

Area of trial anode = $\frac{\pi}{4} \times 10^{-6} \times (20^2 - 16^2)$ = 0.0001131 m^2

Power Density for flow de-coupled from anode = $(\frac{1200}{0.0001131})$ to $(\frac{1300}{0.0001131})$ W/m^2
= 10.61 to 11.49 MW/m^2

Power Density for flow through anode = $(\frac{2500}{0.0001131})$ to $(\frac{4600}{0.0001131})$ W/m^2
= 22.10 to 40.67 MW/m^2

Input power range needed for $Anode_2$ if flow is de-coupled from it
= (10.61 × 0.24m^2) to (11.49 × 0.24m^2) MW/m^2
= 2.55 to 2.76 MW

Energy consumed to clean the strip of steel when the flow is not through the anode using $Anode_2$ = (2.55 MW × 32,876.75 seconds) to (2.76 MW × 32876.75 seconds)
= 83.72 to 90.69 GJ = 23,254.99 to 25192.91 kWh

Input power range needed for $Anode_2$ if flow is through it

= (22.10 to 40.67) MW/m^2 × 0.24m^2

= 5.31 to 9.76 MW

Energy consumed to clean the strip of steel when the flow is through the anode using $Anode_2$

= (5.31 MW × 32,876.75 seconds) to (9.76 MW × 32876.75 seconds)

= 174.41 to 320.92 GJ = 48447.91 to 89144.15 kWh

10 References

[1] "Automotive Trends Report," 2017. [Online]. Available: https://www.epa.gov/automotive-trends/highlights-automotive-trends-report.

[2] E. Ghassemieh, "Materials in Automotive Application, State of the Art and Prospects," in *New Trends and Developments in automotive industry*, Rijeka, Croatia, InTech, 2011, pp. 365-394.

[3] N. Baluch, Z. M. Udin and C. S. Abdullah, "Advanced High Strength Steel in Auto Industry: an Overview," *Engineering, Technology & Applied Science Research Vol. 4, No. 4,* pp. 686-689, 2014.

[4] C. Lahaije, A. Blowey, J. Loiseaux, B. Ennis, C. Ionescu and B. Berkhout, "Mass saving potential of DP800HyperForm® against HSLA grades for BIW applications," *4th International Conference on Steels in Cars and Trucks,* 2014.

[5] "Annealing of cold rolled steel," [Online]. Available: https://www.calmet.com/annealing-of-cold-rolled-steel/.

[6] S. Sarna, "Annealing of Cold Rolled Steel," 9 November 2013. [Online]. Available: https://www.ispatguru.com/.

[7] F. S. Rodrigo, "Development of a model for predicting oxidation during annealing of Advanced High Strength Steels (AHSS)," Delft University of Technology, Delft, 2017.

[8] W. Mao, "Oxidation Phenomena in Advanced High Strength Steels: Modelling and Experiment," Delft University of Technology, The Netherlands, Delft, 2018.

[9] G. Song, T. Vystavel, N. v. d. Pers, J. D. Hosson and W. Sloof, "Relation between microstructure and adhesion of hot dip galvanized zinc coatings on dual phase steel," *Acta Materialia Volume 60, Issues 6–7, https://doi.org/10.1016/j.actamat.2012.02.003,* pp. 2973-2981, 2012.

[10] V. A. Lashgari, "Internal and External Oxidation of Manganese in Advanced High Strength Steels," Uitgeverij BOXPress, Delft, 2014.

[11] A. I. Vitkin, G. A. Kokorin, A. G. Grishko and P. A. Tyukanov, "Effect of aluminum in zinc baths on the formation of the diffusion coating in hot-dip galvanizing of steel," *Metal Science and Heat Treatment, doi: 10.1007/BF00660334* , 1973.

[12] T. Min, Y. Gao, X. Huang, Z. Gong, K. Li and S. Ma, "Effects of aluminium concentration on the formation of inhibition layer during hot-dip galvanizing," *International Journal of Heat and Mass Transfer, Volume 127, https://doi.org/10.1016/j.ijheatmasstransfer.2018.08.016,* pp. 394-402, 2018.

[13] M. Kuperus, “The delamination process of the dross build-up structure on submerged hardware in Zn-Al and Zn-Mg-Al baths.,” Delft University of Technology, Delft, 2018.

[14] W. Melfo, “Selective oxidation on AHSS during continuous annealing and the consequences for Zn wettability, Reference Number 134392.,” Tata Steel Netherlands, IJmuiden, 2007.

[15] L. Guzman, G. Wolf and G. Davies, “PVD–IBAD zinc coating development for automotive application,” *Surface and Coatings Technology, Vol. 174-175, https://doi.org/10.1016/S0257-8972(03)00805-3,* pp. 665-670, 2003.

[16] J. Kawafuku, J. Katoh, M. Toyama, K. Ikeda, H. Nishimoto and H. Satoh, “Properties of Zinc Alloy Coated Steel Sheets Obtained by Continuous Vapour Deposition Pilot-Line,” in *SAE Automotive Corrosion and Prevention Conference and Exposition, https://doi.org/10.4271/912272*, 2019.

[17] M. Dutta, A. K. Halder and S. B. Singh, “Morphology and properties of hot dip Zn–Mg and Zn–Mg–Al alloy coatings on steel sheet,” *Surface and Coatings Technology, Volume 205, Issue 7, https://doi.org/10.1016/j.surfcoat.2010.10.006,* pp. 2578-2584, 2010.

[18] H. Holleck and V. Schier, “Multilayer PVD coatings for wear protection,” *Surface and Coatings Technology, Volume 76-77, Part-1, https://doi.org/10.1016/0257-8972(95)02555-3,* pp. 328-336, 1995.

[19] M. Carr and M. Robinson, “The Effects of Zinc Alloy Electroplating on the Hydrogen Embrittlement of High Strength Steels,” *The International Journal of Surface Engineering and Coatings, https://doi.org/10.1080/00202967.1995.11871060,* pp. 58-64, 2017.

[20] B. Navinšek, P. Panjan and I. Milošev, “PVD coatings as an environmentally clean alternative to electroplating and electroless processes,” *Surface and Coatings Technology Volume 116-119,* pp. 476-487, 1999.

[21] J.Carpio, J. Casado, J. Álvarez and F. Gutiérrez-Solana, “Environmental factors in failure during structural steel hot-dip galvanizing,” *Engineering Failure Analysis, Volume 16, Issue 2, https://doi.org/10.1016/j.engfailanal.2008.02.006,* pp. 585-595, 2009.

[22] E. V. Parfenov, A. Yerokhin, R. R. Nevyantseva, M. V. Gorbatkov, C. J. Liang and A. Matthews, “Towards smart electrolytic plasma technologies: An overview of methodological approaches to process modelling,” *Surface and Coatings Technology, Volume 269, https://doi.org/10.1016/j.surfcoat.2015.02.019,* pp. 2-22, 2015.

[23] P. Gupta, G. Tenhundfeld, E. Daigle and D. Ryabkov, “Electrolytic plasma technology: Science and engineering—An overview,” *Surface & Coatings Technology 201 https://doi.org/10.1016/j.surfcoat.2006.11.023,* pp. 8746-8760, 2007.

[24] A. Yerokhin, A. Pilkington and A. Matthews, “Pulse current plasma assisted electrolytic cleaning of AISI 4340 steel,” *Journal of Materials Processing Technology, doi:10.1016/j.jmatprotec.2009.08.018,* pp. 54-63, 2009.

[25] E. Meletis, X. Nie, F. Wang and J. Jiang, “Electrolytic plasma processing for cleaning and metal-coating of steel surfaces,” *Surface and Coatings Technology 150,* pp. 246-256, 2002.

[26] A. Yerokhin, X. Nie, A. Leyland, A. Matthews and S. Dowey, “Plasma Electrolysis for Surface Engineering,” *Surface and Coatings Technology,* pp. 73-93, 1999.

[27] S. A. Galedari and S. M. Khoei, “Effect of pulse frequency on microstructure and surface properties of Ck45 steel treated by plasma electrolysis method,” *Journal of Alloys and Compounds 551,* pp. 415-421, 2013.

[28] W. Gui, J. Lin, G. Hao, Y. Qu, Y. Liang and H. Zhang, “Electrolytic plasma processing-an innovative treatment for surface modification of 304 stainless steel,” *https://doi.org/10.1038/s41598-017-00204-w,* 2017.

[29] K. Legg, “Electrolytic Plasma Processing for Sequential Cleaning and Coating Deposition for Cadmium Plating Replacement,” Rowan Technology Group, 2008.

[30] A. Pogrebnyak, A. S. Kaverina and M. Kylyshkanov, “Electrolytic Plasma Processing for Plating Coatings and Treating Metals and Alloys,” *Protection of Metals and Physical Chemistry of Surfaces, Vol. 50,* pp. 72-88, 2014.

[31] J. Liang, “A study on the cleaning and modification of metal surfaces by direct current cathodic electrolytic plasma process,” Louisiana State University, 2013.

[32] S. K. Sengupta and O. P. Singh, “Contact glow discharge electrolysis: a study of its onset and location,” *Journal of Electroanalytical Chemistry and Interfacial Electrochemistry, Volume 301, Issues 1–2,,* pp. 189-197, 1991.

[33] M. Okada, N. Ohta, O. Yoshimoto, M. Tatsumi and M. Inagaki, “Review on the high-temperature resistance of graphite in inert atmospheres,” *Carbon, Volume 116,* pp. 737-743, 2017.

[34] C. D. Cionea, “Microstructural evolution of surface layers during electrolytic plasma processing,” The University of Texas at Arlington, 2009.

[35] F. Cheng, W. Gui and J. Lin, “Surface Modification of Q195 Structure Carbon Steel by Electrolytic Plasma Processing,” *https://doi.org/10.3390/met8100831,* 2018.

[36] A. M. Orlov, I. O. Yavtushenko and M. V. Churilov, “Kinetics of the Formation of Gas Bubbles during Polarization of Copper and Graphite Electrodes in Electrolytic Aqueous Solutions,” pp. 831-835, 2010.

[37] L. Kumruoglu and A. Özel, “Electrolytic Plasma Surface Cleaning of Industrial Metallic Components,” *Acta Physica Polonica A, Volume 125, 10.12693/APhysPolA.125.379,* 2014.

[38] “Drop Shape Analysis,” [Online]. Available: https://www.kruss-scientific.com/services/education-theory/glossary/drop-shape-analysis/.

[39] “Contact angle,” [Online]. Available: https://www.kruss-scientific.com/services/education-theory/glossary/contact-angle/.

[40] “Confocal microscopy,” [Online]. Available: https://www.kruss-scientific.com/services/education-theory/glossary/confocal-microscopy/.

[41] I. Parezanović and M. Spiegel, “Influence of dew point on the selective oxidation during annealing of cold rolled DP and Ti-IF steels,” *Journal of Corrosion Science and Engineering 6,* 2003.

[42] A. E. Baumann, D. A. Burns, B. Liu and V. S. Thoi, “Metal-organic framework functionalization and design strategies for advanced electrochemical energy storage devices,” *Communications Chemistry volume 2, Article number: 86; doi:10.1038/s42004-019-0184-6,* 2019.

[43] Z. Liu, X. Yuan, S. Zhang, J. Wang, Q. Huang, N. Yu, Y. Zhu, L. Fu, F. Wang, Y. Chen and Y. Wu, “Three-dimensional ordered porous electrode materials for electrochemical energy storage,” *NPG Asia Materials volume 11, Article number: 12; doi:10.1038/s41427-019-0112-3,* 2018.

[44] F. G. Cuevas, J. M. Montes, J. Cintas and P. Urban, “Electrical conductivity and porosity relationship in metal foams,” *Journal of Porous Materials volume 16, Article number: 675; doi: https://doi.org/10.1007/s10934-008-9248-1,* 2008.

[45] “Special Graphite,” [Online]. Available: https://www.toyotanso.com/Products/Special_graphite/data.html.

[46] “Variables that Affect Weld Penetration,” [Online]. Available: https://www.lincolnelectric.com/en-us/support/process-and-theory/Pages/variables-weld-penetration.aspx.

[47] “Trends in the Netherlands,” 2018. [Online]. Available: https://longreads.cbs.nl/trends18-eng/economy/figures/energy/.

[48] “World Steel in Figures,” World Steel Association, Brussels, 2019.

[49] Z. Yang and A. Bandivadekar, “Light-duty vehicle greenhouse gas and fuel economy standards, The International Council on Clean Transportation,” The International Council on Clean transportation, 2017.

[50] M. Maderthaner, A. Jarosik and G. A. a. R. Haubner, “Effect of dew point on the selective oxidation of advanced high strength steels,” *Materials Science Forum, Vol. 891; doi:10.4028/www.scientific.net/MSF.891.292,* pp. 292-297, 2017.